Mariana Tiemi Tamura

An assessment of the drilling process employed by the Hole-Drilling Method for residual stress measurements

Dissertation submitted to the Department of Mechanical Engineering at Federal University of Santa Catarina in partial fulfilment of the requirements for the degree of Master of Engineering in Mechanical Engineering.

Supervisor: Prof. Rolf Bertrand Schroeter, Dr. Eng.
Co-supervisor: Prof. Armando Albertazzi Gonçalves Jr., Dr. Eng.

Florianópolis
2016

Ficha de identificação da obra elaborada pelo autor,
através do Programa de Geração Automática da Biblioteca Universitária da UFSC.

Tamura, Mariana Tiemi
An assessment of the drilling process employed by the Hole-Drilling Method for residual stress measurements / Mariana Tiemi Tamura ; orientador, Rolf Bertrand Schroeter ; coorientador, Armando Albertazzi Gonçalves Júnior. - Florianópolis, SC, 2016.
177 p.

Dissertação (mestrado) - Universidade Federal de Santa Catarina, Centro Tecnológico. Programa de Pós-Graduação em Engenharia Mecânica.

Inclui referências

1. Engenharia Mecânica. 2. Método do Furo Cego. 3. Tensões residuais. 4. Fresa de topo reto. 5. Furação. I. Bertrand Schroeter, Rolf . II. Albertazzi Gonçalves Júnior, Armando . III. Universidade Federal de Santa Catarina. Programa de Pós-Graduação em Engenharia Mecânica. IV. Título.

Mariana Tiemi Tamura

An assessment of the drilling process employed by the Hole-Drilling Method for residual stress measurements

This dissertation was considered adequate to obtain the degree of Master of Engineering in Mechanical Engineering and was approved on its final version by the Mechanical Engineering Graduate Programme.

Florianópolis, 11 February 2016.

Prof. Armando Albertazzi Gonçalves Jr., Dr. Eng.
Department Chair

Examining board:

Prof. Rolf Bertrand Schroeter, Dr. Eng.
Supervisor – Federal University of Santa Catarina

Prof. Armando Albertazzi Gonçalves Jr., Dr. Eng.
Co-supervisor – Federal University of Santa Catarina

Prof. Walter Lindolfo Weingaertner, Dr.-Ing.
Federal University of Santa Catarina

Prof. Milton Pereira, Dr. Eng.
Federal Institute of Santa Catarina

Matías Roberto Viotti, Dr. Ing.
LABMETRO - Federal University of Santa Catarina

To my father and brother.

To Marina,
who made me understand Cortázar's words
"No aprenderé por eso a quererte mejor,
pero desalojado de la felicidad
sabré cuánta me dabas
con solamente a veces estar cerca".

ACKNOWLEDGEMENTS

– PETROBRAS, that funded this work through the CARD3 project;

– PRH-34/ANP Programme, that provided the scholarship;

– Prof. Rolf Bertrand Schroeter, who confided this work to me;

– Prof. Armando Albertazzi Gonçalves Jr., for his trust and everlasting willingness to help;

– All the LABMETRO staff that I could count on, especially Matías Viotti, Rosana Vieira, Elsio Varella and Celso Veiga;

– SENAI – ISI in Manufacturing Systems, that made the experiments possible, and Saulo Melotti, who supported us during the procedures;

– CTIF/UNIFEBE, particularly Denis Boing, that helped with the cutting tool characterisation;

– LABCONF/UFSC, LCM/UFSC, LCME/UFSC and their respective personnel, for kindly granting me access to their facilities and technical expertise;

– No words can bear the gratitude I hold for Rodrigo Blödorn, a caring mentor and a loyal friend who not only taught me the ropes of this work, but also provided all the required technical and emotional support to overcome the countless challenges I faced during the past two years;

– Special thanks are addressed to Luciano Serconek Fuso, the research intern I had the honour to supervise and to rely on, I could have neither finished at this rate without his relentless diligence nor survived lacking his witty;

– All my friends and colleagues that supported me somehow during this period: Adriano, Angela, Bruna, Bruno, Bryant, Cabral, Clarissa, Cyrillo, Danilo, Estiven, Fabíola, Fernanda, Gabriel, João Vitor, Jhonattan, Knoblauch, Lívia, Louise, Magrão, Marcos José and his wife Luciana, Miriam, Mônica, Nathalia, Paula, Pati, Paty, Pedro, Rolón, Tahiriny, Willian;

– Andrea, remotely omniscient and an accomplice since 2013;

– Marina, *per starmi sempre vicina e avermi regalato l'obiettivo che mi ha incoraggiato ad andare avanti anche nei giorni più duri*;

– My father and my brother, for the patience, care and comprehension.

"And I must continue to follow the path I take now. If I do nothing, if I study nothing, if I cease searching, then, woe is me, I am lost. That is how I look at it - keep going, keep going come what may."

(Vincent van Gogh)

ABSTRACT

Predictive maintenance is important to prevent catastrophic accidents in oil and gas distribution networks, since failures in pipelines and other mechanical components may lead to serious economic and environmental consequences. A possible approach to perform predictive maintenance is to monitor periodically loads that act on these structures. This task can be carried out through the Hole-Drilling Method to measure residual stresses, a consolidated semi-destructive technique for both in-field and in-lab applications. Standardised by ASTM E837 – 13a, this method is based on a blind hole drilling that relieves local stresses; the stress relief that occurs after material removal induces a microstructure reorganization, settling the material in a new equilibrium state after producing strains on the hole surrounding surface. These strains are related to the stresses that caused them according to Hooke's law in linearly elastic isotropic materials. The measurement result provided by this technique is intrinsically sensitive to the drilling process and produced hole characteristics, since machining induced residual stresses can mislead the true stress value. Besides, the hole geometry may differ significantly from the model recommended by the standard, provoking further errors in stress calculation. This work aims to investigate a cutting tool and cutting parameters combination that presents the best performance for residual stress measurements through the Hole-Drilling Method from two perspectives: machining and Electronic Speckle Pattern Interferometry application to measure strains. Two square end mills (two and four flutes) with TiAlN coating were used to drill the following workpiece materials: aluminium alloy AA 6061, carbon steel AISI 1020 and stainless steel AISI 304L. Chip and burr formation are investigated in preliminary analysis concerning the optical technique application since these elements can cause loss of correlation and produce unreliable data. Rotational speed and feed rates effects on machining induced residual stresses are analysed through analysis of variance. Chip analysis is performed to assess qualitatively plastic deformation suffered during the process. This information are complemented with microhardness measurements to ver-

ify microstructural changes caused by the drilling process. Four-flute end mill presented lower machining induced residual stress absolute values. Particularly, the cutting tool and cutting parameters combination yielded satisfactory results when drilling AA 6061 and AISI 1020. However, AISI 304L presented highly compressive machining induced residual stresses for almost all conditions. The most influential cutting parameter on machining induced residual stress introduction was the feed rate in the majority of the tested conditions.

Keywords: Hole-Drilling Method. Residual stresses. Square end mill. Drilling.

RESUMO

A manutenção preditiva tem um papel importante na prevenção de acidentes catastróficos em redes de distribuição de petróleo e gás, uma vez que falhas em dutos e componentes mecânicos integrantes destas malhas podem trazer graves consequências econômicas e ambientais. Um dos procedimentos usados para tal fim é o monitoramento periódico dos esforços que atuam sobre estas estruturas; isto pode ser feito através do Método do Furo Cego para medição de tensões residuais, uma técnica semi-destrutiva consolidada tanto em aplicações em campo quanto em laboratórios. Este método, normatizado pela ASTM E837 – 13a, consiste na produção de um furo cego, o qual alivia tensões localizadas; o alívio proporcionado pela remoção de material provoca a reorganização da estrutura, a qual se acomoda em uma nova condição de equilíbrio, que se expressa em deslocamentos na superfície vizinha ao furo. Os deslocamentos estão associados às tensões que as provocaram através de lei de Hooke em materiais isotrópicos linearmente elásticos. O resultado de medição desta técnica é intrinsicamente susceptível à qualidade do processo de furação e do furo produzido, pois tensões induzidas pela usinagem podem mascarar o valor de tensão que se deseja conhecer, além de produzir características geométricas que diferem significativamente do modelo padronizado pela norma e podem provocar erros no cálculo das tensões. Este trabalho visa estudar uma combinação de parâmetros de corte e ferramenta que apresente o melhor desempenho para medição de tensões residuais através do Método do Furo Cego tanto do ponto de vista da usinagem quanto da aplicação da Interferometria *speckle* na medição dos deslocamentos. Duas fresas de topo reto (dois e quatro gumes) com revestimento de TiAlN foram utilizadas na furação de corpos de prova dos seguintes materiais: liga de alumínio AA 6061, aço carbono AISI 1020 e aço inoxidável AISI 304L. Formação de cavaco e rebarba são avaliados em análise preliminar quanto à utilização da técnica óptica para medição de deslocamentos, uma vez que podem provocar perda de correlação e inutilizar pontos de medição. Os efeitos da rotação e da velocidade

de avanço na tensão residual induzida pela usinagem são analisados através de análise de variância. Análise do cavaco é usada para avaliar qualitativamente a deformação plástica sofrida durante o processo; estas informações são complementadas com medições de microdureza para verificar alterações na microestrutura causadas pela furação. Fresas de quatro gumes apresentaram menores valores absolutos de tensão residual induzidas pela usinagem. Em particular, a combinação de ferramenta e parâmetros de corte mostrou-se satisfatória no caso do AA 6061 e AISI 1020, no entanto para o AISI 304L foram encontrados valores de tensão residual induzidas pela usinagem de caráter bastante compressivo em quase todas as condições. Observou-se que o parâmetro de corte de maior influência na introdução de tensões residuais pela usinagem foi a velocidade de avanço na maioria das condições testadas.

Palavras-chave: Método do Furo Cego. Tensões residuais. Fresa de topo reto. Furação.

UMA AVALIAÇÃO DO PROCESSO DE FURAÇÃO EMPREGADO PELO MÉTODO DO FURO CEGO PARA MEDIÇÃO DE TENSÕES RESIDUAIS

Introdução

A manutenção preditiva de equipamentos e componentes mecânicos é uma atividade de importância vital na indústria de petróleo e gás; em sua ausência, paradas não planejadas no ciclo de produção e contratempos devido a falhas catastróficas podem acarretar prejuízos em várias esferas, principalmente no âmbito econômico e ambiental. Uma das possíveis causas de falha é a combinação de tensões mecânicas de operação e tensões residuais no componente, que caso supere limites de resistência do material pode provocar a ruptura da peça. Sabe-se que o estado de tensões residuais no material pode sofrer modificações após a sua instalação, seja por condições de operação ou fatores externos (por exemplo, um deslizamento de terra que atinge as vizinhanças de um duto de transporte de petróleo). Deste modo, monitorar as tensões residuais que atuam na peça é uma atividade crucial para garantir a segurança de pessoas e do ambiente em que se insere, além de evitar intervenções emergenciais que seriam muito custosas para a indústria. Neste contexto, insere-se o Método do Furo Cego para medição de tensões residuais, que apresenta como vantagens em relação a outras técnicas concorrentes um custo acessível de operação, possibilidade de portabilidade para inspeção em campo, além de ser um método que já foi amplamente estudado cuja aplicação é consolidada tanto em ambientes industriais quanto em laboratórios. Ademais, permite verificar tensões residuais macroscópicas, que são as de maior interesses de engenharia. No entanto, o resultado de medição deste método é sensível à produção do furo, devido ao fato que a furação sempre introduzirá uma tensão residual oriunda da usinagem.

Objetivos

Recentes atualizações na norma ASTM E837 – 13ª, que fornece instruções sobre a aplicação do Método do Furo Cego, permitiram que a faixa de parâmetros de corte fosse estendida. Este trabalho visa fornecer dados acerca de novas combinações de parâmetros de corte (rotação e velocidade de avanço) que minimizem a tensão residual oriunda do processo de usinagem e consequentemente diminua a invasividade do procedimento de inspeção, de forma que sejam fornecidos valores de tensão medidos mais próximos ao valor do estado de tensões originais em dutos de petróleo e gás. Tais dados servirão para melhorias no módulo de furação do equipamento de medição de tensões residuais MTRES desenvolvido pelo LABMETRO/UFSC que são previstas para futuros desdobramentos do projeto.

Metodologia

Medições de tensão residual através do Método do Furo Cego foram executados usando como máquina-ferramenta o centro de usinagem de 5 eixos Hermle C42U, no qual foram acoplados o *electrospindle* Minitor SFIDA MZ01 e o módulo de controle Minitor SFIDA MT01CP. Foram escolhidos os seguintes parâmetros de corte: rotações de 25.000 e 40.000 rpm; velocidades de avanço de 10 e 20 mm/min. As ferramentas de corte utilizadas foram fresas de topo reto revestidas com TiAlN, de dois e quatro gumes. Os materiais dos corpos de prova empregados foram materiais largamente utilizados na indústria: aço carbono SAE1020, aço inoxidável austenítico AISI304L e liga de alumínio AA6061. Os principais atributos analisados foram a forma e dimensão do cavaco através de microscopia eletrônica de varredura; medição de tensões residuais induzidas pela usinagem através do Método do Furo Cego aliado à interferometria *speckle*; indícios de alterações na microestrutura nas vizinhanças do furo através de medições de microdureza; finalmente, perfil do furo obtido através de microscopia óptica. Estes atributos foram analisados para cada material e combinação de parâmetros de corte tendo em vista uma solução de compromisso entre boas características de usinagem e adequação ao uso do Método do Furo

Cego com a interferometria *speckle*. Análises de variância foram utilizadas para avaliar as maiores fontes de variação dentre os parâmetros de corte na introdução de tensão residual, enquanto testes pareados de Welch foram empregados para verificar variação significativa da microdureza devido ao processo de furação.

Resultados e Discussão

Foram observados que cavacos longos são bastante danosos à aplicação da técnica de interferometria *speckle* devido ao fato que propiciam a raspagem da superfície vizinha ao furo, causando a perda de correlação e inutilizando os dados de medição. Cavacos de AISI 304L e AISI 1020 apresentaram uma estrutura com lamelas bem definidas, das quais pode-se depreender que a condição de corte através do deslizamento de planos de cisalhamento foi alcançada, sendo um indicativo de condições favoráveis de corte de material. Cavacos de AA 6061 apresentaram aspecto bastante viscoso, provavelmente devido à facilidade com a qual este material se adere à superfície da ferramenta de corte e dificulta sua saída da zona de corte.

Verificou-se que a ferramenta de quatro gumes produziu, em geral, menor nível de tensões residuais do que a ferramenta de dois gumes, além de ter menor desvio padrão da amostra. Ao menos uma combinação de parâmetros de corte produziu baixos valores absolutos de tensão residual induzida pela usinagem para todos os materiais, com valores máximos e mínimos dentro da faixa ± 10 MPa. A velocidade de avanço foi apontada na maior parte dos casos como o fator mais importante na introdução de tensões residuais induzidas pela usinagem. Foram detectados aumentos nos valores de microdureza dos materiais testados na maior parte dos casos quando houve alteração significativa, indicando um baixo aquecimento da peça apesar do uso de altas rotações. O perfil do furo obtido com as ferramentas selecionadas apresenta melhores características para aplicação do Método do Furo Cego do que a fresa dental atualmente empregada pelo módulo de furação do MTRES.

Conclusões

Resultados satisfatórios quanto à introdução de tensões residuais induzidas pela usinagem foram encontrados e as melhores combinações de parâmetros de corte foram selecionados para cada material. Estes resultados também se apresentaram adequados do ponto de vista da usinagem, apresentando formação de cavaco mais favorável do que processo atual empregado pelo dispositivo de furação do MTRES devido ao maior avanço por gume, portanto com esmagamento de material e fricção entre ferramenta de corte e peça menos intensos.

Ademais, múltiplos furos foram feitos com uma única fresa de topo reto sem significativos aumentos nos níveis de tensão residual introduzidos pela usinagem para uma dada combinação de parâmetros de corte, indicando que o desgaste sofrido pela ferramenta selecionada é bem menos agressivo do que a atual fresa odontológica que é descartada após único uso. As fresas de topo reto produziram uma geometria de furo mais adequada àquela exigida pela norma, com cantos vivos e geometria mais cilíndrica. Utilizando a configuração experimental deste trabalho, notou-se que a rigidez do módulo de furação do MTRES requer melhoras, pois exerce grande influência na qualidade do furo produzido e na dispersão dos resultados de medição de tensão residual.

LIST OF FIGURES

LIST OF TABLES

LIST OF ABBREVIATIONS AND ACRONYMS

ABNT	Brazilian National Standards Organization
AISI	American Iron and Steel Institute
ANOVA	Analysis of Variance
ASM	American Society for Metals
ASTM	American Society of Tests and Materials
CARD3	Load Evaluation in Ducts from Residual Stresses
CVD	Chemical Vapour Deposition
DOE	Diffractive Optical Element
EDM	Electrical Discharge Machining
ESPI	Electronic Speckle Pattern Interferometry
HDM	Hole-Drilling Method
ISO	International Organisation for Standardization
LABCONF	*Laboratório de Conformação Mecânica*
LABMETRO	*Laboratório de Metrologia e Automatização*
LCM	*Laboratório de Caracterização Microestrutural*
LCME	*Laboratório Central de Microscopia Eletrônica*
MTRES	Residual Stress Measurement Device
PVD	Physical Vapour Deposition
SEI	Secondary Electron Imaging
SEM	Scanning Electron Microscopy

UFSC	Federal University of Santa Catarina
UNIFEBE	*Centro Universitário de Brusque*

LIST OF SYMBOLS

LATIN SYMBOLS

$\bar{a}, \bar{b}$	Calibration constants accounting the hole depth [-]
A, B	Calibration constants in Kirsch's analytical solution [-]
a_p	Depth of cut [mm]
A_p	Nominal cross-sectional area [m^2]
b	Uncut chip width [mm]
d_f	Degrees of freedom [-]
d_{dr}	Drill diameter [mm]
E	Elasticity modulus [GPa]
f	Feed [mm]
f_z	Feed per tooth [mm]
F_c	Cutting force [N]
F_f	Thrust force [N]
F_p	Passive force [N]
F_{crit}	Critical F-ratio coefficient [-]
h	Uncut chip thickness [mm]
h_1	Crushed layer thickness [mm]
h_m	Minimum chip thickness [mm]
h_c	Specific cutting force [GPa]
H_0	Null hypothesis

H_1	Alternative hypothesis
MD	Mean difference [-]
MS	Mean squares [-]
n	Rotational speed [rpm]
n	Number of samples [-]
r	Radius [mm]
r_0	Hole radius [mm]
S	Sample variance [-]
t_a	Actual uncut chip thickness [mm]
t_{crit}	Critical t coefficient [-]
u_r	Radial displacement [mm]
v_c	Cutting speed [m/min]
v_f	Feed rate [mm/min]
z_c	Number of teeth in the cutter [-]

GREEK SYMBOLS

α	Clearance angle [°]
β	Wedge angle [°]
β	Clockwise angle from the x-axis to σ_1 direction [°]
γ	Rake angle [°]
μ	Sample mean [-]
ν	Poisson's ratio [-]
Φ_p	Drilling tool point angle [°]

σ_1	Maximum residual stress [MPa]
σ_2	Minimum residual stress [MPa]
θ	Angle of strain gage from the x-axis [°]

SUBSCRIPTS

$_{0,1}$	Base material
$_{a,b,c,d}$	Cutting parameter combination using two-flute end mill
$_{A,B,C,D}$	Cutting parameter combination using four-flute end mill

CONTENTS

1 INTRODUCTION

1.1 CONTEXT

The aim of predictive maintenance is to spot the degradation mechanism onset and to correct the affected part prior to the structure or component failure. In oil and gas industry, predictive maintenance is an activity of major importance since great amounts of petroleum and its derivatives are daily transported across long distances. In particular, the pipelines safety is a crucial concern, as any significant harm in their integrity may lead to a leakage, having as immediate consequences valuable raw material losses, interruption in the transport network and nearby zone contamination.

In-service pipelines are subject not merely to mechanical stresses originated by the workload; almost always, residual stresses are also present. As they exist in the absence of any external load, residual stresses are often neglected despite the fact that they can play an important role in the failure of mechanical structures [1]. There are four main sources of residual stresses: assembly process, thermal gradients, manufacture process and interactions with the environment [2], which means that the stress state in the material can change during service and should be monitored regularly in order to avoid catastrophic failures.

Pipelines predictive maintenance calls for non-destructive or semi-destructive techniques, i.e. those that do not harm the mechanical structure integrity. Among them, the Hole-Drilling Method (HDM) is one of the most widely employed techniques to evaluate residual stresses, conventionally using strain gages for this purpose accordingly to the standard that endorses this testing procedure, ASTM E837 – 13a: *Standard Test Method for Determining Residual Stresses by the Hole-Drilling Strain-Gage Method* [3]. However, in the past few years strain gages are being successfully replaced by Electronic Speckle Pattern Interferometry (ESPI), since the latter technique allows for non-contact and faster displacement measurements

[4, 5]. Figure 1.1 illustrates an in-field residual stress measurement using a portable interferometer.

Figure 1.1 – In-field measurement of combined stresses in two gas pipeline cross-sections [6].

1.2 THE PROBLEM

The most recent version of the residual stress measurement device MTRES (Figure 1.2) developed by *Laboratório de Metrologia e Automatização* – LABMETRO/UFSC incorporates an air turbine drill, which presents the following drawbacks: low and unstable torque, poor rotational speed control and compressed air supply dependence; rotational speed depends on the material being machined and its average value is around 210,000 rpm [7]. Furthermore, MTRES employs carbide inverted-cone dental end mills without coating; these cutting tools are used to drill only a single hole to assure its quality, since the cutting tool suffers severe tool wear as reported by Blödorn [7].

It is worth mentioning that both the pneumatic turbine and the inverted-cone dental end mill have been recommended by the standard over decades, however the configuration yielded by this combination may not deliver the less disturbing drilling procedure due to the resultant unfavourable machining conditions [7].

The current standard version released in 2013 decreased the rotational speed lower bound from 50,000 rpm to 20,000 rpm. Thus, better chip formation can be expected from lower rotational speeds since higher feed per

tooth can be achieved for a given feed rate, approaching the recommended cutting parameters values accordingly to the machining theory.

Another element that can be easily improved is the cutting tool, the inverted-cone dental end mill currently used can be substituted with a square end mill properly designed to metal cutting.

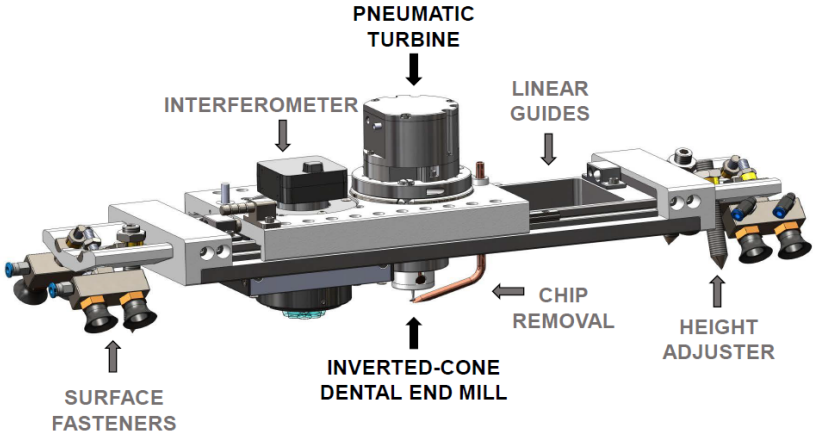

Figure 1.2 – Main elements of the residual stress measurement device with linear guides developed by LABMETRO/UFSC.

1.3 OBJECTIVES

From the aforementioned matters, an important modification in the MTRES design concerns the high speed pneumatic drill replacement, which can be substituted with an electric drill in order to allow a better rotational speed control and higher torques. In addition, coated square end mills were selected as the cutting tools.

The main objective of this work is to test the proposed cutting parameters combinations and cutting tools to provide the best configuration for further MTRES design improvements. This tailored configuration must be a compromise solution between machining attributes and appropriateness to the ESPI utilisation requirements.

To verify the suitability of the proposed drilling process for residual stress measurement purposes, hole drilling experiments were carried out, varying the rotational speed, feed rate, cutting tool and workpiece material. Burr formation was also observed in a preliminary analysis to verify if their size could compromise the measured area. Chips were qualitatively analysed to provide information about chip formation and plastic deformation suffered during this process. Residual stresses introduced by the drilling process were measured through ESPI technique, and their effect on the surrounding material were investigated with microhardness testing.

This work is developed within the CARD3 project (Load Evaluation in Pipelines from Residual Stresses), a partnership between LABMETRO/UFSC and Petrobras.

1.4 DISSERTATION STRUCTURE

This dissertation is divided in the following chapters:

- Chapter 1 – Introduction: an overview of this work, explaining its context, problem and aims;
- Chapter 2 – Residual stresses and their measurement: a background about residual stresses and the main techniques used to evaluate them;
- Chapter 3 – Machining induced residual stresses: a brief review about drilling process, milling cutting tools and machining induced residual stresses in metals;
- Chapter 4 – Experimental planning: a description about materials, methods and experimental design;
- Chapter 5 – Results and discussion: main outcomes from the proposed analyses are presented along with their discussion;
- Chapter 6 – Conclusion: main findings and suggestions for future work.

2 RESIDUAL STRESSES AND THEIR MEASUREMENT

The aim of this chapter is to present a brief overview about residual stresses and their main measurement techniques, focusing particularly on the Hole-Drilling Method combined with Electronic Speckle Pattern Interferometry for strain measurement, since MTRES operating principle is based on these techniques.

2.1 RESIDUAL STRESSES

Residual stresses correspond to the stress state found within the bulk material in the absence of an external loads and are self-equilibrating; in other words, the resultant force and moment must be zero through the whole body [1, 2]. They are an elastic response to an incompatible local strain in the structure, such as a non-uniform plastic deformation, and are created in order to preserve the dimensional continuity of the body [8]. Their importance is often overlooked because residual stresses occur without the application of any external force; depending on the operational conditions a structure is exposed to, particularly in corrosive environments and alternating service loads, such negligence can lead to the component failure, as the residual stresses and mechanical stresses superposition can surpass the material yield strength.

Residual stresses are introduced to mechanical parts by almost all manufacturing processes (some examples are illustrated in Figure 2.1), but they can also be developed during the component service life. The most common mechanisms to produce residual stresses are non-uniform plastic deformations, originated from many manufacturing processes such as machining and forming, also happen in components under operating conditions, such as railway rails or pipelines close to landslide locations. Another mechanism consists of material phase and/or density changes, often in the presence of high thermal gradients, that happen in some manufacturing processes such as welding, casting, quenching, nitriding, among others;

during service life, this alteration may happen as corrosion [8].

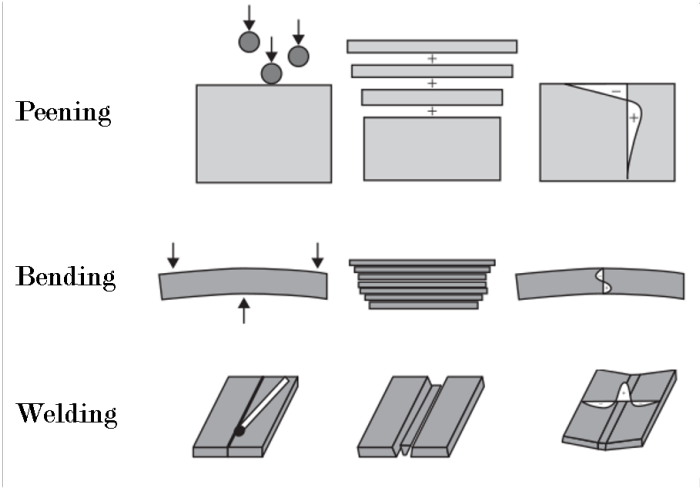

Figure 2.1 – Examples of residual stress distributions caused by manufacturing processes [8].

Three main types of residual stresses can be discerned according to their extent. Residual stresses of the first type have a macroscopic nearly homogeneous characteristic that extends over several grains of the material, and are equilibrated over the whole body. In a body that presents the first type residual stress, any change in the equilibrium state will affect its dimensions. Residual stresses of the second type, also known as structural microstresses, are nearly homogeneous across microscopic small areas of a material, affecting one grain or part of grain. They are equilibrated across a certain number of grains; if the equilibrium of forces and moments is disturbed sufficiently, macroscopic changes in the dimensions of a body may be produced. Residual stresses of the third type are inhomogeneous across submicroscopic small areas and range over several atomic distances within a grain. Forces and moments are equilibrated over a small portion of the grain. Third type residual stresses do not provoke macroscopically noticeable modifications in the body dimension [1].

Residual stresses can bring beneficial or prejudicial effects to the material behaviour depending on their sign and location, impacting significantly on material strength, fatigue life and dimensional stability [8]. Compressive residual stresses are known to have a favourable effect as they improve fatigue life, retard crack propagation and delay stress corrosion. On the other hand, tensile residual stresses generally have the opposite effect, jeopardizing the component performance [2]. For this reason, monitoring periodically the actual residual stress state in a component is vital to keep a safe and reliable operation in many engineering applications.

2.2 RESIDUAL STRESS MEASUREMENT TECHNIQUES

The inherent locked-in nature of residual stresses makes their measurement a challenging task. Many residual stress measurement techniques have been developed over the years to assess residual stresses either quantitatively or qualitatively; they vary in equipment costs, operational costs, complexity, time required to acquire data and suitability for a given measurement duty [9]. A comparison between many methods is provided in Figure 2.2 concerning to their penetration and spatial resolution. James [2] suggests that the main parameters that should be analysed to make a proper selection are:

- nature of the material (crystallographic structure, chemical composition, phase, etc.);
- type of residual stress (microstress or macrostress);
- residual stress gradient (through the thickness of the part or only near the surface);
- geometry of the component and the zone to be studied (depth, dimension and shape of the region of interest);
- where the measurement is carried out (on-site or in laboratory);
- type of intervention (destructive or non-destructive);
- measuring time rates;
- precision and repetitiveness;
- measurement cost and the price of the equipment required.

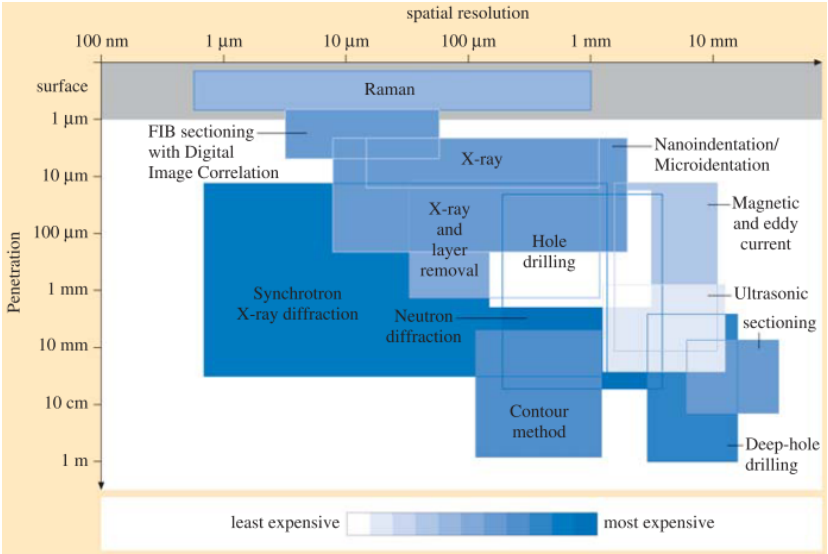

Figure 2.2 – Penetration and spatial resolution for various residual stress measurement techniques [8].

Destructive methods are based on the destruction of residual stress equilibrium state by material removal or cutting, provoking a relaxation (deformation) that is typically elastic. For this reason, a linear relationship can be established between the released residual stress and the deformation magnitude. The relaxation itself is not measured, but rather the consequences of this effect, being the strain change the most used analysed parameter. Among destructive methods, there are semi-destructive methods that introduce little harm to the structure or component, which remains fully functional even after the intervention. The most widespread totally destructive methods are the Sectioning Method and the Contour Method, while the most extensively used semi-destructive methods are Ring-Core technique and the Hole-Drilling Method [10]. These techniques are sensitive to macroscopic stresses, which are the most important residual stresses for engineering applications [2].

Sectioning Method (Figure 2.3) is based on the principle that residual stresses are relieved by cutting the component in several strips of smaller cross sections. Heat and plasticity effects during the cutting process must be minimal to mitigate the contamination of the original residual stress value. Released strains are commonly measured with mechanical or electrical gauges. This method is more suitable when longitudinal stresses alone are significant and allows the measurements of residual stress profiles accurately, being largely used to evaluate residual stresses in steel and aluminum structural components [10, 11].

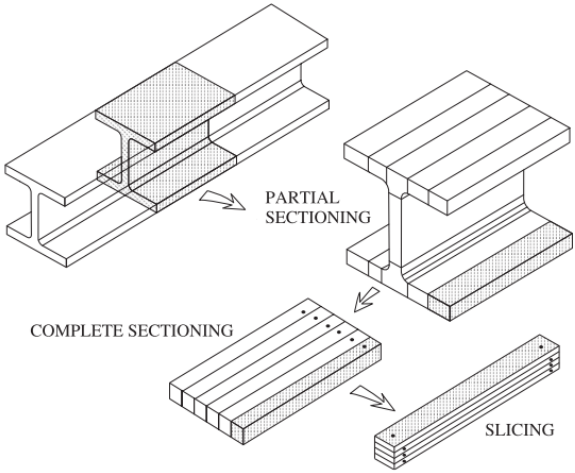

Figure 2.3 – Sectioning method [8].

The recently developed Contour Method (Figure 2.4) is a full-field technique that consists of cutting through the component cross section using a wire electrical discharge machining, measuring the freshly cut surface heights profile with a coordinate measuring machine or a laser profilometer. The cut releases residual stresses that provoke deformations in the surface, pulling inwards for tensile stress and bulging outwards for compressive stress. The original residual stresses normal to the cut are determined using finite element method to calculate the stress required to flat the deformed surface. This novel technique great advantage is the residual stress 2D map generation [8].

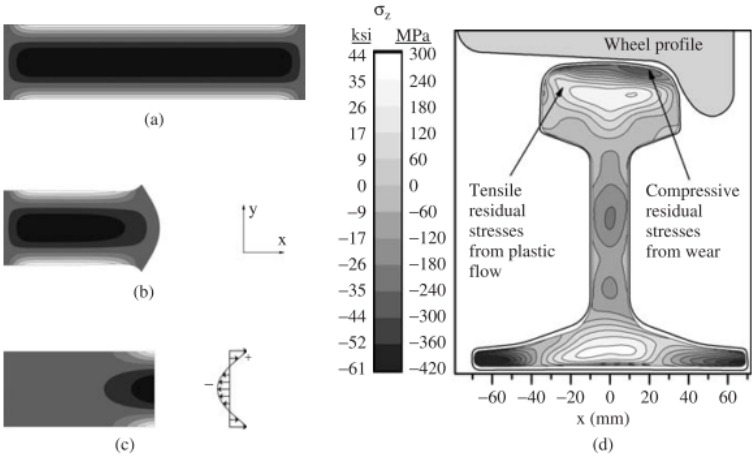

Figure 2.4 – Contour Method [8].

Non-destructive methods operating principle relies on the relationship between physical or crystallographic parameters and residual stresses, typically little or no material removal is necessary. However, some methods must need some "stress free" reference state and intact residual stress that are hard to obtain with reliability. Depending on the technique, both microscopic and macroscopic residual stresses can be inspected. The main non-destructive techniques are: X-ray diffraction, neutron diffraction, ultrasonic and magnetic methods [2, 8]. Both magnetic and ultrasonic methods can be used to measure all three types of residual stresses, however they are not able to make a clear distinction between them [2].

Both diffraction methods are based on measuring lattice strains that arise from modifications in the polycrystalline material interplanar spacing and they can be used to study all three types of residual stresses with high spatial resolution. While X-ray diffraction allows the residual strains inspection on the material surface, neutron diffraction measures residual strains within a volume of the specimen [2, 8].

Ultrasonic techniques use variations in the ultrasonic waves flight time differences, and a relationship between the wave velocity in the medium

and the residual stress state can be established. However, the flight time is not only affected by stresses, but also by other microscopic characteristics such as the grain size, presence of voids and other phases, crystallographic texture and so on. These elements decrease measured residual stress accuracy and makes this method suitable to very specific cases. It allows the measurements in a few seconds within volumes of several cubic millimetres [2, 8].

Magnetic methods take advantage of the interaction between magnetisation and elastic strain in ferromagnetic materials. Among magnetic methods, the most popular uses the Magnetic Barkhausen Noise, that consists in the measurement of abrupt magnetic re-orientations number and magnitude made by magnetic domains during magnetization reversal. The application is limited to ferromagnetic materials, but measurements can be performed in seconds with spatial resolutions smaller than a millimetre [2, 8].

Even though non-destructive techniques seem to be the best option to inspect in-service components due to their non-invasive approach, they often require a delicate and expensive hardware that must be operated in laboratory conditions, which makes them unsuitable to measure in harsh environments.

Semi-destructive methods are a good compromise solution as they avoid the component total destruction and provide information about greater depths than non-destructive approaches. As said beforehand, the main semi-destructive techniques are the Ring-Core Drilling and the Hole-Drilling Method.

The Ring-Core Method consists of ring core drilling, typically 15–150 mm internal diameter; the relieved strains are measured on the surface inside the ring and allow the inspection depth range between 25–150% of the internal diameter. Compared to the Hole-Drilling Method, the Ring-Core Method presents higher sensitivity to the relieved strains and insensitivity to minor diameter errors or eccentricity at the cost of more damage and invasiveness to the structure [12].

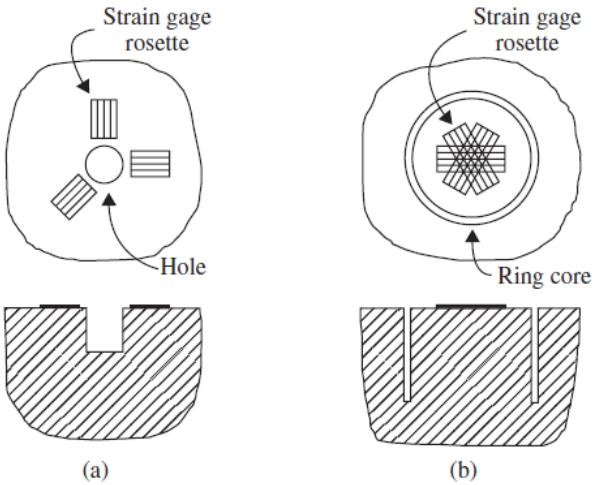

Figure 2.5 – Main semi-destructive techniques: (a) Hole-Drilling Method and (b) Ring-Core technique [8].

The Hole-Drilling Method is probably the most well-established and largely used technique to measure residual stresses; it consists basically in the stressed material local removal by drilling a hole, typically 1-4 mm diameter, to a depth approximately equal to its diameter, followed by the strain relief measurement in the adjacent material. Even though the relieved strains decay quickly with their depth from the surface, this technique allows a much more localized residual stress measurement than the Ring-Core Method [12]. Further detail about the Hole-Drilling Method follows in the forthcoming topic, due to its popularity and use in the residual stress measurement device developed by LABMETRO/UFSC.

2.3 HOLE-DRILLING METHOD

The Hole-Drilling Method is based on the pioneering work of Mathar [13] and since then has become the most widespread general-purpose technique to measure residual stresses due to its relative simplicity, low cost, versatility, compactness and consequent portability, being an effec-

tive outside-lab solution [14]. Currently, this procedure is endorsed by the ASTM E837 – 13a [3] and can deliver quickly reliable results of uniform stresses in workpieces that have a thickness comparable to the tool diameter; otherwise, if the workpiece thickness is much greater than the tool diameter, both uniform stresses and non-uniform stresses can be obtained. In practice, the method can provide satisfactory results if the residual stresses do not exceed about 80% of the material yield stress when measuring a thick workpiece, since a linear-elastic behaviour is assumpted [3]. Figure 2.6 shows a schematic comparison between before and after the drilling, and the effect in the surrounding material detected by the measuring technique.

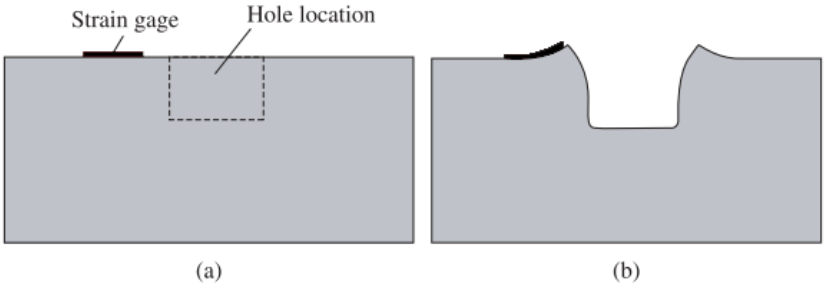

Figure 2.6 – Schematic cross-sections around a hole drilled into tensile residual stresses (a) before hole drilling and (b) after hole drilling [8].

For the application of the Hole-Drilling Method to determine residual stresses, the following assumptions are made: the material is elastic and isotropic; the measured stresses are below the elastic limit of the material; the stress normal to the surface component is negligible; in each layer removed, the in-plane stress gradients are small; the shear forces are negligible between layers and the hole bottom is flat [3, 15]. This method is constituted by three main features: drilling process, strain measurement and computational technique.

Conventionally, deformations are measured with strain gages, which are being replaced by full-field optical techniques [8, 9]. Optical methods present features that make their application for residual stress measurements attractive: they are non-invasive techniques and allow for full-field

data obtained at high speeds. The former feature provides a measurement that does not cause any deformation or damage to the specimen and avoids demanding surface preparation; the latter feature regards the great amounts of 2D data acquired at light speed that make possible complex residual stress analyses [4, 5]. Particularly for the Hole-Drilling Method, Beghini *et al.* [16] affirms that optical methods are more adequate than the strain gage methods if significant plastic effects are present since the whole strain field can be measured. The most widespread optical techniques to measure residual stresses are: ESPI, Moiré interferometry and digital image correlation [5]; the first technique will be detailed, since the investigation to be developed by this work uses ESPI.

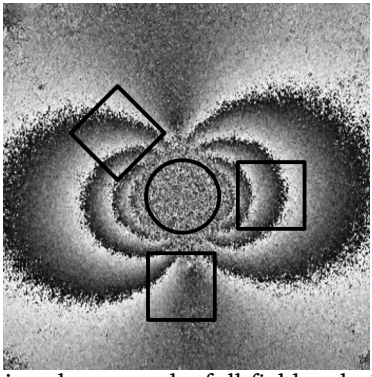

Figure 2.7 – Comparison between the full-field technique ESPI and strain gage data [8].

The ESPI technique combines speckle interferometry with electronic detection and processing. The *speckle effect* results in a high contrast fine-scale granular pattern characterized by the random distribution of scattered light that arises when a rough surface is illuminated with laser light, shown by Figure 2.8. This distribution is sensitive to changes in the illumination and observation geometry, rotation and diffuse surface displacement, laser wavelength and medium refractive index. These features make speckle suitable to measure rough surface out-of-plane and in-plane deformation components, 3D shapes and surface displacements derivatives, since the random distribution that characterises this pattern can be deterministically

changed by displacements and rotations of the diffuse body that scatters incident light [6]. This is possible because each speckle is ideally surrounded by an unique combination of speckles, creating a particular signature for each measured point.

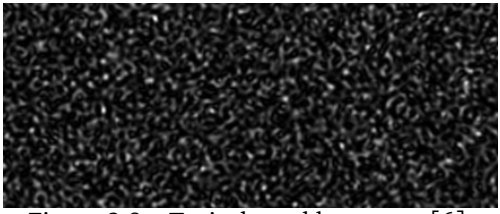

Figure 2.8 – Typical speckle pattern [6].

ESPI allows displacement, deformation and vibration measurements typically in fraction of micrometres. This technique enable the comparison between two non-simultaneous wave fronts generated by rough or curved object two different states. An interferometric pattern arises from these wave fronts interference, providing information about the change (vibration, displacement or deformation) that the object experienced, as illustrated in Figure 2.9. Figure 2.10 shows the steps to retrieve information about the change the body suffered from this transformation recorded effect, known as specklegram.

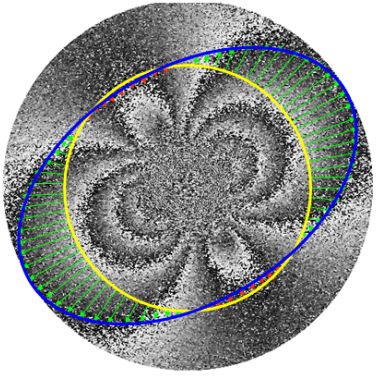

Figure 2.9 – Typical ESPI interferogram of residual stress relief and consequent displacements around a drilled hole [17].

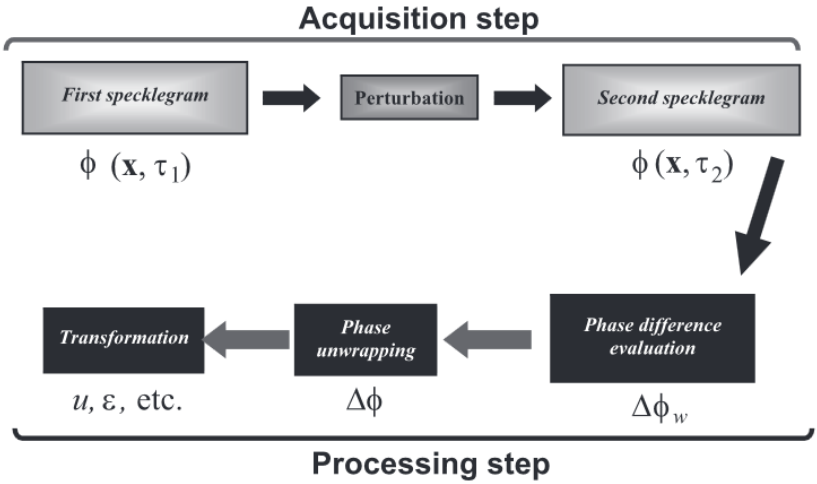

Figure 2.10 – Steps to analyse ESPI interferograms [6].

This technique presents a 5–15% in-lab accuracy, but the test set-up needs interferometric stability: a stiff assembly free of vibration and without significant thermal gradients nearby, since the interferogram is extremely sensitive to the slightest changes in its optical path [5].

Since mechanical stresses are virtually impossible to be measured during operation, their quantification is made based on the relationship between stresses and their consequent strains [6]. Strains arise also on the material surface, making possible their measurement using either strain gages or optical rosettes; in the Hole-Drilling Method, these measurement techniques are sensitive to radial displacements u_r. From u_r, the principal residual stresses σ_1 and σ_2 and their direction β are obtained using the numerical solution developed by Makino and Nelson (1994 *apud* Suterio[19], 2005) from Kirsch's analytical solution in polar coordinates:

$$u_r(r,\theta) = A\, r_0\, \bar{a}\left(\frac{r_0}{r}\right)(\sigma_1+\sigma_2) + B\, r_0\, \bar{b}\left(\frac{r_0}{r}\right)(\sigma_1-\sigma_2)\,\cos(2\theta-2\beta) \tag{2.1}$$

where A and B are constants related to material elastic properties, Poisson's ratio ν and elasticity modulus E, given by the following equations:

$$A = \frac{1+\nu}{2\,E} \tag{2.2}$$

$$B = \frac{1}{2\,E} \tag{2.3}$$

in which $\bar{a}$ and $\bar{b}$ are dimensionless calibration constants, almost material-independent, that correspond to the relieved strains due to unit stress within the hole depth. These calibration constants are geometric functions obtained from finite element method calculations; the standard provides numerical values for these coefficients according to the rosette type, hole depth and diameter [3, 20].

There are two considerations concerning the drilling process that must be taken into account: the produced hole quality and the additional stresses that may be added by the machining process [14]. The drilled hole features exert a strong influence on the measurement results. If the optical system is not orthogonal to the hole, an error of 17% may be present in the stress value result for a misalignment in the range of ± 15°; furthermore, a circularity error in the order of 2% of the diameter may cause a 4.5% error in the obtained stress value. In addition, the stresses introduced by the drilling process should not surpass 3% of the measured residual stress [21]. Thus, the importance of a meticulous drilling process for a successful residual stress measurement is very clear; however, little attention has been paid to the hole-drilling process, in which often the cutting tool and the cutting parameters are poorly detailed.

3 MACHINING INDUCED RESIDUAL STRESSES

In this chapter, first a brief exposition about the drilling process and the milling cutting tools is provided to understand the particularities associated with the procedure proposed by ASTM E837 – 13a [3]. A summary about residual stresses introduced by machining processes closes the literature review.

3.1 DRILLING

Drilling is a hole-making operation in which the cutting tool with rotational motion enters the workpiece axially and cuts a hole. The hole-making comprises an important family of machining processes, as illustrated by Figure 3.1). Drilling operations produce about 60% of the chips and it is the most time-consuming metal cutting operation, adding up to about 36% of all machine hours [22].

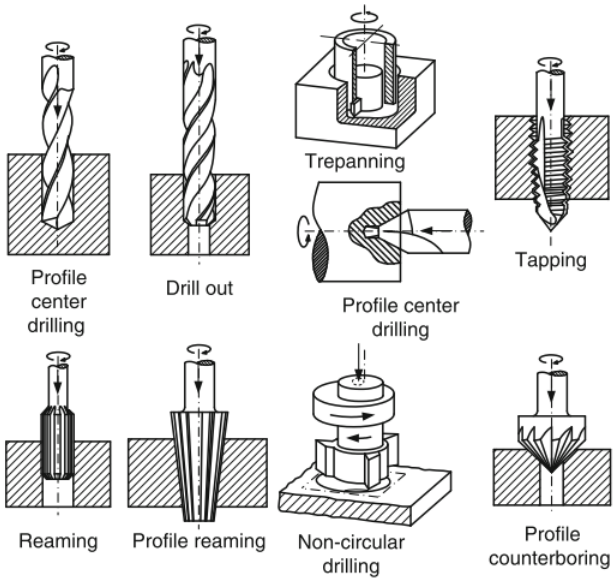

Figure 3.1 – Examples of basic drilling operations [23].

3.1.1 Drilling regime

The prime parameters that constitute the solid drilling regime (Figure 3.2) are the cutting speed and the cutting feed. In drilling, the cutting speed v_c [m/min] varies along the cutting edge, since the rotating point linear velocity is proportional and perpendicular to the rotation radius. The maximum v_c obtained at the tool periphery is given by Eq. 3.1,

$$v_c = \frac{\pi \cdot d_{dr} \cdot n}{1000} \tag{3.1}$$

where d_{dr} [mm] is the drill diameter and n [rpm] is the rotational speed. The depth of cut a_p [mm] is half the drill diameter in solid drilling.

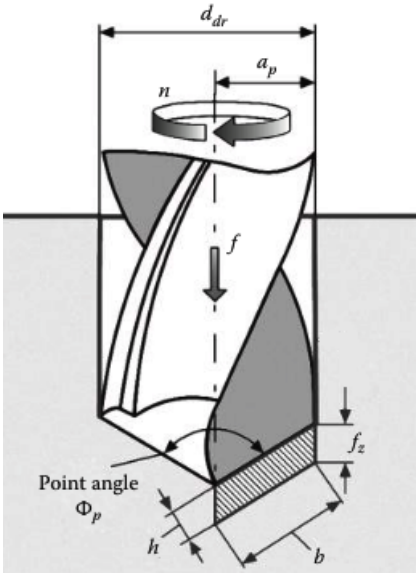

Figure 3.2 – Components of solid drilling regime [24].

The cutting feed f [mm] is defined as the distance in the feed motion direction at which the drilling tool advances into the workpiece per revolution. Feed rate v_f [mm/min] is calculated

$$v_f = f \cdot n \tag{3.2}$$

The cut is defined by ISO 3002/3 standard as the layer of the workpiece material to be removed by a single action of a cutting part. The cut parameters for one cutting tooth are the nominal thickness of cut, the nominal width of cut and the nominal cross-sectional area [24].

The nominal thickness h [mm] (also known as the uncut chip thickness or chip load) is one of the most important parameters in any machining process, because it significantly influences many other features such as tool life, cutting forces and power, contact stresses on the tool-chip interface, amount of plastic information of the layer being removed, among others [25]. The parameter h is calculated as

$$h = f_z \sin\left(\frac{\Phi_p}{2}\right) \tag{3.3}$$

where Φ_p [°] is the drilling tool point angle, while the nominal width of cut or uncut chip width b [mm] is given by

$$b = \frac{a_p}{\sin(\Phi_p/2)} \tag{3.4}$$

and finally, the nominal cross-sectional area or uncut chip cross-sectional area A_D [mm] is obtained by

$$A_D = h \cdot b \tag{3.5}$$

Figure 3.3 shows the main forces developed during drilling. The cutting forces F_c correspond to the circumferential components that act onto the tool rake face at the cutting edge and their direction is perpendicular to the lips projection in the plane normal to the drill axis; they are the most important forces and arise from chip shearing. Thrust forces F_f oppose to the tool feed and have a direction parallel to the drill axis. Finally, the passive forces F_p oppose to the tool radial motion into the workpiece and have a direction parallel to the drill lips projections on the plane normal to the drill axis [26, 27, 28].

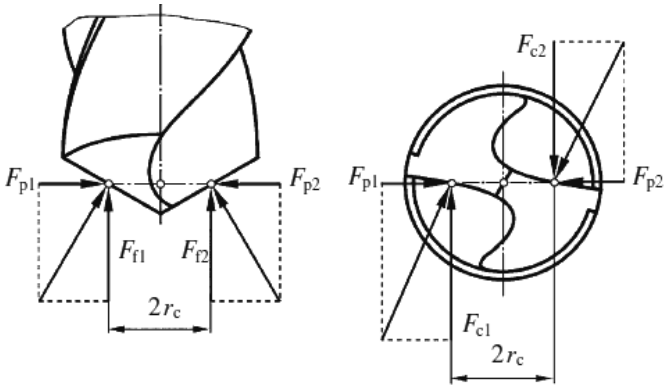

Figure 3.3 – Forces in drilling [26].

3.2 MILLING

Milling principally refers to a machining process performed with a rotating, multi-edge cutting tool which performs programmed feed movements in almost all directions against a workpiece. This operation is very efficient and versatile, allowing the production of prismatic, polyhedrical or free-form shapes, as shown in Figure 3.4; in addition, it is an alternative to produce holes, threads, cavities and surfaces that are traditionally obtained by turning, drilling or tapping [22, 29].

The intermittent action of each cutting edge during material removal is an important aspect inherent to all milling operations; each tooth undergoes periodical impacts and thermal cycling due to the interrupted nature of the cut. Each cutting edge cuts during less than half of a revolution of the tool, often only in very small fractions of the cycle, producing in general small chips [22, 26, 28].

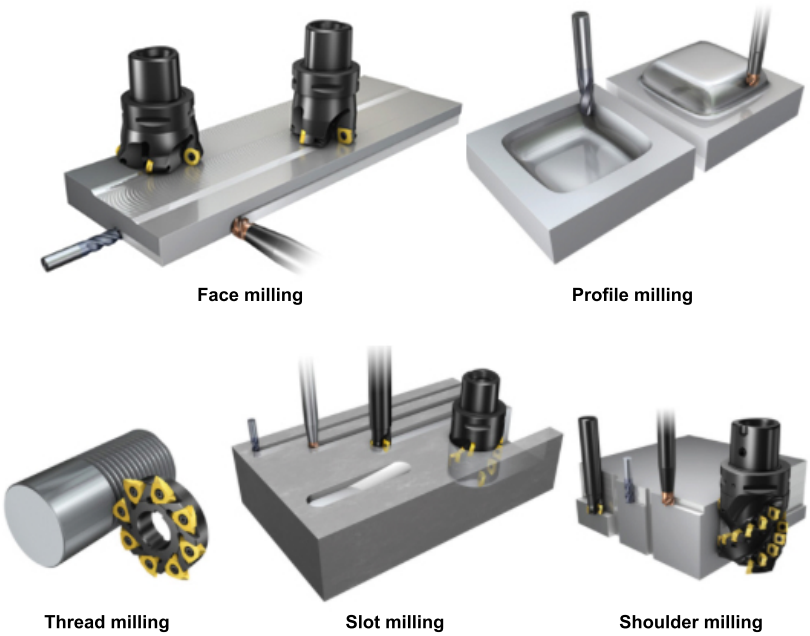

Figure 3.4 – Examples of milling operations [29].

Often, a distinction is made based on the milling direction. If the workpiece feed direction is the same as that of the cutter rotation at the area of cut, up-milling is being performed (Figure 3.5b); the milling cutter enters the workpiece at null theoretical undeformed chip thickness, which increases until the end of the cut. In this case, rubbing and burnishing effects with friction, high temperatures and work-hardened surfaces are present. Otherwise, when the feed direction of the workpiece is opposite to that of the cutter rotation at the area of cut, the operation is called down-milling (Figure 3.5a); the milling cutter enters the workpiece at the maximum undeformed chip thickness and it will decrease to zero until the end of the cut. The large chip thickness helps to keep lower burnishing effects, with less heat and work-hardening [26, 29].

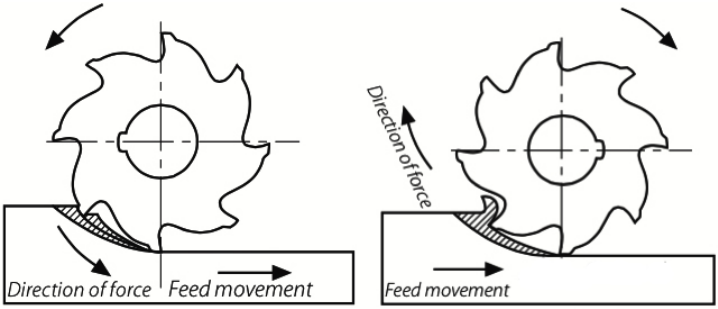

Figure 3.5 – Milling direction: (a) down-milling and (b) up-milling [30].

3.2.1 Milling cutting tools

Many different shapes of milling cutting tools are available for different uses. The most popular are, by far, end mills and milling cutters, shown in Figure 3.6. While milling cutters are often developed for a specific purpose, end mills are versatile cutting tools that can be used for a variety of applications (face milling, shoulder milling, slot milling, plunge milling, profile milling, chamfering, threading and drilling, among others) due to the wide range of diametrical sizes and design characteristics [29]. The main geometrical parameters of an end mill are illustrated in Figure 3.7.

Figure 3.6 – Most common milling cutting tools: (a) Milling cutters and (b) end mills [29].

The number of flutes is a significant parameter that should be taken into account when selecting an end mill; two to four flutes end mills are the

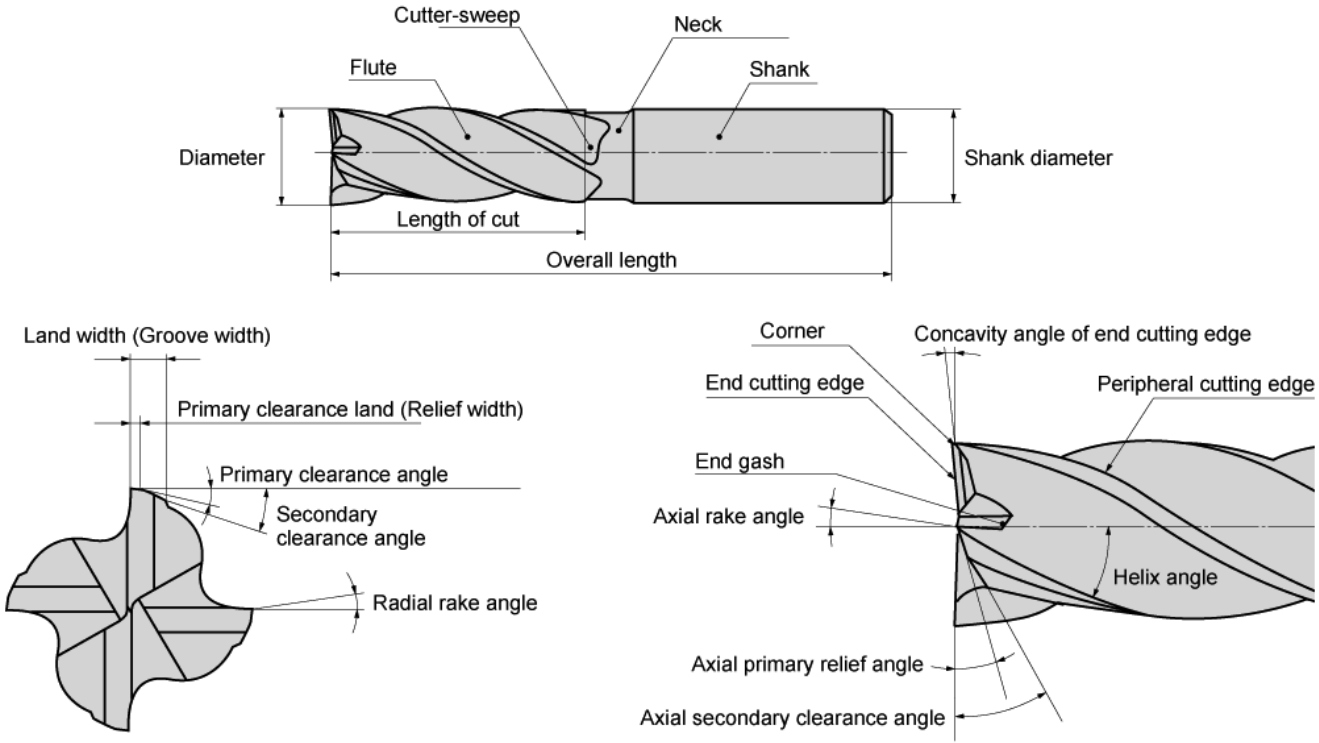

Figure 3.7 – End mill geometry [31].

most common types for small diameter tools, whereas larger diameter tools may have six, eight or more flutes. The fewer the flutes, the more material is removed with each tool rotations, making rougher cuts with greater chip loads that prevent heat from building up. More flutes favours the creation of smoother surface finish. Increasing the flute number improves flexural rigidity due to higher cross-section area, but on the other hand decreases the space for chip ejection [31, 32]. The number of flutes is related to an important parameter, the feed per tooth f_z [mm], defined as

$$f_z = \frac{v_f}{z_c \cdot n} \tag{3.6}$$

where z_c is the number of teeth in the cutter, which is equal to the number of flutes in an end mill.

Among the geometric parameters (Figure 3.8), the most important concerning machining induced residual stresses are clearance angle, rake angle and tool edge radius. The clearance angle α is the angle between the workpiece surface and the tool flank, responsible for diminishing the friction between these elements. If clearance angle is too small, the wedge does not penetrate in the workpiece and the wear is intensified, making the tool blunt precociously. If the clearance angle is too large, the tool mechanical resistance is reduced and it may chip easily [23, 33].

The rake angle γ can be positive, null or negative, being the main responsible for the metal cutting. The wedge stability strongly depends on the rake angle magnitude. When the rake angle is very positive, lower cutting and feed forces are required to produce chips, also better surface finishing is achieved; however, it tends to produce a continuous chip and the wedge becomes too fragile and susceptible to break. Negative rake angle favours tool stability, but plastic deformation is increased, demanding higher cutting forces and exposing the wedge to severe thermal loads [23, 33].

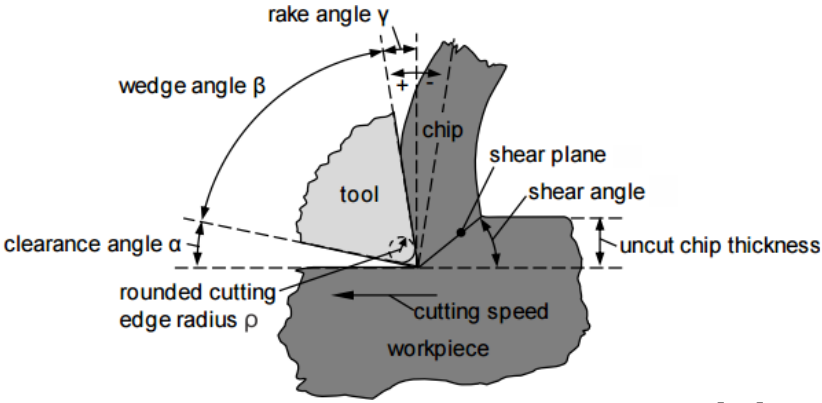

Figure 3.8 – Chip formation and tool geometric parameters [34].

The cutting edge radius ρ (Figure 3.9) influences the separation of the total uncut chip thickness h into two components, the actual uncut chip thickness t_a and the crushed layer thickness h_1 caused by the round part adjacent to the tool flank. When $h/\rho \geq 10$, the cutting tool can be considered perfectly sharp; otherwise, the material is significantly burnished by the tool and the cutting edge radius influences must be taken into account [33].

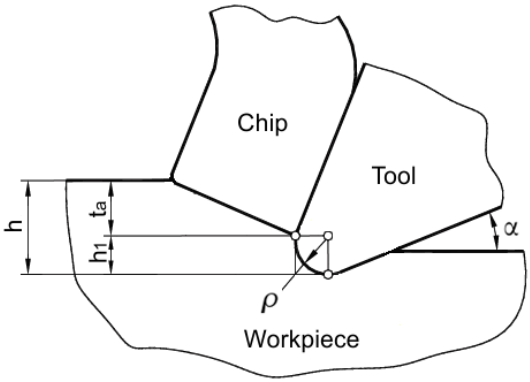

Figure 3.9 – Cutting edge radius and chip thickness [33].

3.3 CHIP FORMATION

During cutting processes, the chip formation consists of the cutting edge penetration into the workpiece material, which suffers elastic and plastic deformation until the maximum permissible material shear stress is reached and the material begins to flow, forming a chip; it is worth mentioning that the chip formation will take place if the minimum chip thickness h_m is surpassed [23].

A schematic representation of the chip formation (continuous chip, for the sake of didactics) is shown in Figure 3.10 in which four zones constitute a continuous plastic deformation. Simple shear provokes the transition from the workpiece structure (a) to the chip structure (b). Small deformations on the shear plane are able to produce material detachment during machining of brittle materials, whereas in a material with higher deformability the detachment begins in the front of the cutting edge in zone (e). Great amounts of deformation in the surroundings of the rake face (c) and the cut surface (d) arise from the combined action of tensile stresses, perpendicular active pressure and high temperatures in the detachment zone.

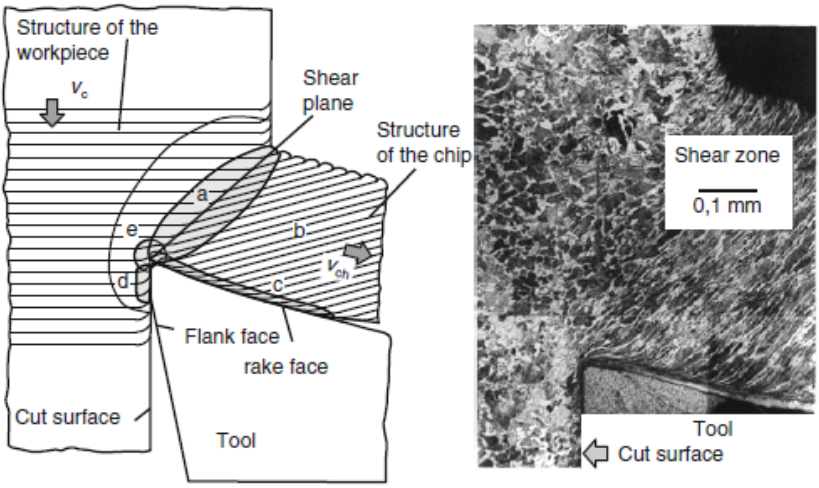

Figure 3.10 – Chip initiation [23].

Depending on the stress direction and magnitude, the material behaviour can be either tough or brittle; hence, chip formation mechanism is strongly influenced by these variables. The stress direction is defined by the tool normal rake angle, tool cutting edge angle and tool cutting edge inclination, while the magnitude of a stress is affected by the cutting speed, feed rate and depth of cut [23, 35]. Interactions between factors that influences chip formation are summarised in Figure 3.11.

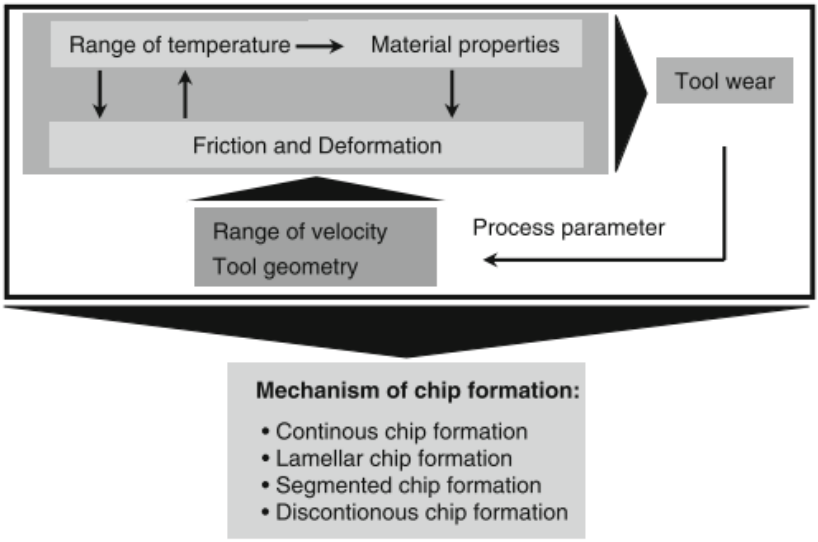

Figure 3.11 – Influences during chip formation [23].

The chip formation mechanisms that arise from this set of elements are illustrated in Figure 3.12. Continuous chip formation occurs when an evenly deformed material slides off along the rake face in temporally highly uniform friction conditions (constant speed in a stationary flow) between the chip and the tool, as a consequence of positive rake angles, low undeformed chip thickness and an uniform, high ductility workpiece material [23, 35].

Lamellar chip formation is a continuous, periodic mechanism characterized by an unevenly material deformation, in which the lamellae arise from thermal or elastomechanical processes with a high formation frequency in the kHz range that results in cleavages or concentrated shear

bands. Lamellar chips are often produced from highly ductile workpiece materials with an increased strength, in particular at high cutting speeds [23, 35].

Segmented chip formation is a discontinuous mechanism that presents slightly connected elements that are separated in the shear plane and fused immediately after; chip segments are characterized by significant differences in the degree of deformation, occurring mostly by the use of negative rake angles, lower cutting speeds and higher chip thickness [23, 35].

Discontinuous chip formation occurs in materials with very brittle properties or when predefined slide paths are present due to profuse inhomogeneities; bits of the workpiece material are ripped up from the bulk without significant deformation, consequently the freshly machined workpiece surface is a result of these small breakages [23, 35].

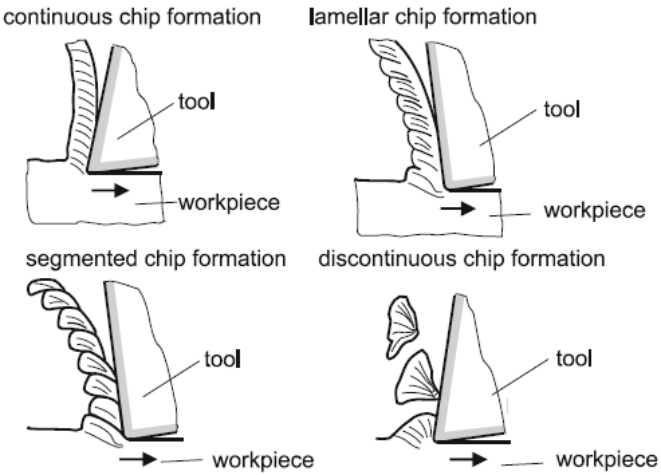

Figure 3.12 – Chip formation mechanisms [35].

3.4 SIZE EFFECT

Size effect occurs when the cutting edge radius becomes comparable to the cutting thickness. With this configuration, cutting happens with a highly negative rake angle and the proportion between the cutting thickness and cutting edge radius determines the chip formation mechanism, as shown by Figure 3.13. Chip will not be formed if the cutting thickness is smaller than the minimum chip thickness; in this circumstance, the material undergoes an elastic-plastic deformation known as ploughing, without forming chips effectively. As the cutting thickness approaches and surpasses the minimum chip thickness, ploughing decreases and chips are efficiently produced [36, 37, 38, 39].

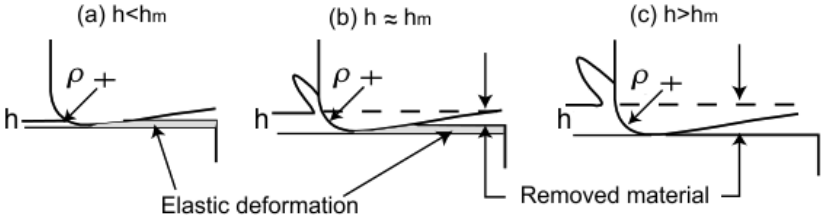

Figure 3.13 – Effect of the proportion between minimum chip thickness [38].

The dramatic increase in specific cutting force during machining with small cutting thickness happens due to the increasing specific shear energy caused by ploughing and actual chip thickness accumulation, that keeps building up until the material removal can take place [40].

Oliveira *et al.* [41] suggest that any minimum chip thickness can be within 1/4 and 1/3 of the cutting edge radius, regardless of the workpiece material. In processes dominated by size effect, chip formation with intermittent nature may arise from the several revolutions made by the cutting tool without properly forming a chip, which may overload tool bearings or bend and even break the cutting tool [42, 43]. Determination of micromilling cutting parameters cannot be based on conventional milling information since size effect takes place concomitantly to the micro end mill low strength [36].

3.5 MACHINING INDUCED RESIDUAL STRESSES

During metallic materials chip-forming machining process, elastic and plastic deformations, lattice imperfection variations and heat production occurs near the workpiece surface [44]. A large amount of the power consumption is converted into heat in the cutting edge surroundings due to frictional effects in the interface tool-workpiece and the plastic deformation of material being removed [45].

Residual stresses are always originated from ihnomogeneous plastic deformations and/or phase transformations associated to volume changes. Plastic deformations due to forces perpendicular and parallel to the workpiece surface favours the production of compressive residual stresses, while plastic deformations due to local heating tends to generate tensile residual stresses; phase transformations can lead to the development of both compressive and tensile residual stresses depending on the volume changes and plastic deformations associated with [44]. Figure 3.14 explains the formation of thermally and mechanically induced residual stresses, while Figure 3.15 focuses on the chip-forming relationship with residual stresses.

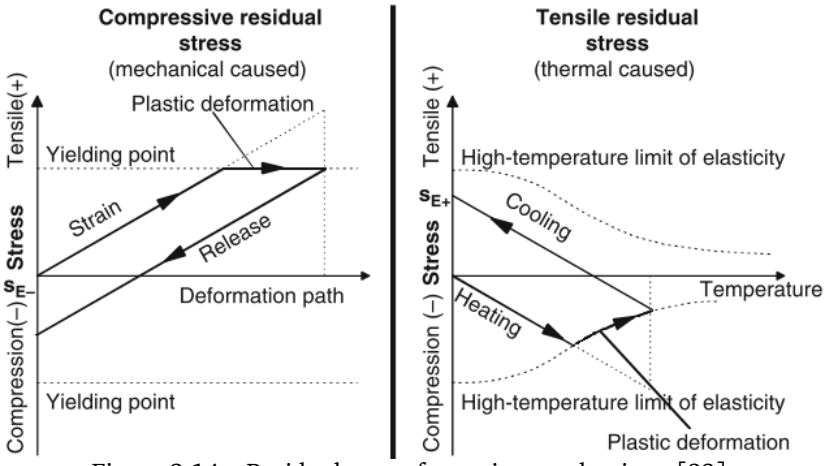

Figure 3.14 – Residual stress formation mechanisms [23].

Heat generation influences strongly the cutting tool performance

and is, concomitantly, a consequence of its characteristics. Furthermore, it affects strongly the freshly cut work surface quality, the material properties and the residual stress state due to the severe temperature gradients developed during the metal cutting [46]. On the other hand, the heat generated can be beneficial since it decreases the shear stress, facilitating the chip formation and decreasing the plastic deformation in the workpiece. Indeed, Sadat [47] showed that extension of the residual stresses beneath the machined surface increases as the cutting speed decreases, which can be explained by lower temperatures for lower cutting speeds.

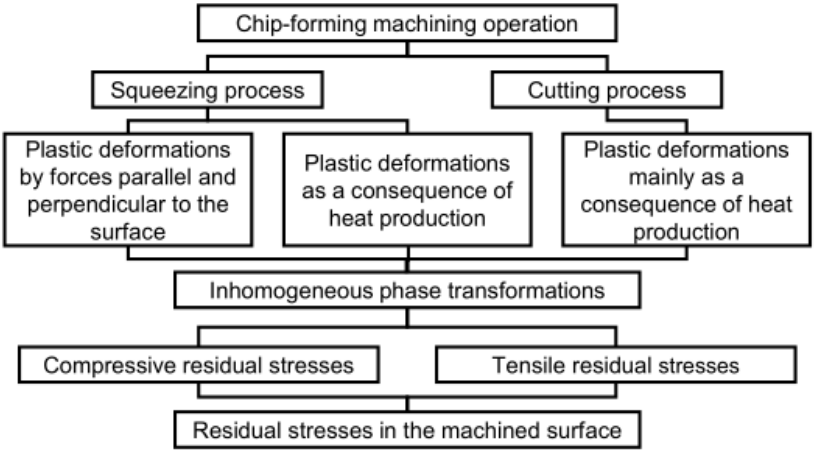

Figure 3.15 – Classification of processes producing residual stresses during chip-forming machining operations [44].

Brinksmeier *et al.* [48] presented a vast compilation comprising residual stresses measurement and causes in many machining processes. Particularly in milling, compressive residual stresses are found due to the considerable plastic deformation associated with this process; furthermore, higher feed rates and rotational speeds increase compressive stresses and their penetration depth, which is also favoured by tool wear. Tool sharpness strong influence in residual stress introduction was also noticed by Jang *et al.* [49] in a study that analysed surface residual stresses through X-ray diffraction in austenitic stainless steel turning and found mostly compressive stresses. El-Khabeery and Fattouh [50] studied residual stresses caused by

milling and concluded that residual stress reached highest values with increasing feed rate, depth of cut and material resistance.

Particularly in the case of the hole drilling process for residual stress measurement purposes, Flaman [51] compared the low-speed end mill to the high-speed drill; it was observed that the high-speed-drilled hole, when compared to the hole obtained by the low-speed end mill, presented a much smoother and straighter sides (Figure 3.16), a much flatter and less rounded bottom; in addition, the first technique resulted in smaller and more equi-dimensional chip. In short, the high-speed drill provided a hole with better characteristics to be used to measure residual stresses.

Later, Flaman and Herring (1985 *apud* Grant *et al.*[14], 2006) studied four drilling techniques, comparing induced stresses, hole geometry and controllability, portability and ease of use. The author concluded that the drilling with low-speed modified end mill was the only inadequate technique as high stresses were produced; the drilling with high-speed drill was suitable for most materials, except extremely hard ones.

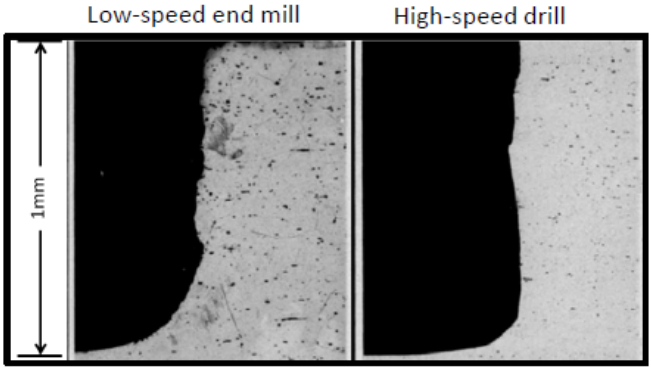

Figure 3.16 – Comparison of the low-speed end mill and the high-speed drill [51].

Recently, Steinzig *et al.* [53] tested the Hole-Drilling Method using a two-flute end mill with 1.59 mm diameter, 3 mm/min feed rate and rotational speeds within the range between 2,000 and 40,000 rpm. They observed that chattering possibly caused inadequate holes when using rotational speed below 10,000 rpm and above this limit repeatable residual stress

measurements could be carried out, indicating that high-speed commonly advised by the standard may not be necessarily required.

4 EXPERIMENTAL PLANNING

This chapter details the experimental planning used to achieve the aims of this investigation. An explanation on the standardised drilling process idiosyncrasies opens the chapter to provide understanding about the choices that culminated in the final experimental design, followed by a description about the materials and methods used in this study. Further information in provided in an organic fashion to furnish understanding about the chain of decisions taken during this work development.

4.1 DESCRIPTION OF THE DRILLING PROBLEM

The drilling process recommended by ASTM E837 – 13a [3] should be performed with an carbide inverted-cone dental burr or small carbide end mill; in other words, this machining process is a boring operation with drilling dynamics acting on a milling cutting tool. Besides, rotational speeds must be in the range within 20,000 rpm and 400,000 rpm due to the historical use of high-speed pneumatic turbines by many research groups and companies to measure residual stresses through the Hole-Drilling Method. Despite its widespread utilisation, these rotational speeds are often much higher than the recommended values for this cutting tool material and diameter [3, 54, 55]. Concerning the pneumatic turbine, another relevant aspect is the air compressibility that restrains feed rates to very low values to avoid stalling and unacceptable run-outs. Extremely low feed rates and excessively high rotational speeds combination results in an unfavourable chip formation, the minimum chip thickness is barely reached and the process is dominated by burnishing instead of cutting due to ploughing effects [42].

Concerning the ESPI use to measure strains from which residual stress are calculated, an essential requirement is to free the reference surface from any foreign body between measurement steps, including moisture, chips, burrs, among others. This precaution is taken because these undesired

elements will provoke a change in the acquired image that is not related to strain, leading to spurious data. For this reason, dry machining is obligatory.

Summarising briefly given the problem constraints, dry drilling is performed with an end mill, using very high rotational speeds and fairly low feed rates.

4.2 DRILLING TEST STAGES

Two drilling test stages were performed: screening tests and final tests. Screening tests were drilling operations performed using two and four-flute square end mills in the most difficult-to-machine workpiece among the preselected materials to check technical viability and to reduce the experimental matrix to the most suitable cutting parameters combinations concerning machining aspects and how they relate to the Hole-Drilling Method alongside ESPI application. Residual stress measurements were not performed at this stage. From three rotational speeds and three feed rates, this test outputs are the two best rotational speed and two best feed rates to be used in the next stage. During this first analysis, particular attention was paid to the following aspects:

- the resulting burr around the hole that may act as a noise source in the phase map depending on its extent;
- the chip formation, that provide information about the plastic deformation the material is suffering, and consequently a qualitative evidence about the residual stresses being introduced into the workpiece;
- the chip form, since long and continuous chip may scratch the measuring surface during the cutting tool rotation.

During the second stage in which the final tests were carried out, residual stress measurements through the Hole-Drilling Method were performed in three types of workpieces using the four cutting parameters combination using two and four-flute square end mills. Further detail about the cutting tools, workpiece and cutting parameters are provided in the next

sections.

4.3 WORKPIECES

Three different types of workpieces were used, which are materials commonly used in the industry: AISI 304L austenitic stainless steel, AISI 1020 carbon steel and AA 6061 aluminium alloy. These materials were acquired as flat sheets with 6.35 mm, 6.30 mm and 12.00 mm respectively and their relevant physical properties are shown in Table 4.1.

Table 4.1 – Workpieces physical properties [56].

Property	**AISI 1020**	**AISI 304L**	**AA 6061-O**
Density [kg m^{-3}]	7850	8000	2700
Elastic modulus [GPa]	207	193	69
Poisson's ratio [-]	0.30	0.30	0.33
Tensile yield strength [MPa]	210	205	55
Tensile ultimate strength [MPa]	380	515	125
Vickers hardness [HV]	162	191	50
Thermal conductivity [W m^{-1} K^{-1}]	51.9	16.2	180
Thermal expansion coefficient [$\times 10^{-6}$ K^{-1}]	11.7	17.2	23.0
Thermal diffusivity [$\times 10^{-6}$ m^2 s^{-1}]	13.6	4.1	137.2

The above-mentioned dimensions correspond to the case in which the hole depth is much smaller when compared to the specimen thickness, being denominated as *thick workpieces* by ASTM E837 – 13a [3]. The standard recommends that the minimum thickness should be 5.13 mm for a hole diameter between 1.52 and 2.54 mm to measure uniform stresses in these situations. These sheets were cut into 135 mm strips using plasma cutting; afterwards, these strips were divided equally into 25 mm wide pieces using a band saw. After the cutting process, these 25 mm wide and 135 mm long specimens have undergone a heat treatment to relieve stresses from the previous manufacturing processes in order to assess only the influence from machining induced residual stress introduced by the hole drilling. Heat

treatment certificates can be found in Annex A. The preparation was concluded by spraying the workpieces with a thin white paint layer to produce a matte finish, since a non-reflective surface is desirable in ESPI technique application. In Figure 4.1, workpieces ready to be drilled are shown.

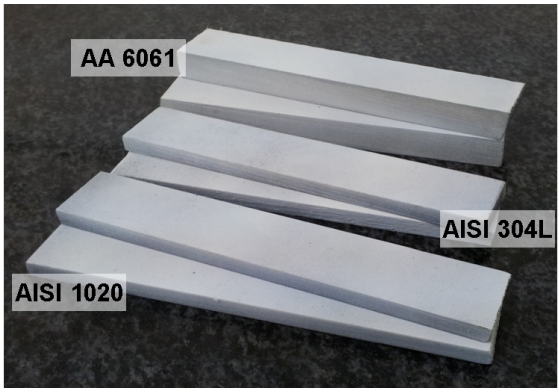

Figure 4.1 – Workpieces after preparation [7].

Austenitic stainless steels, such as AISI 304L, are considered difficult-to-machine materials due to their work-hardening tendencies, high tensile strength, high ductility combined with poor thermal conductivity. High cutting forces are developed during the machining process, accompanied by intense heat generation around the cutting edge [57, 58]. In particular, the combination of high strength and high ductility makes chip breaking a difficult task, propitiating tool vibration that may cause a severe harm to the cutting tool [59].

AISI 1020 is a plain low-carbon steel that consists principally in ferrite, having small amounts of pearlite. Low-carbon steels undergo rapid work-hardening, especially when clean [58]. Ferrite is easily cut and has little contribution to tool wear, but favours built-up edge formation and poor finishing. The main responsibles for tool wear when machining AISI 1020 are pearlite and oxide particles, that have higher hardness and can be very abbrasive to the cutting tool. Nonetheless, plain carbon steels are almost always easily machined than alloys steels of comparable carbon content and hardness [60], having also a thermal conductivity three times higher than

the AISI 304L that removes heat from the cutting zone more efficiently.

AA 6061 is magnesium-silicon aluminium alloy with excellent corrosion resistance that can be machined to a good finish in the cutting fluid absence and are more machinable in the heat-treated tempers than in softer annealed solutions, which are more prone to the built-up edge formation because of melting from heat generation. High cutting speed has a beneficial effect keeping the workpiece cool, as most of the heat generated in a given rotation is removed with the freshly cut chip during the subsequent rotation. Short diffusion times given by the aluminium alloy high thermal conductivity also helps to dissipate heat from the cutting area [60].

4.4 CUTTING PARAMETERS SELECTION

Cutting parameters were selected having the following premises:

- take advantage of the decrease in the rotational speed allowed by the last standard version, from 50,000 to 20,000 rpm;
- propose an evolution from the former MTRES process (0.1–0.2 mm/min feed rates and approximately 210,000 rpm rotational speed), presenting lower rotational speeds, higher and yet moderate feed rates to favour proper chip formation;
- choose rotational speeds within the operating range offered by brushless motors without auxiliary fluid-based cooling subsystem, as they constitute the most likely replacement for the pneumatic turbine, considering that most devices reach 60,000 rpm and higher rotational speeds are associated with decreasing torque.

Therefore, the following rotational speeds were chosen to perform screening tests: 10,000, 25,000 and 40,000 rpm. Even though 10,000 rpm is out of bounds, in a preliminary test it will be used to dig for any improvements in association with the selected feed rates.

The selected feed rates were 1, 10 and 20 mm/min. The lower feed rate, 1 mm/min, was chosen as an intermediary solution between the current MTRES and the higher feed rates, which are two order of magnitudes

greater than those reached currently by the equipment.

4.5 CUTTING TOOL SELECTION

A major concern in the tool selection is the tool geometry, since geometrical characteristics impact directly on machining performance: chip flow, breakage and direction; cutting force components direction and magnitude; machining productivity; tool life; sliding velocity at the tool-chip interface; thermal energy and cutting edge temperature distributions; machining quality (surface integrity and machining induced residual stress), and so forth [61, 62].

There are two types of cutting tools allowed by ASTM E837 – 13a: carbide inverted-cone dental burrs or small carbide end mills, aiming to produce a hole with cylindrical shape and flat bottom [3]. Since inverted-cone dental burrs are designed to machine teeth, their performance may be far from optimal during metal cutting.

Another feature that could be improved is to use a coated cutting tool. Coatings are used in the machining industry is to improve the tribological condition at the cutting tool-chip and the cutting tool-workpiece interfaces [25]. Choosing the right coating helps to minimize adhesion and friction effects, and the thermal load in the tool is reduced by the small heat penetration [63]. The use of coatings broadened the dry machining operations range, enabled the use of higher rotational speeds and feed rates, enhanced performance in high temperature environments such as abrasive and difficult to machine materials [63, 64]. A comparison between coatings used in cutting tools are provided in Table 4.2. Recapitulating that dry machining is a requirement imposed by ESPI technique and high rotational speeds are demanded by ASTM E837 – 13a [3], choosing TiAlN that presents high oxidation temperatures seems a reasonable decision.

Taking into account the previous considerations, square end mills with a 1.5 mm diameter were chosen. Two tools were selected: two-flute and four-flute tungsten carbide square end mills, coated with TiAlN, which

are shown in Figure 4.2.

Table 4.2 – Coating performances comparison [23].

	TiN	TiCN	TiC	TiAlN	CrN	Al_2O_3
Production process	PVD/CVD	PVD/CVD	CVD	PVD	PVD	CVD/PVD
Coating thickness/µm	1 to 5	1 to 5	1 to 5	1 to 5	1 to 10	1 to 5
Microhardness/HV 0,05	2300	3000	3100	3000	1900	2100 HV 0.1
Oxidation temperature/°C	> 450	> 350	> 350	> 700	> 600	–[3)]
Thermal barrier effect	+++	++	+	++++	+	+++++
Resistance to abrasion	++	+++	+++	+++	++	++
Resistance to wear due to adhesion (against steel)	++	++	+	++	++	+++
Resistance to wear due to diffusion (to steel)	++	+	+	+++	++	+++
Protection of basis material against corrosion	+	+	+	+	++	+

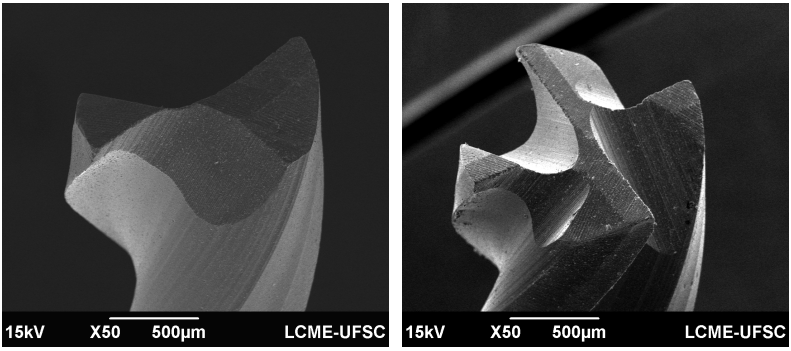

(a) Two-flute square end mill. (b) Four-flute square end mill.

Figure 4.2 – Cutting tools used to perform drilling tests.

Tool geometries were characterized using an optical 3D micro coordinate system Alicona Infinite Focus G5 at *Centro de Tecnologia e Inovação em Fabricação*/UNIFEBE. Both tool present a short cutting edge and a long

cutting edge; on each cutting edge, geometric parameters tool nose radius ρ, clearance angle α, wedge angle β and rake angle γ were measured in 50 parallel sections to the cutting speed vectors; measurement samples are illustrated in Annex A. These results are presented in Table 4.3 and 4.4 with a 95% confidence interval.

Table 4.3 – Two-flute square end mill geometric parameters.

	ρ [μm]	α [°]	β[°]	γ[°]
Short cutting edge	12.8 ± 2.7	0.7 ± 1.0	79.6 ± 1.0	9.7 ± 0.1
Long cutting edge	17.7 ± 3.9	0.0 ± 0.5	80.3 ± 0.6	9.7 ± 0.4

Table 4.4 – Four-flute square end mill geometric parameters.

	ρ [μm]	α [°]	β[°]	γ[°]
Short cutting edge	15.3 ± 3.0	-1.9 ± 3.3	82.6 ± 3.5	9.3 ± 0.2
Long cutting edge	9.3 ± 1.4	-0.4 ± 0.4	81.0 ± 0.5	9.4 ± 0.2

4.6 DRILLING EXPERIMENTAL SETUP AND PROCEDURE

Hole drilling experiments were carried out at the SENAI Institute for Innovation in Manufacturing Systems facilities on a 5-axis machining center Hermle C42U (Figure 4.3). The spindle motor maximum rotational speed is 18,000 rpm and the maximum feed rate is 60 m/min. Since the minimum rotational speed allowed by the current standardised method surpasses the machine tool maximum rotational speed, a Minitor SFIDA MZ01 electrospindle that reaches 60,000 rpm was coupled to the system, accompanied by the control pack Minitor SFIDA MT01CP.

Figure 4.3 – Machine tool overview.

4.6.1 First stage

During the first stage, dry drilling was performed without measuring residual stresses and MTRES was not used. Nonetheless, drilling operations were divided in ten increments, simulating the procedure to be used at the second stage. Naturally, AISI 304L stainless steel was the chosen material to perform screening tests due to the challenges its mechanical and thermal properties pose to machining, using the worst case scenario to verify the coupling between machine tool dynamics and cutting tool when drilling

the chosen cutting parameters. Another feature that was being tested is whether the end mills would be capable of drilling multiple holes without being severely worn to a prohibitive level culminating in tool breakage as observed in the dental end mills currently used by MTRES [42].

Workpieces were fastened directly on the machining centre table using strap clamps. Two new cutting tools were used, a four-flute square end mill and a two-flute square end mill. Each cutting tool was used to test all cutting parameters combinations shown in Table 4.5.

Table 4.5 – Tested cutting parameters during first stage.

Cutting parameters		
10,000 rpm 1 mm/min	10,000 rpm 10 mm/min	10,000 rpm 20 mm/min
25,000 rpm 1 mm/min	25,000 rpm 10 mm/min	25,000 rpm 20 mm/min
40,000 rpm 1 mm/min	40,000 rpm 10 mm/min	40,000 rpm 20 mm/min

Each cutting tool was used to perform a single repetition for each cutting parameters combination, totalising nine drilling operations for each end mill. Holes were drilled in a row according to the longitudinal workpiece direction, with a 10 mm distance between hole centres to prevent any influences from the previous and next drilling sites. This experiment workflow is given by 4.4.

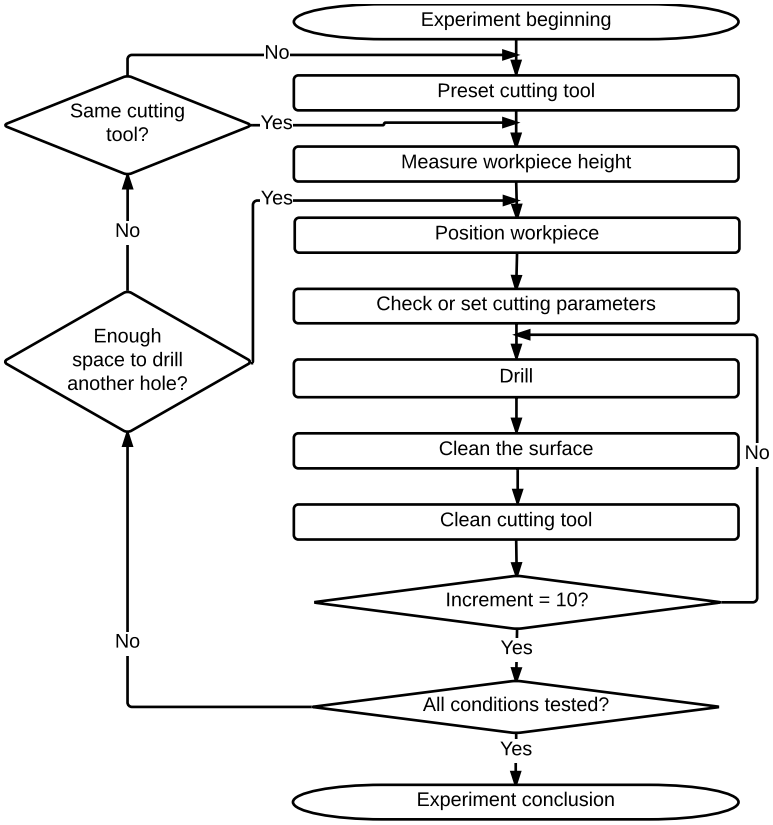

Figure 4.4 – First stage flowchart.

4.6.2 Second stage

The experiment second stage consisted of machining induced residual stress measurements using the Hole-Drilling Method with ESPI in three kinds of workpieces as already described. To measure stresses, MTRES was employed. This device is composed by two independent subsystems: the drilling module and the measurement module. The drilling module was disassembled from the equipment, freeing the diameter socket in which this subsystem is fixed (dimensions in Annex C). This way, the set composed by cutting tool and electrospindle shank MZ01 – SK40 was able to dive into

the socket and drill the hole without colliding against the device, since a clearance annulus having a 6 mm maximum distance between those parts was possible given the electrospindle characteristics as specified in Annex B. A schematic MTRES in-scale view and electrospindle positions during measuring and drilling is provided in Figure 4.5.

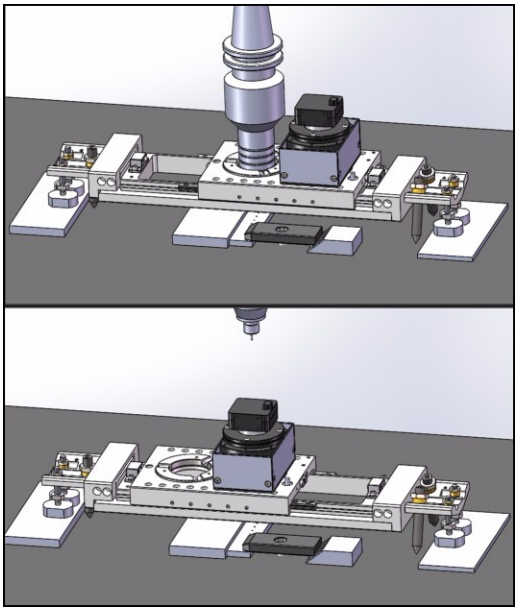

Figure 4.5 – Drilling and measuring positions.

After positioning MTRES on the machine tool table and adjusting a proper height, i.e. aligning the interferometer arms to have the same length, a probe coordinate measurement was conducted to reference the socket cylindrical surface. This referencing procedure was also performed on the workpieces upper surface to find a plane that describes their heights to drill the first step correct depth.

Workpieces were fixed as in the previous stage using strap clamps, which were bolted as far as possible from the drilling points with the minimum required torque to keep the specimen in place without introducing undesired stresses into it. The workpiece lateral surface was propped against

a flat metal strip along which the specimen could slide forward to the next drilling position, which preserved the same 10 mm spacing as the one used in the previous stage. The metal strip was aligned perpendicularly to MTRES linear guides using a set-square, yielding the disposition shown in Figure 4.6.

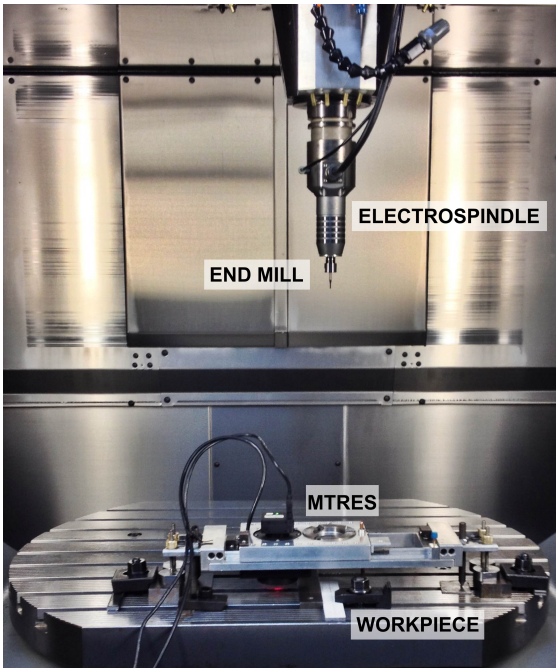

Figure 4.6 – Drilling experiments key elements mounted on the machine tool table.

Each end mill was assigned to only one material and all the cutting parameters according to the sequence shown in Table 4.6 were tested using a single tool for all repetitions; test short nomenclatures are provided since they were used to make clean plots in the next chapter. This sequence was chosen based on the conventional machining knowledge that lower feed rates are less aggressive than higher ones, since the most favourable chips chosen in the previous stage seemed to be satisfactorily formed at least for AISI 304L. However, clear distinction between chip formation regime due to size effect was not easily discerned since there was evidence of a transition

between these two regimes during the preliminary tests.

Since the tool edge radius (9.3<ρ<17.7 μm) was much greater than the feed per tooth (0.06<f_z<0.40 μm), during the planned tests the cutting edge would not experience the transition from sharp to blunt condition, otherwise it would modify significantly the metal cutting regime. Furthermore, drilling several holes with a single end mill and verifying that the machining induced residual stresses were kept at satisfactory levels also represent an improvement from the current MTRES state, as each dental end mill is discarded after drilling only a single hole [7]. Three repetitions were planned for all materials in each cutting parameters combination, but due to tool breakage in the beginning of the final tests during AISI 304L drilling only two repetitions were made for this material. Three repetitions could be made during AISI 1020 and AA 6061 machining without replacing the cutting tool.

Table 4.6 – Tested cutting parameters during second stage.

Cutting parameters combination	**Short nomenclature**	**Feed per tooth**
25,000 rpm 10 mm/min	a: two-flute end mill A: four-flute end mill	$f_{z,a}$: 0.20 μm $f_{z,A}$: 0.10 μm
40,000 rpm 10 mm/min	b: two-flute end mill B: four-flute end mill	$f_{z,b}$: 0.13 μm $f_{z,B}$: 0.06 μm
25,000 rpm 20 mm/min	c: two-flute end mill C: four-flute end mill	$f_{z,c}$: 0.40 μm $f_{z,C}$: 0.20 μm
40,000 rpm 20 mm/min	d: two-flute end mill D: four-flute end mill	$f_{z,d}$: 0.25 μm $f_{z,D}$: 0.13 μm

Another care taken during the experiments concerned the reference surface cleaning: dessicated compressed air was blown remove metal chips from the measuring area without contact after each drilling step prior to the image acquisition. Cutting edges were similarly cleaned after each increment. Figure 4.7 provides the step-by-step procedure followed during the experiment.

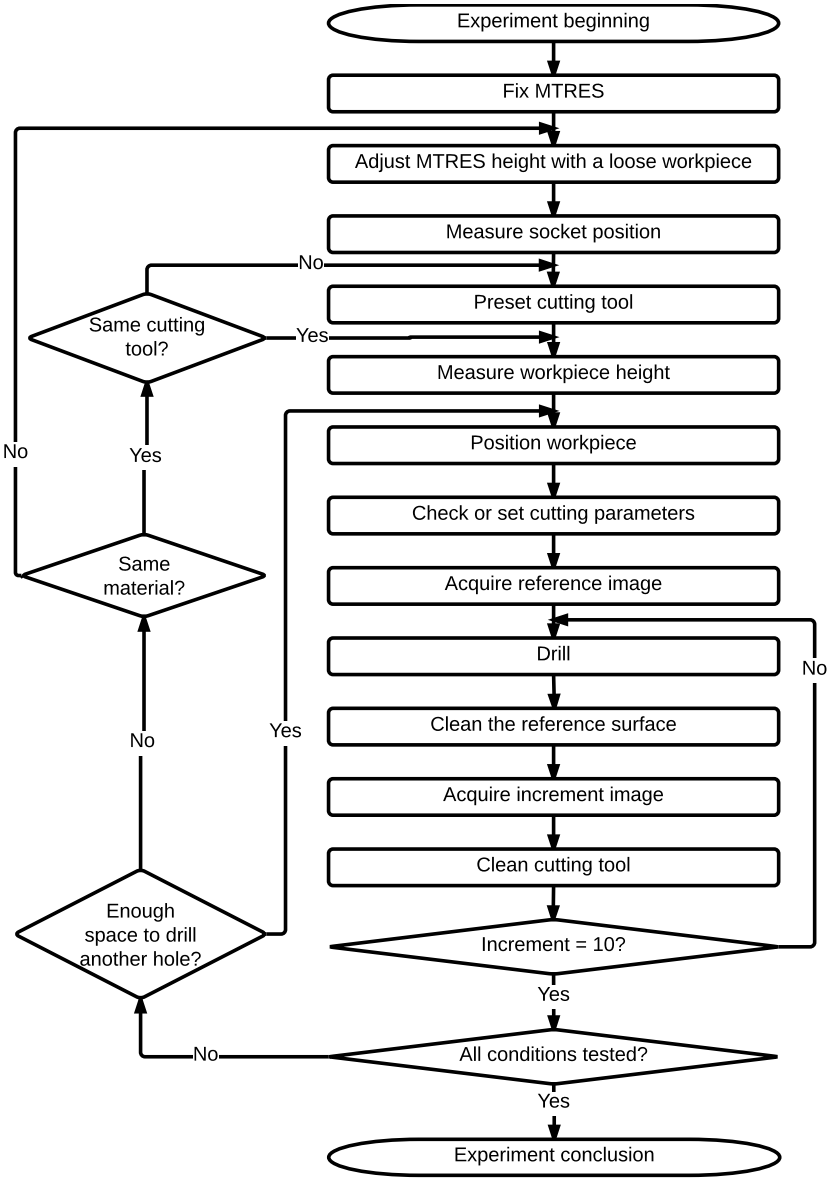

Figure 4.7 – Second stage flowchart.

4.7 TECHNIQUES AND ANALYSES

The forthcoming topics consist of information about the techniques employed and the analyses that were derived from them during the development of this work; the relationships between the experiments inputs and outputs, techniques and their respective analyses are synthesized in Figure 4.8.

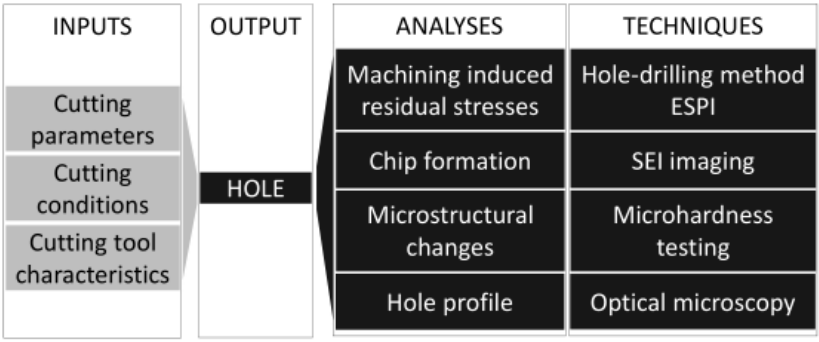

Figure 4.8 – Overview of analyses and techniques used in this work.

4.7.1 Analysis from the Hole-Drilling Method

In this work, uniform residual stresses evaluation were performed using the Hole-Drilling Method as aforementioned. For this purpose, MTRES measurement module, which is a double-illumination ESPI system to measure pure radial in-plane displacement fields that makes use of an axis-symmetrical binary diffractive optical element (DOE) as a beam-splitting grating (Figure 4.9). Further information about this system can be found in [6, 65].

The assumption of an uniform stress field is based on the fact that the workpieces have undergone a heat treatment to relieve prior manufacturing residual stresses before the hole drilling experiments. In addition, uniform stress calculation can be done to find the representative size of a residual stress field, being an average within the hole depth, weighted in favour of the stresses that act near the measured surface [3]. Therefore, the

uniform stress assumption to assess the drilling process overall effect on the machining induced residual stress seems to be a reasonable approach. For this reason, results are expressed in terms of the principal stresses σ_1 and σ_2. To assess the cutting parameters effects on machining induced residual stresses, analysis of variance (ANOVA) was conducted.

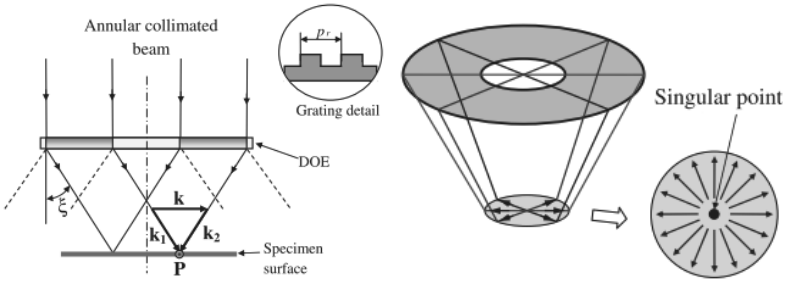

(a) Radial in-plane sensitivity and DOE cross-section.

(b) Illumination principle

Figure 4.9 – Illumination details of the employed setup [6].

4.7.2 Analysis from microhardness testing

Microhardness testing was performed to analyse the drilling effect on the hole surroundings microstructure. Metallographic specimen preparation was carried out prior to microhardness testing observing standardised guidelines from ASTM and ASM [66, 67]. The hole cross-section was obtained with a metallographic cut-off machine which uses wet abrasive cutting to impinge less damage than other sectioning techniques; afterwards, specimens were hot mounted using a phenolic resin at 150°C and 14.7 MPa during 10 minutes. Grinding and polishing steps are found in Table 4.7.

Microhardness measurements were made using a Shimadzu HMV-2 microhardness tester at LABCONF/UFSC – *Laboratório de Conformação Mecânica* following instructions from ISO 6507-1:2005 – Metallic materials – Vickers hardness test – Part 1: Test method [68]. Due to the different materials behaviour, i.e. the extent of indentation influence is greater in softer materials such as aluminium, two microhardness measurement schemes were used. The hole wall dimensions allowed four hole wall indentations

and three hole bottom indentations in aluminium alloy (Figure 4.11), while six hole wall indentations and five hole bottom indentations could be made in both steels (Figure 4.10). Microhardness test loads and their application times are provided in Table 4.8. In order to verify microhardness changes around the hole, hole bottom and hole wall values were tested against the base material values using a paired Welch t-test for unequal variances.

Table 4.7 – Grinding and polishing steps.

AISI 1020	**Grinding**	120, 220, 360, 600, 1200 grits SiC paper
	Polishing	3 μm diamond paste, 0.3 μm alumina
AISI 304L	**Grinding**	120, 220, 360, 600, 1200 grits SiC paper
	Polishing	3 μm diamond paste, 0.3 μm alumina
AA 6061	**Grinding**	220, 360, 600, 1200 grits SiC paper
	Polishing	3 μm diamond paste, 1 μm diamond paste

Table 4.8 – Microhardness testing parameters.

Material	Test load	Force application time
AISI 1020	1 kgf (9.8 N)	10s
AISI 304L	1 kgf (9.8 N)	10s
AA 6061	0.2 kgf (1.96 N)	5s

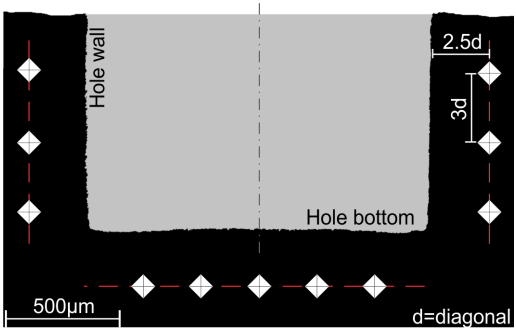

Figure 4.10 – Indentation scheme in steel samples.

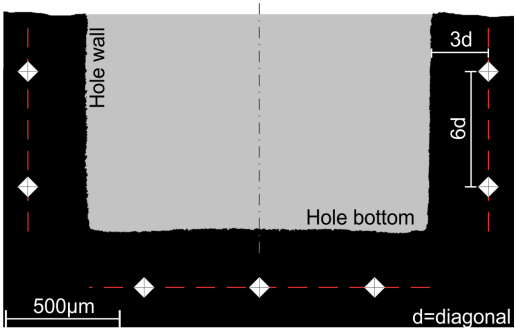

Figure 4.11 – Indentation scheme in aluminium alloy sample.

4.7.3 Analysis from scanning electron and optical microscopy

When a sample is exposed to an electron beam, various signals are produced from the interactions between the atoms in the sample and the incident electrons: this is scanning electron microscopy (SEM) basic principle. Some examples of signals are secondary electrons, backscattered electrons, characteristic X-rays, Auger electrons, and so forth; depending on the signal nature, different types of information about the sample can be obtained.

In this work, chips and burrs were visualised through secondary electron imaging (SEI), since secondary electrons are low-energy electrons generated near the surface and for this reason images produced from this kind of signal provide information about the surface topography [69]. For this purpose, a JEOL JSM-6390LV scanning electron microscope was used at LCME/UFSC – *Laboratório Central de Microscopia Eletrônica*.

To look into the hole profile produced by the selected square end mill and provide a comparison with the current drilling process, hole cross-section micrographs were acquired with a LEICA DM 4000 M optical microscope at LCM/UFSC – *Laboratório de Caracterização Microestrutural*. The hole cross-section images were obtained in specimens properly prepared and prior to microhardness measurements.

5 RESULTS AND DISCUSSION

Results are grouped by workpiece material in order to provide whole comprehension of the findings. For each material, the following topics are investigated: chip formation, machining induced residual stress and microhardness changes. As AISI 304L austenitic stainless steel was the only material used in both stages, its section presents also a brief additional discussion about the formed burr. The chapter is closed with a comparison between hole geometries obtained with the square end mills and the dental inverted-cone end mill currently employed by MTRES.

5.1 STAINLESS STEEL AISI 304L

5.1.1 Burr and chip formation

The first attribute to be analysed during the first stage was the burr formation, to verify whether its size may pose a problem to the optical technique. Figure 5.1 shows *Polar* software interface, used to process data and calculate stresses, in which three areas can be discerned: the circle inside red circumference is the hole, the annulus between the red circumference and the blue inner circumference corresponds to the discarded area, while the annulus between the blue inner and outer circumferences is the useful area that actually provide information about strains and has its boundaries defined by ASTM E837 – 13a [3] for type A strain gage.

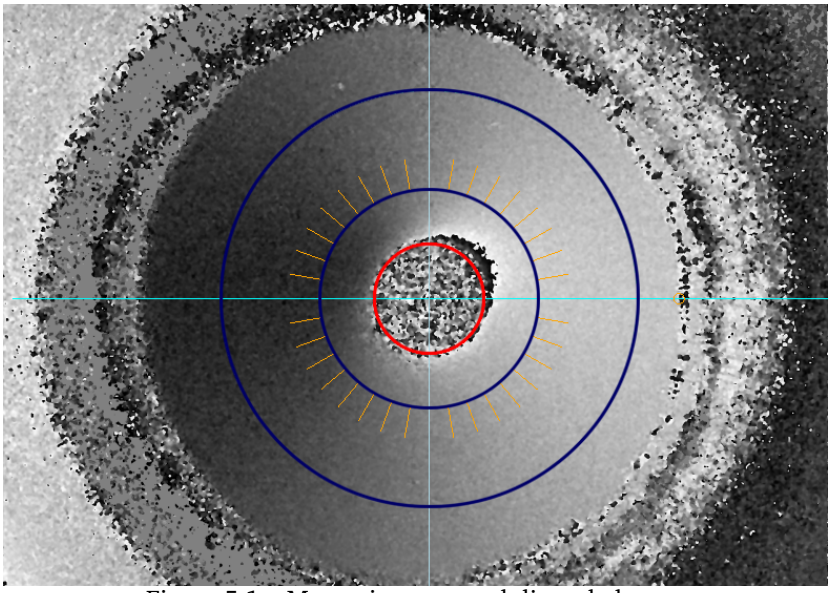

Figure 5.1 – Measuring area and discarded area.

Burr formation was negligible for the optical technique utilisation, since it was always restrained to a very thin area around the hole border, having an extension of approximately 1 μm, as observed in Figure 5.2 and 5.3. Since the measuring inner boundary has about 2.20 mm and the drilled holes have around 1.55 mm, burr formation does not seem to be a concern to the optical measurement technique and for this reason this analysis were not performed in the second stage for all workpiece materials. A similar trend was already reported by Blödorn [7] for AA 6061, AISI 304L and AISI 1020, in which burrs were very small and do not interfere in the optical measurement.

(a) $v_f = 1$ mm/min and $n = 10,000$ rpm (b) $v_f = 10$ mm/min and $n = 10,000$ rpm (c) $v_f = 20$ mm/min and $n = 10,000$ rpm

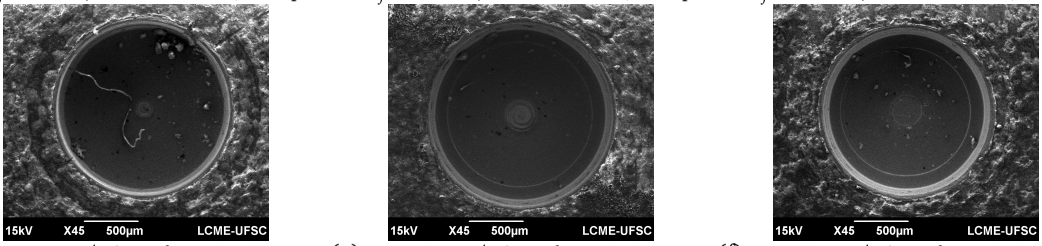

(d) $v_f = 1$ mm/min and $n = 25,000$ rpm (e) $v_f = 10$ mm/min and $n = 25,000$ rpm (f) $v_f = 20$ mm/min and $n = 25,000$ rpm

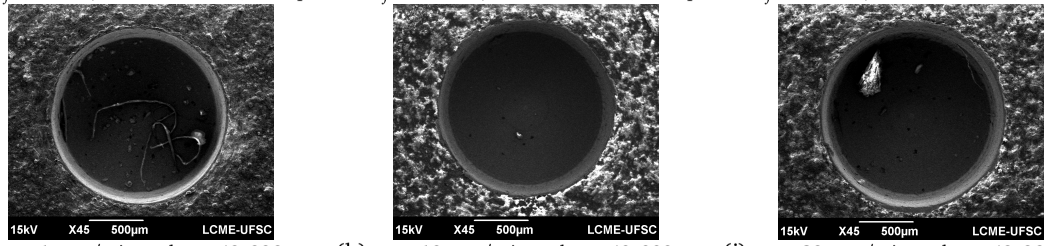

(g) $v_f = 1$ mm/min and $n = 40,000$ rpm (h) $v_f = 10$ mm/min and $n = 40,000$ rpm (i) $v_f = 20$ mm/min and $n = 40,000$ rpm

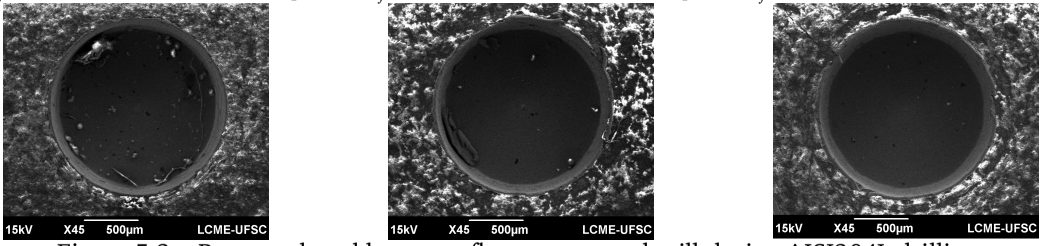

Figure 5.2 – Burr produced by a two-flute square end mill during AISI304L drilling.

(a) $v_f = 1$ mm/min and $n = 10,000$ rpm (b) $v_f = 10$ mm/min and $n = 10,000$ rpm (c) $v_f = 20$ mm/min and $n = 10,000$ rpm

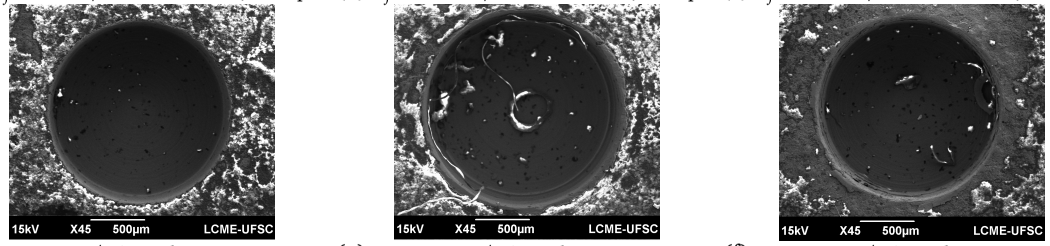

(d) $v_f = 1$ mm/min and $n = 25,000$ rpm (e) $v_f = 10$ mm/min and $n = 25,000$ rpm (f) $v_f = 20$ mm/min and $n = 25,000$ rpm

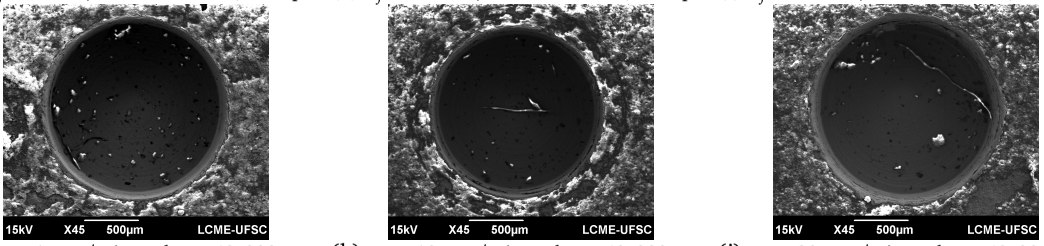

(g) $v_f = 1$ mm/min and $n = 40,000$ rpm (h) $v_f = 10$ mm/min and $n = 40,000$ rpm (i) $v_f = 20$ mm/min and $n = 40,000$ rpm

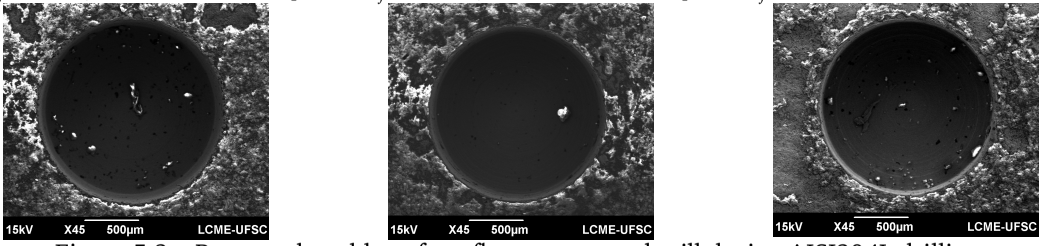

Figure 5.3 – Burr produced by a four-flute square end mill during AISI304L drilling.

Austenitic stainless steels present high plastic deformability due to their face-centred cubic crystal lattice, which results in several slip systems. This feature favours not only the built-up edge and gluing-points formation, but it also contributes to the production of undesired ribbon and snarled chips [23].

An overview comparison of the formed chips during AISI 304L drilling using a two-flute end mill is provided in Figure 5.4. In fact, using a two-flute end mill, snarled chips were formed using the lowest rotational speed (10,000 rpm) for all feed rates. These snarled chips proved to be a very prejudicial feature, as seen in Figure 5.2, where radial scratches can be seen to the corresponding cutting parameters combinations. This can be better understood seeing Figure 5.5, in which radial scratches caused by continuous chips invaded the measuring area and provoked loss of correlation where the strains are intenser, near the measuring perimeter inner boundary.

Using the lowest feed rate (1 mm/min), the most similar condition to the one used currently by MTRES drilling module, unfavourable chip formation was detected for all the rotational speeds: a very thin snarled chip was formed, indicating that the minimum chip thickness was barely surpassed. In addition, a powdery and irregular aspect was seen for higher rotational speeds, similar to those chips reported by Blödorn [7]. Using 10 and 20 mm/min feed rates, two chip widths can be observed due to the two asymmetrical cutting edges: the minor produced around 80 μm wide chips, while the major cut approximately 450 μm wide chips. Particularly using higher rotational speeds (25,000 and 40,000 rpm) associated to higher feed rates (10 and 20 mm/min), chips seemed to be properly formed without favouring continuous morphology due to smaller thickness that facilitated chip breakage; these are desirable characteristics in the aimed application.

(a) $v_f = 1$ mm/min and $n = 10,000$ rpm (b) $v_f = 10$ mm/min and $n = 10,000$ rpm (c) $v_f = 20$ mm/min and $n = 10,000$ rpm

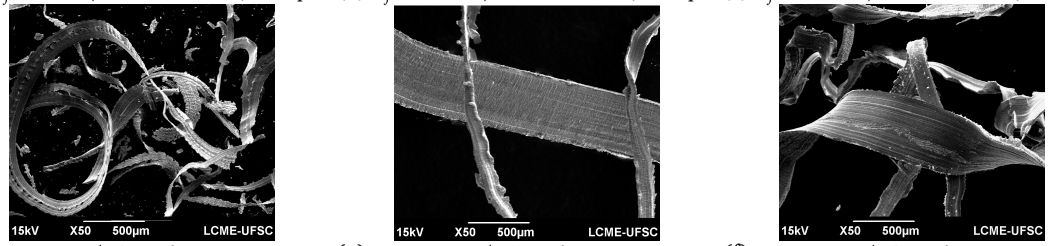

(d) $v_f = 1$ mm/min and $n = 25,000$ rpm (e) $v_f = 10$ mm/min and $n = 25,000$ rpm (f) $v_f = 20$ mm/min and $n = 25,000$ rpm

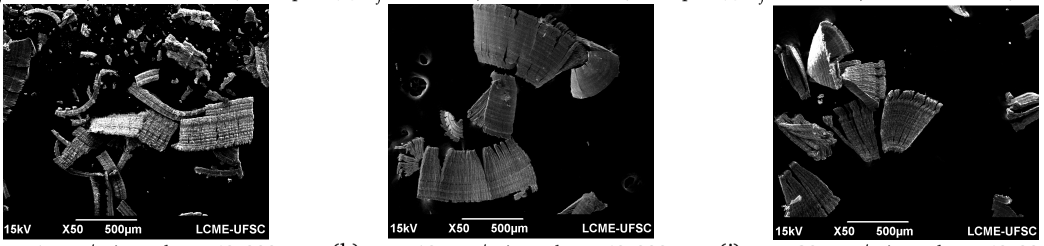

(g) $v_f = 1$ mm/min and $n = 40,000$ rpm (h) $v_f = 10$ mm/min and $n = 40,000$ rpm (i) $v_f = 20$ mm/min and $n = 40,000$ rpm

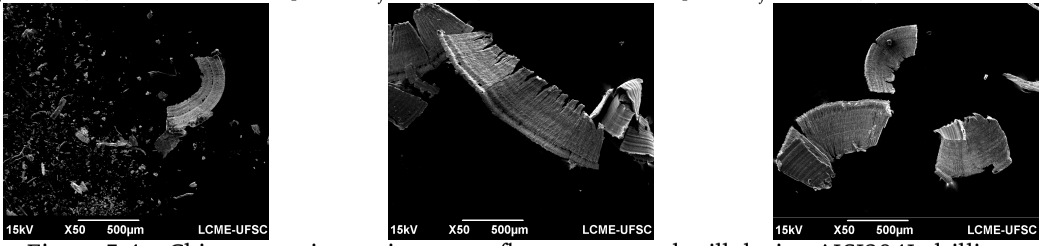

Figure 5.4 – Chip comparison using a two-flute square end mill during AISI304L drilling.

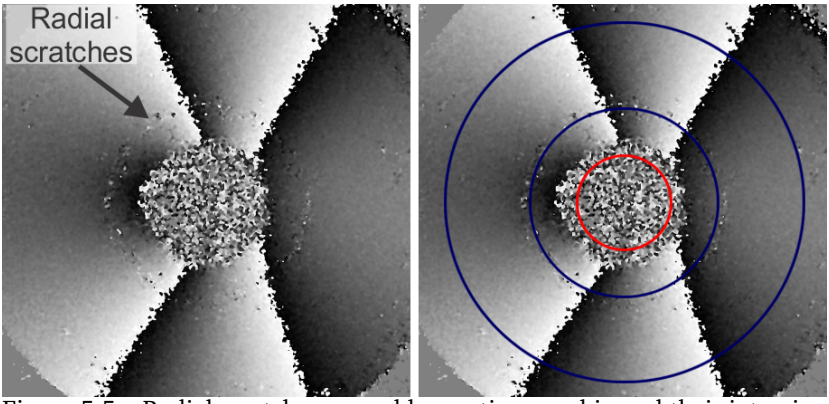

Figure 5.5 – Radial scratches caused by continuous chip and their intrusion in the measuring area.

In higher magnification (Figure 5.6), intense plastic deformation can be seen for all rotational speeds at 1 mm/min. In contrast, for the higher feed rates (10 and 20 mm/min) using all the rotational speeds, a regular chip formation was reached possibly because the feed per tooth was greater than the minimum chip thickness. This transition from favourable to unfavourable chip formation occurs because plastic deformation process changes as the uncut chip thickness and the grain size become comparable; when this condition is reached, grain boundaries, impurities and crystal defects matter. In this regime, shear energy increases as the uncut chip thickness gets thinner [70]. Plus, the patterns observed when using v_f =1 mm/min suggests that the chip load in a single rotation was insufficient, therefore only after several rotations as the feed advances the chip load was enough to form a chip; meanwhile, the material suffered rubbing and work hardening as the end mill rotates without metal cutting [71].

(a) $v_f = 1$ mm/min and $n = 10,000$ rpm (b) $v_f = 10$ mm/min and $n = 10,000$ rpm (c) $v_f = 20$ mm/min and $n = 10,000$ rpm

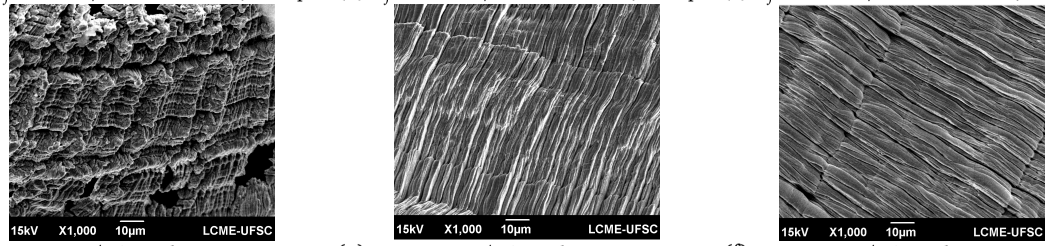

(d) $v_f = 1$ mm/min and $n = 25,000$ rpm (e) $v_f = 10$ mm/min and $n = 25,000$ rpm (f) $v_f = 20$ mm/min and $n = 25,000$ rpm

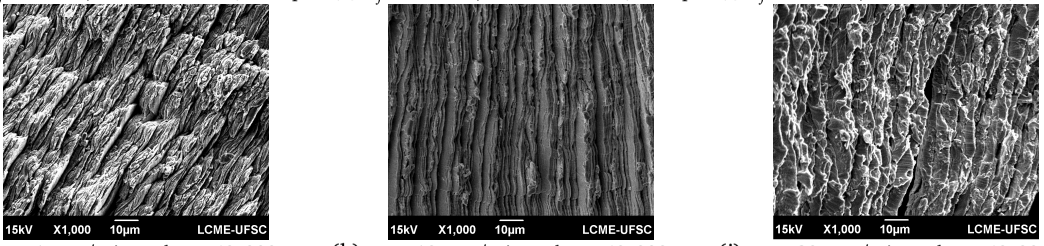

(g) $v_f = 1$ mm/min and $n = 40,000$ rpm (h) $v_f = 10$ mm/min and $n = 40,000$ rpm (i) $v_f = 20$ mm/min and $n = 40,000$ rpm

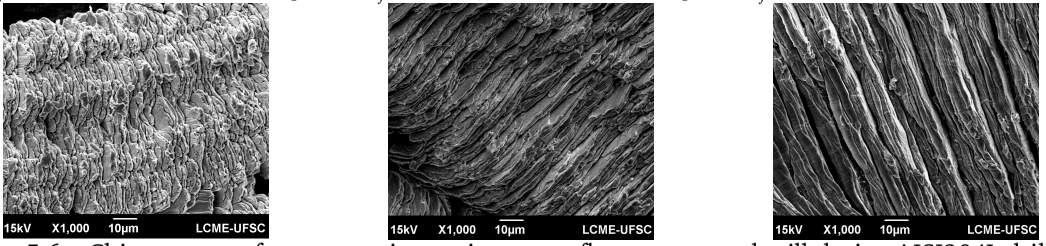

Figure 5.6 – Chip upper surface comparison using a two-flute square end mill during AISI304L drilling.

On the other hand, long and snarled chips were barely observed using a four-flute end mill, as the higher flute number favoured chip breakage, and all conditions seem to provide a more favourable chip size, mostly having a width about 250 μm, as seen in Figure 5.7. Nonetheless, fluctuations in the drilling process may happen and long, continuous chip may also be formed, as radial marks in Figure 5.3e indicates. Concerning the lowest feed rate (1 mm/min), a similar tendency as the two-flute end mill towards poor chip formation was observed for all rotational speeds, thin chips with a fragile appearance were seen instead of the powdery aspect observed for the two-flute end mill, worsening as the feed per tooth decreases with increasing rotational speed. Looking at the chip upper surface in Figure 5.8 using the lowest feed rate, the same poor cutting process dominated by intense plastic deformation observed with a two-flute end mill is seen. However, examining the chip upper surface for all the other cutting parameters combinations, regular material layers arise and may indicate that the minimum chip thickness is close to the feed per tooth.

Considering the chip size and form discussion for both cutting tools, the highest feed rates (10 and 20 mm/min) and highest rotational speeds (25,000 rpm and 40,000 rpm) were chosen, since they provided smaller chip sizes without excessive plastic deformation.

(a) $v_f = 1$ mm/min and $n = 10,000$ rpm (b) $v_f = 10$ mm/min and $n = 10,000$ rpm (c) $v_f = 20$ mm/min and $n = 10,000$ rpm

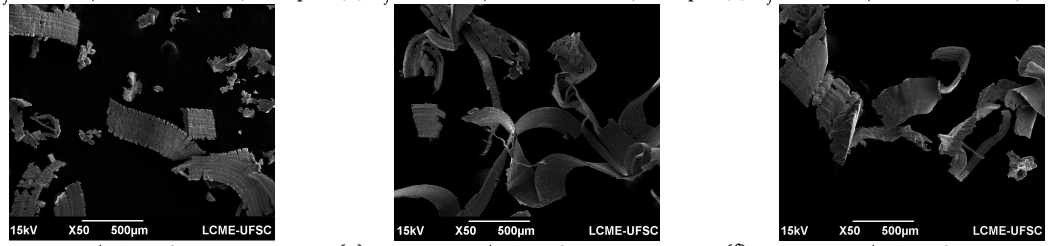

(d) $v_f = 1$ mm/min and $n = 25,000$ rpm (e) $v_f = 10$ mm/min and $n = 25,000$ rpm (f) $v_f = 20$ mm/min and $n = 25,000$ rpm

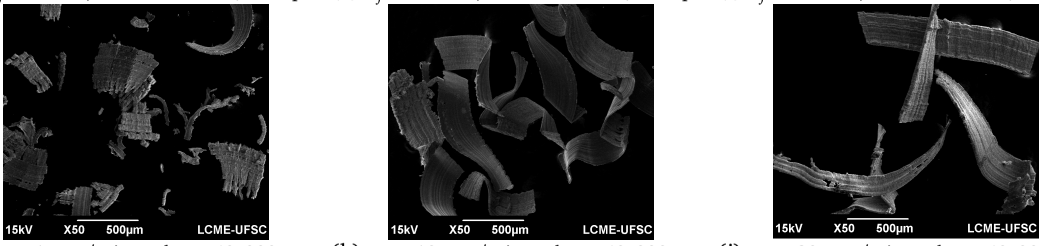

(g) $v_f = 1$ mm/min and $n = 40,000$ rpm (h) $v_f = 10$ mm/min and $n = 40,000$ rpm (i) $v_f = 20$ mm/min and $n = 40,000$ rpm

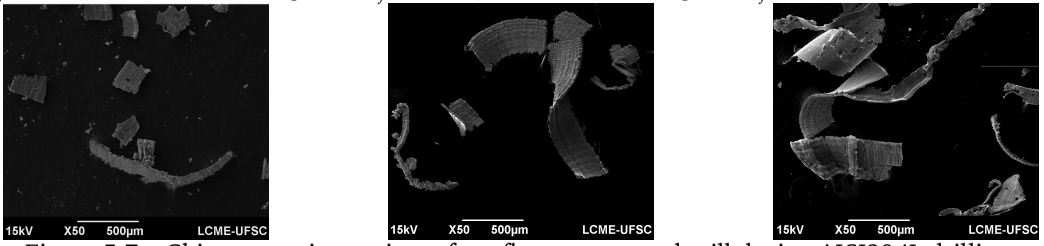

Figure 5.7 – Chip comparison using a four-flute square end mill during AISI304L drilling.

(a) $v_f = 1$ mm/min and $n = 10,000$ rpm (b) $v_f = 10$ mm/min and $n = 10,000$ rpm (c) $v_f = 20$ mm/min and $n = 10,000$ rpm

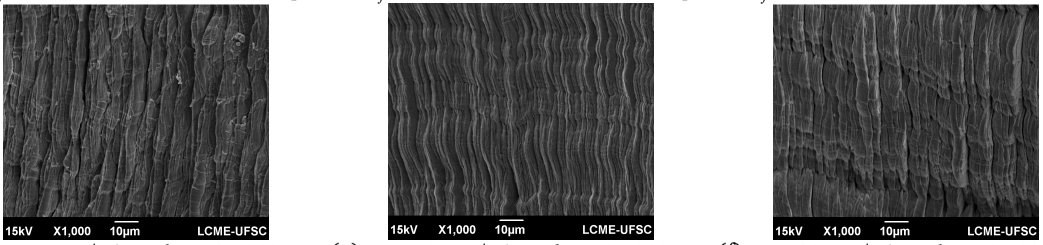

(d) $v_f = 1$ mm/min and $n = 25,000$ rpm (e) $v_f = 10$ mm/min and $n = 25,000$ rpm (f) $v_f = 20$ mm/min and $n = 25,000$ rpm

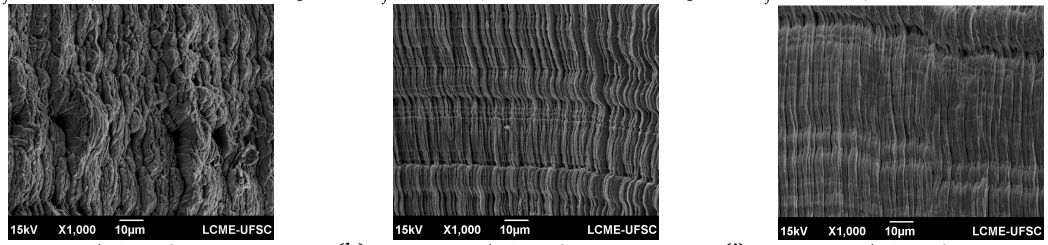

(g) $v_f = 1$ mm/min and $n = 40,000$ rpm (h) $v_f = 10$ mm/min and $n = 40,000$ rpm (i) $v_f = 20$ mm/min and $n = 40,000$ rpm

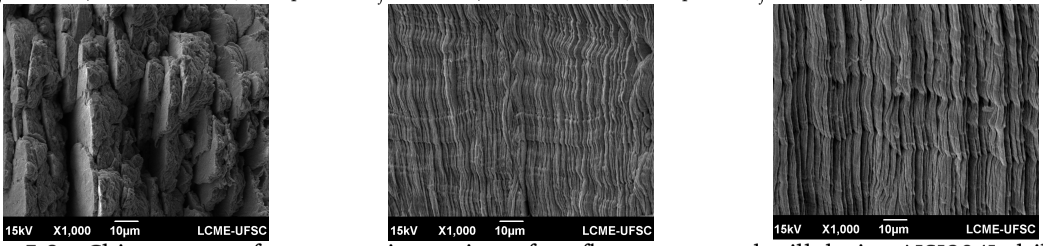

Figure 5.8 – Chip upper surface comparison using a four-flute square end mill during AISI304L drilling.

5.1.2 Machining induced residual stress

During the first residual stresses measurements, two catastrophic tool breakages took place while attempting to drill the first holes. For this reason, it was established that only two repetitions would be made for each cutting parameter combination during AISI 304L drilling. Snarled chips were also formed by chance, despite eliminating the most favourable cutting parameters for their inception, since the material nature is prone to their production. For this reason, some points that delivered unreliable data were eliminated and only a single point for those cutting parameters combinations (b and B) was available to conduct this analysis and therefore MTRES maximum error was used for these tests instead of sample standard deviation. Collected data can be found in Table B.1 – Appendix B.

In Figures 5.9 and 5.10, maximum and minimum machining induced residual stresses mean values are plotted for each cutting parameter combination for both end mills types, accompanied by their sample standard deviation whenever applicable; their values can be found in Tables 5.1 and 5.2. The sample standard deviation was plotted instead of the confidence interval in order to focus on the data dispersion. Since the flute number evidently exerts an influence on residual stress introduction, ANOVA was applied separately to assess the rotational speed and feed rate effects for each cutting tool.

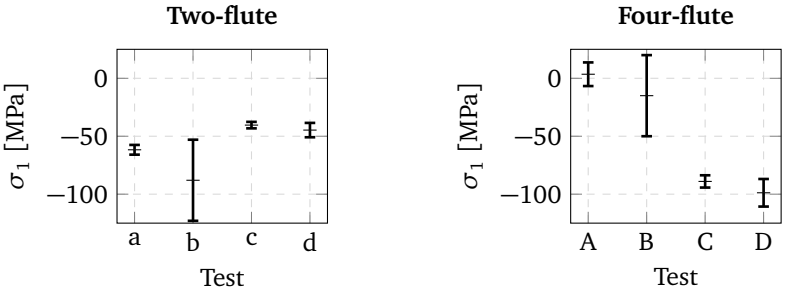

Figure 5.9 – Machining induced maximum residual stress σ_1 during AISI 304L drilling.

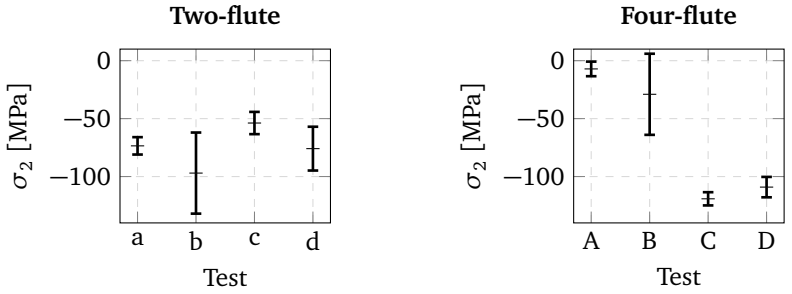

Figure 5.10 – Machining induced minimum residual stress σ_2 during AISI 304L drilling.

Table 5.1 – Machining induced residual stresses in AISI 304L drilling using a two-flute end mill.

Cutting parameters	σ_1 **[MPa]**	σ_2 **[MPa]**
25,000 rpm 10 mm/min	-62 ±4	-74 ±8
40,000 rpm 10 mm/min	-88 ±35*	-97 ±35*
25,000 rpm 20 mm/min	-40 ±3	-54 ±10
40,000 rpm 20 mm/min	-45 ±6	-76 ±19

*MTRES maximum error (Celso L. N. Veiga, personal communication, October 22, 2015).

Table 5.2 – Machining induced residual stresses in AISI 304L drilling using a four-flute end mill.

Cutting parameters	σ_1 **[MPa]**	σ_2 **[MPa]**
25,000 rpm 10 mm/min	4 ±10	-7 ±6
40,000 rpm 10 mm/min	-15 ±35*	-29 ±35*
25,000 rpm 20 mm/min	-89 ±5	-119 ±6
40,000 rpm 20 mm/min	-99 ±12	-109 ±9

*MTRES maximum error (Celso L. N. Veiga, personal communication, October 22, 2015).

Compressive stresses with higher magnitudes have been introduced into the workpiece for almost all cutting parameters combinations, indicating that intense plastic deformation occurred in the hole walls, possibly associated with ploughing action that occurs with a protusion of the primary deformation zone below the tool nose given by material adhesion [50]. In addition, when uncut chip thickness drops below two times the tool edge radius, cutting efficiency decays dramatically and chip is barely formed at the cost of increased temperature, residual stresses and forces [72]. In this case, this effect was very aggressive since the feed per tooth and tool edge radius ratio was between 0.41% and 3.1%.

Feed rate seems to be the most important cutting parameter using a four-flute end mill. The lowest machining residual stresses occurred when drilling with a four-flute end mill using lower feed rate (10 mm/min) for both rotational speeds. A possible explanation for this behaviour is an equilibrium between thermal and mechanical contributions, since lower feed rates mean higher interaction times between a rotating cutting tool and the workpiece. Mechanical effects that tend to compressive stresses are counterbalanced with higher heat generation which favours tensile stress.

In Figure 5.11, interaction plots show feed rate and rotational speed effects on the maximum residual stress σ_1 using a two-flute cutting tool, while its ANOVA is presented in Table 5.3. Feed rate presented the strongest source of variation, while non significant interaction and rotational speed effects were noticed. Using v_f= 20 mm/min and n= 25,000 rpm, absolute residual stress values were less pronounced than using v_f= 10 mm/min and n= 40,000 rpm.

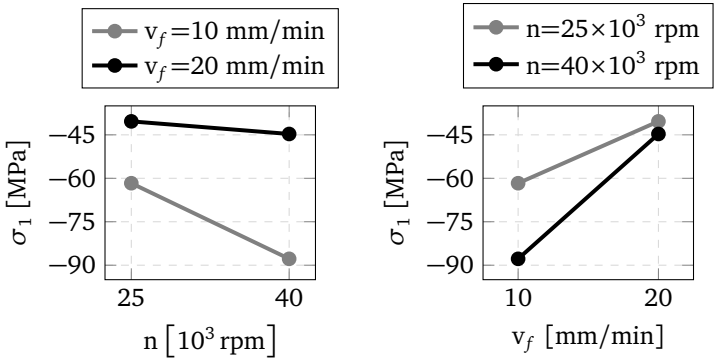

Figure 5.11 – Interaction plots for maximum residual stress σ_1 using a two-flute square end mill during AISI 304L drilling.

Table 5.3 – ANOVA table for maximum residual stress σ_1 using a two-flute square end mill during AISI 304L drilling.

Source of Variation	*SS*	*df*	*MS*	*F-ratio*	*P-value*	F_{crit}
Feed rate	1661.52	1	1661.52	38.82	0.0083	10.13
Rotational speed	370.88	1	370.88	8.67	0.0603	10.13
Interaction	189.23	1	189.23	4.42	0.1263	10.13
Within	128.41	3	42.80			
Total	1933.49	6				

$\alpha = 0.05$; SS: sum of squares; df: degrees of freedom; MS: mean squares.

Figure 5.12 shows interaction plots for feed rates and rotational speeds effects on the minimum residual stress σ_2 using a two-flute end mill. In Table 5.4, ANOVA shows that rotational speed, feed rate and the interaction between these two variables do not provoked noticeable varia-

tions. $v_f = 20$ mm/min and $n = 25{,}000$ rpm presented better results, since their absolute residual stress values were smaller than the other cutting parameters in each comparison.

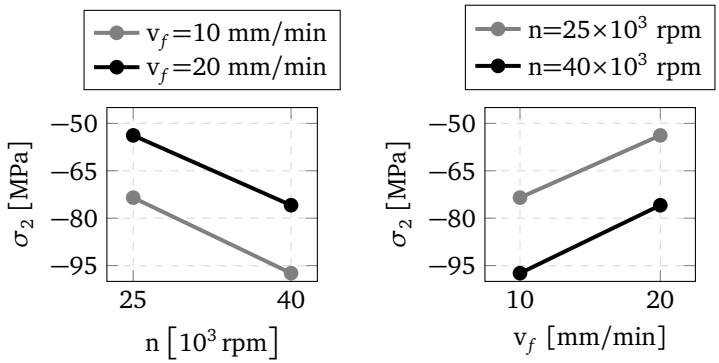

Figure 5.12 – Interaction plots for minimum residual stress σ_2 using a two-flute square end mill during AISI 304L drilling.

Table 5.4 – ANOVA table for minimum residual stress σ_2 using a two-flute square end mill during AISI 304L drilling.

Source of Variation	*SS*	*df*	*MS*	*F-ratio*	*P-value*	F_{crit}
Feed rate	678.98	1	678.98	2.01	0.2509	10.13
Rotational speed	846.40	1	846.40	2.51	0.2112	10.13
Interaction	1.30	1	1.30	0.00	0.9545	10.13
Within	1011.24	3	337.08			
Total	2353.79	6				

$\alpha = 0.05$; SS: sum of squares; df: degrees of freedom; MS: mean squares.

Using a four-flute square end mill, $v_f = 10$ mm/min and $n = 25{,}000$ rpm, less aggressive maximum σ_1 machining induced residual stresses were produced, as seen in Figure 5.13. In Table 5.5, rotational speed and the interaction exert little influence in the residual stress introduction, but the feed rate presents a strong effect: as the feed rate increased, residual stresses became more and more compressive for all rotational speeds.

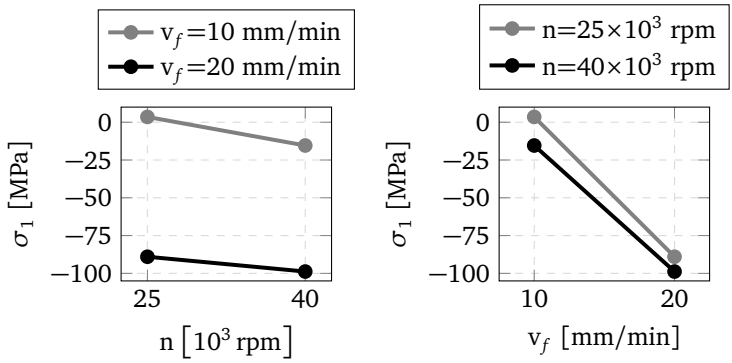

Figure 5.13 – Interaction plots for maximum residual stress σ_1 using a four-flute square end mill during AISI 304L drilling.

Table 5.5 – ANOVA table for maximum residual stress σ_1 using a four-flute square end mill during AISI 304L drilling.

Source of Variation	*SS*	*df*	*MS*	*F-ratio*	*P-value*	F_{crit}
Feed rate	12376.32	1	12376.32	67.82	0.0037	10.13
Rotational speed	329.48	1	329.48	1.81	0.2717	10.13
Interaction	33.12	1	33.12	0.18	0.6988	10.13
Within	547.48	3	182.49			
Total	15108.88	6				

$\alpha = 0.05$; SS: sum of squares; df: degrees of freedom; MS: mean squares.

In Figure 5.14, minimum machining induced residual stresses σ_2 absolute values were much smaller for $v_f = 10$ mm/min; furthermore, the feed rate effect becomes even more clear in Table 5.6, since the P-value is really low at $\alpha = 0.05$. Rotational speed and the interaction did not produce significant changes.

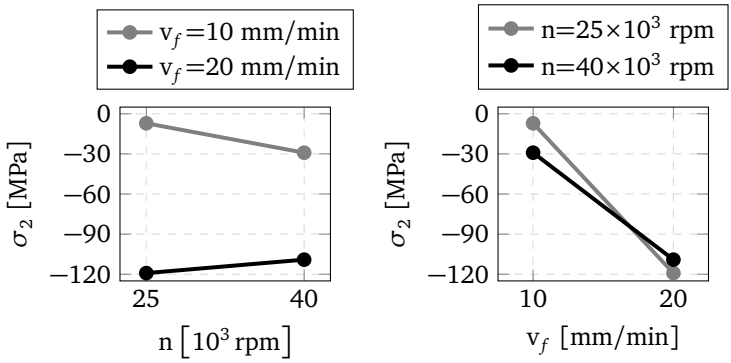

Figure 5.14 – Interaction plots for minimum residual stress σ_2 using a four-flute square end mill during AISI 304L drilling.

Table 5.6 – ANOVA table for minimum residual stress σ_2 using a four-flute square end mill during AISI 304L drilling.

Source of Variation	*SS*	*df*	*MS*	*F-ratio*	*P-value*	F_{crit}
Feed rate	14753.28	1	14753.28	147.34	0.0012	10.13
Rotational speed	57.12	1	57.12	0.57	0.5050	10.13
Interaction	410.88	1	410.88	4.10	0.1359	10.13
Within	300.39	3	100.13			
Total	17761.36	6				

$\alpha = 0.05$; SS: sum of squares; df: degrees of freedom; MS: mean squares.

Summarising the results about machining induced residual stresses during AISI 304L drilling, the feed rate effect was by far the most significant factor. Opposing trends were observed for two-flute and four-flute cutting tools, since higher feed rate seemed to produce less residual stresses using the two-flute end mill and more residual stresses with a four-flute end mill. Using four-flute end mill, two plateaux could be discerned for each feed rate, with little effect for rotational speed. This is in good agreement with literature, as the feed rate was already pointed out as the most relevant process by previous work and cutting speed exerted little effect in residual stress introduction [73].

Intense compressive residual stress fields are also associated with strain hardening tendencies AISI 304L presents. Plus, Capello [74] affirms that in general the level of residual stresses increases with increasing mechanical properties. Brinksmeier *et al.* [48] suggests that considerable plastic deformation leads to compressive residual stresses, having the tool sharpness has a major influence. Compressive residual stresses were also observed during AISI 304 stainless steel turning by [49]. Given the feeds per tooth, cutting edge radius and AISI 304L mechanical properties, the high magnitude machining induced residual stresses found for most conditions is an expected result. The author believes that high speed machining may actually bring some benefits in the case of alloys prone to intense work hardening as AISI 304L, as the material resistance limits decrease with increasing temperatures in the shearing zone.

5.1.3 Microhardness

Microhardness mean values were plotted with a 95% confidence interval in Figure 5.15 and 5.16 using a two-flute end mill and a four-flute end mill respectively; the Sample 0 correspond to the base material. Paired Welch t-tests are presented in the Tables C.1, C.2, C.3 and C.4 and their respective results are commented further.

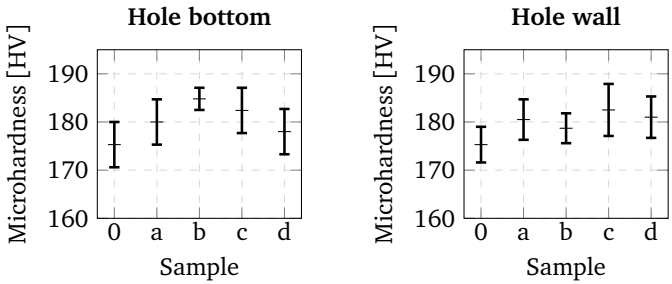

Figure 5.15 – Drilling effect on AISI 304L hardness using a two-flute square end mill.

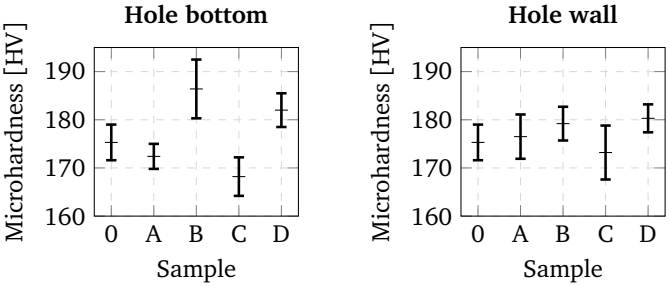

Figure 5.16 – Drilling effect on AISI 304L hardness using a four-flute square end mill.

In Table C.1, the drilling effect on the hole bottom microhardness using a two-flute square end mill is analysed. The combinations $v_f = 10$ mm/min and $n = 25,000$ rpm, $v_f = 20$ mm/min and $n = 40,000$ rpm did not produce significant changes in the hole bottom microhardness, while for the other cutting parameters combinations the microstructure were significantly changed.

Hole wall microhardness change using a two-flute square end mill is investigated in Table C.2. The hole walls microhardness increased for all the cutting parameters combinations, which endorses the highly compressive residual stresses found in the previous section.

Using a four-flute square end mill, the hole bottom microhardness suffered noticeable changes for most cutting parameters combinations, except for the $v_f = 10$ mm/min and $n = 25,000$ rpm, as seen in Table C.3, which was also the one that presented less machining residual stress introduction.

Table C.2 shows that significant changes in microhardness were found for $n = 25,000$ rpm, which are possibly associated with chip rubbing and burnishing at higher rates against the hole walls, as the chip pockets are smaller in a four-flute tool and their disposal becomes problematic.

Looking into an overall panorama, using a four-flute end mill

provokes less changes in the hole wall microstructure than using a two-flute end mill. However, no general trend was observed concerning the hole bottom microhardness values for both cutting tools. A possible explanation for this behaviour is the random built-up edges formation since AISI 304L favours this condition, concomitant to the excessive material smearing in the end mill centre, which happens in a more uncontrolled way since the cutting tool is not properly designed for drilling operations.

Since Blödorn [7] observed that hole walls suffered microhardness increases for all conditions tested and the present study found the same result for the two-flute square end mill, the mechanical influence predominance over the thermal effect is very clear, despite the low thermal conductivity and heat generated from tool friction and plastic deformation that makes the cutting zone reach high temperatures.

5.2 CARBON STEEL AISI 1020

5.2.1 Chip formation

Carbon steel AISI 1020 has two main constituents: ferrite and perlite. Ferrite presents a tendency to form unfavourable chips such as snarled and ribbon types due to its high deformability, being also prone to adhesion and built-up edge formation. On the other hand, perlite reduces adhesion and built-up edge formation tendencies, also helping to form more favourable chip forms [23]. Since the main carbon steel components present opposite effects, depending on their proportions good machining conditions may be expected.

(a) $v_f = 10$ mm/min and $n = 25,000$ rpm (b) $v_f = 20$ mm/min and $n = 25,000$ rpm

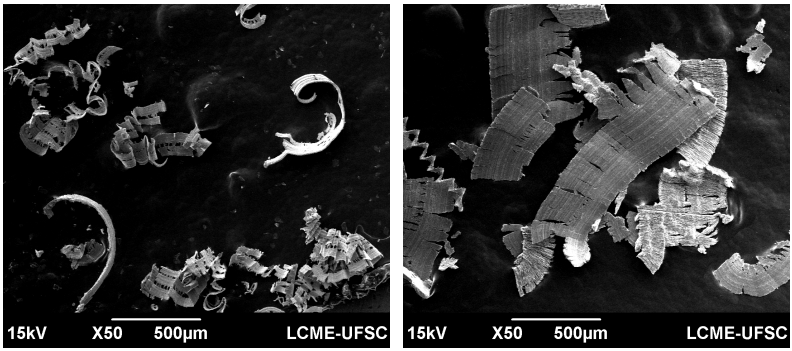

(c) $v_f = 10$ mm/min and $n = 40,000$ rpm (d) $v_f = 20$ mm/min and $n = 40,000$ rpm

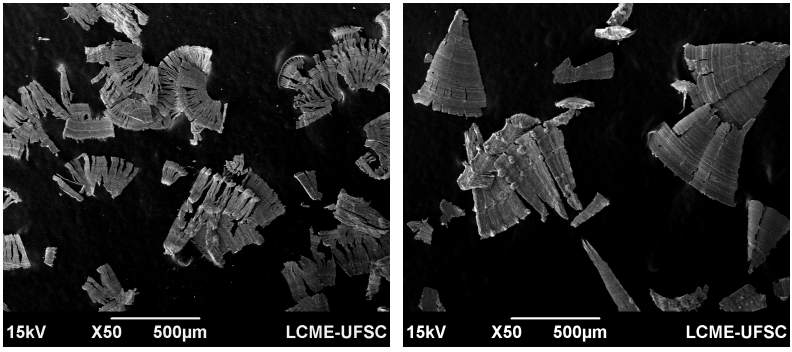

Figure 5.17 – Chip comparison using a two-flute square end mill during AISI 1020 drilling.

AISI 1020 drilling employing a two-flute end mill produced the chips shown in Figure 5.17. Using $v_f = 10$ mm/min, very thin and therefore fragile chips were formed for both rotational speeds, which is a desirable feature because it facilitates chip breakage. Thicker chips were obviously formed using $v_f = 20$ mm/min, presenting wider widths (about 400 μm) due to the larger cutting edge engagement. Using $v_f = 20$ mm/min and $n = 25,000$ rpm, a more continuous chip was formed, but it still seems to be very thin. Figure 5.18 shows in higher magnification that chip formation presented regular and periodic shear fronts, without excessive plastic deformation for all the tested conditions.

(a) $v_f = 10$ mm/min and $n = 25,000$ rpm (b) $v_f = 20$ mm/min and $n = 25,000$ rpm

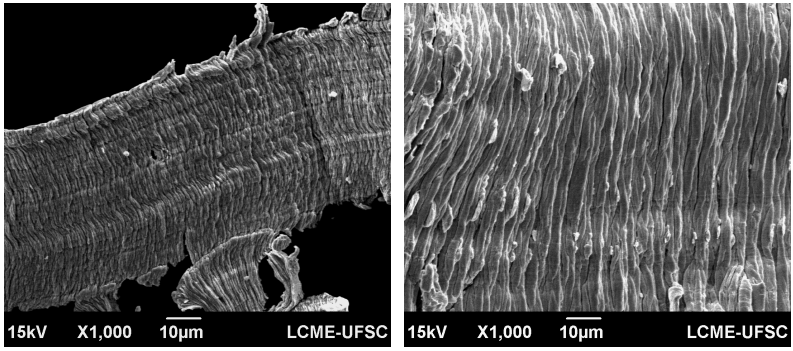

(c) $v_f = 10$ mm/min and $n = 40,000$ rpm (d) $v_f = 20$ mm/min and $n = 40,000$ rpm

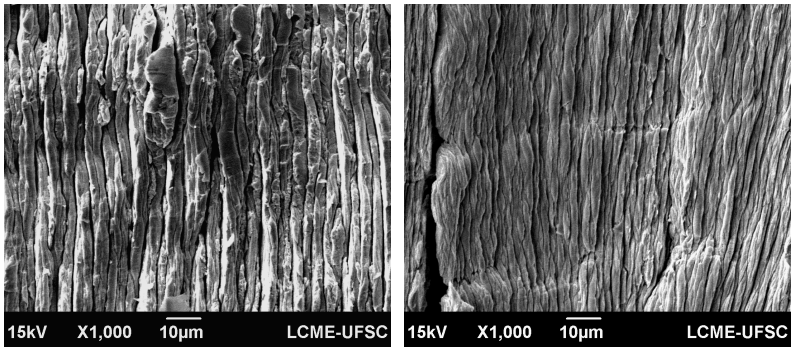

Figure 5.18 – Chip upper surface comparison using a two-flute square end mill during AISI 1020 drilling.

(a) $v_f = 10$ mm/min and $n = 25,000$ rpm (b) $v_f = 20$ mm/min and $n = 25,000$ rpm

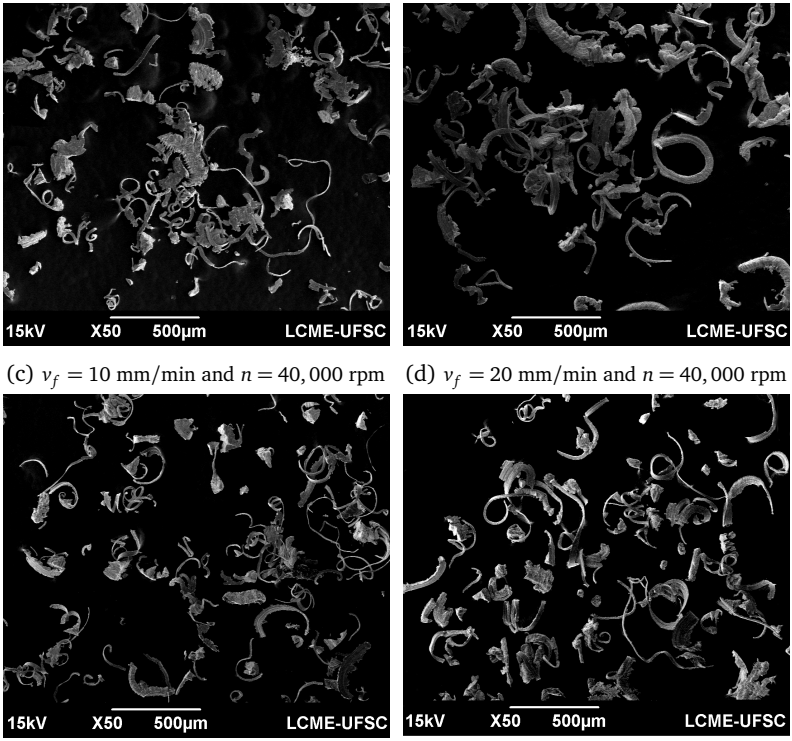

(c) $v_f = 10$ mm/min and $n = 40,000$ rpm (d) $v_f = 20$ mm/min and $n = 40,000$ rpm

Figure 5.19 – Chip comparison using a four-flute square end mill during AISI 1020 drilling.

Four-flute square end mill produced narrow and small chips as seen in Figure 5.19, with widths not greater than 70 µm. Using $n = 40,000$ rpm, narrower chips were noticeably formed. Figure 5.20 shows that similarly to two-flute cutting tool utilisation, chip formation occurred in regular shear fronts, but plastic deformation appears to be slightly worse in the chip borders as the feed per tooth is half of those obtained by a two-flute end mill. As commented previously, the cutting edge is not fully engaged in metal cutting using these cutting parameters combinations; nevertheless, the small portion that penetrates into the workpiece seems to be cutting satisfactorily the material. For these reasons, these chips seem to be adequate both from the machining point of view and ESPI utilisation.

(a) $v_f = 10$ mm/min and $n = 25,000$ rpm (b) $v_f = 20$ mm/min and $n = 25,000$ rpm

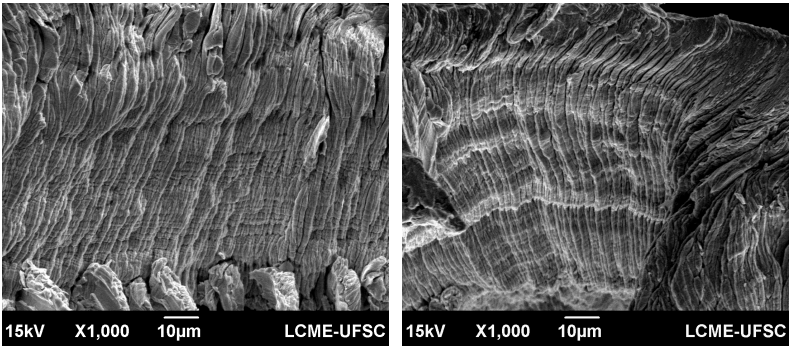

(c) $v_f = 10$ mm/min and $n = 40,000$ rpm (d) $v_f = 20$ mm/min and $n = 40,000$ rpm

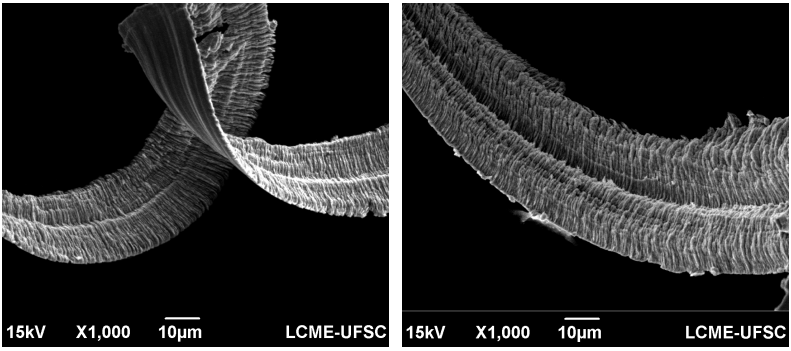

Figure 5.20 – Chip upper surface comparison using a four-flute square end mill during AISI 1020 drilling.

5.2.2 Machining induced residual stress

Figures 5.21 and 5.22 show maximum and minimum machining induced residual stresses mean values with their sample standard deviation for both cutting tools. AISI 1020 drilling with a four-flute end mill clearly introduces less machining induced residual stresses than using a two-flute end mill for almost all cutting parameters combinations and have a slightly tensile nature. In addition, their absolute values are considerably small, which is the close to the desired solution when applying the Hole-Drilling Method. Raw data are presented in Table B.2 – Appendix B. Machining induced residual stresses mean values and sample standard deviation are plotted in Tables 5.7 and 5.8.

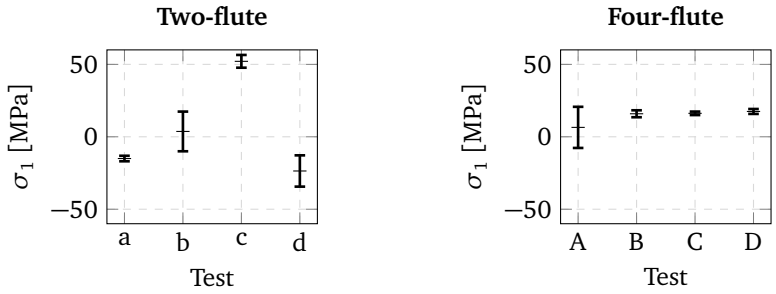

Figure 5.21 – Machining induced maximum residual stress σ_1 during AISI 1020 drilling.

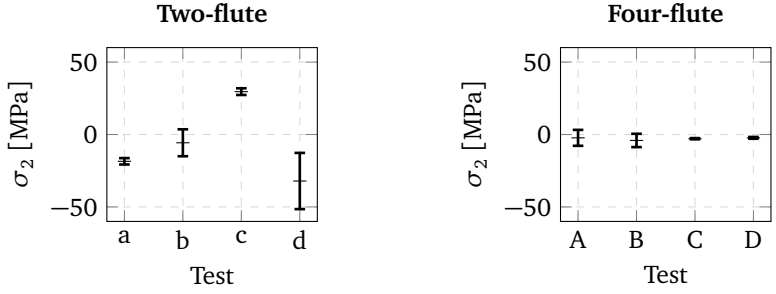

Figure 5.22 – Machining induced minimum residual stress σ_2 during AISI 1020 drilling.

Table 5.7 – Machining induced residual stresses in AISI 1020 drilling using a two-flute end mill.

Cutting parameters	σ_1 **[MPa]**	σ_2 **[MPa]**
25,000 rpm 10 mm/min	-15 ±2	-19 ±2
40,000 rpm 10 mm/min	4 ±14	-6 ±9
25,000 rpm 20 mm/min	52±4	30 ±2
40,000 rpm 20 mm/min	-24±11	-32 ±19

Table 5.8 – Machining induced residual stresses in AISI 1020 drilling using a four-flute end mill.

Cutting parameters	σ_1 **[MPa]**	σ_2 **[MPa]**
25,000 rpm 10 mm/min	6 ±14	-2 ±5
40,000 rpm 10 mm/min	16 ±2	-4 ±5
25,000 rpm 20 mm/min	16 ±1	-3 ±1
40,000 rpm 20 mm/min	18 ±2	-2 ±1

Figure 5.23 shows interaction plots for maximum residual stress σ_1 using a two-flute square end mill. Even though both feed rate and rotational speed provoke changes in the amount of machining induced residual stresses, the interaction between these two variables undoubtedly influences heavily this process, as reported in Table 5.9. However, using v_f =10 mm/min seems to be a better choice as the absolutes values are close to zero using both rotational speeds; a similar trend was also observed for minimum residual

stress σ_2, as seen in Figure 5.24. Table 5.10 shows that interaction between v_f and n also produces heavier effects on machining induced residual stress when compared to solely rotational speed, while feed rate did not exert much influence.

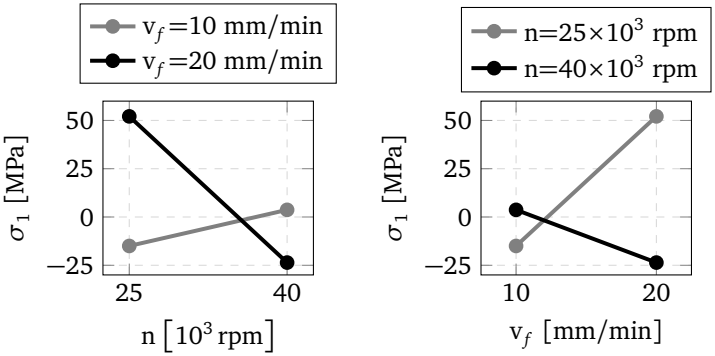

Figure 5.23 – Interaction plots for maximum residual stress σ_1 using a two-flute square end mill during AISI 1020 drilling.

Table 5.9 – ANOVA table for maximum residual stress σ_1 using a two-flute square end mill during AISI 1020 drilling.

Source of Variation	*SS*	*df*	*MS*	*F-ratio*	*P-value*	F_{crit}
Feed rate	1185.90	1	1185.90	9.61	0.0147	5.32
Rotational speed	2437.06	1	2437.06	19.76	0.0022	5.32
Interaction	6695.03	1	6695.03	54.27	0.0001	5.32
Within	986.84	8	123.35			
Total	11304.83	11				

$\alpha = 0.05$; SS: sum of squares; df: degrees of freedom; MS: mean squares.

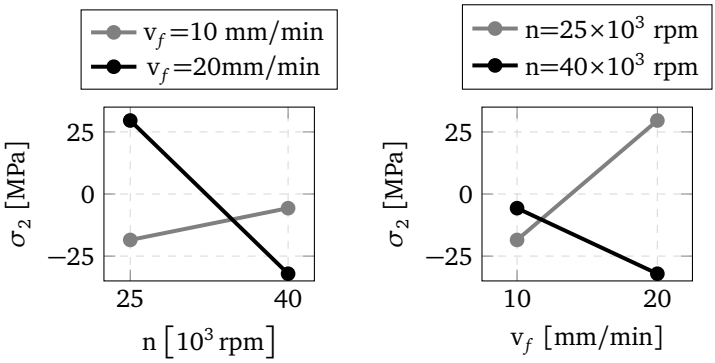

Figure 5.24 – Interaction plots for minimum residual stress σ_2 using a two-flute square end mill during AISI 1020 drilling.

Table 5.10 – ANOVA table for minimum residual stress σ_2 using a two-flute square end mill during AISI 1020 drilling.

Source of Variation	*SS*	*df*	*MS*	*F-ratio*	*P-value*	F_{crit}
Feed rate	354.84	1	354.84	2.00	0.1947	5.32
Rotational speed	1795.03	1	1795.03	10.13	0.0129	5.32
Interaction	4164.49	1	4164.49	23.51	0.0013	5.32
Within	1417.25	8	177.16			
Total	7731.61	11				

$\alpha = 0.05$; SS: sum of squares; df: degrees of freedom; MS: mean squares.

Using a four-flute end mill, better results were obtained by the combination of v_f =10 mm/min and $n = 25{,}000$ rpm for maximum residual stress σ_1, since the measured values were closer to zero as seen in Figure 5.25. Figure 5.26 shows that very small minimum residual stress σ_2 are introduced, but lower values are reached using $n = 25{,}000$ rpm. ANOVA presented in Tables 5.11 and 5.12 confirms the suspicion from Figure 5.21 and 5.22 that neither v_f nor n impact on machining induced residual stresses for the cutting parameters combinations tested. As mentioned before for the AISI 304L case, higher mechanical properties result in higher residual stress produced; comparing these two steels, this behaviour was observed.

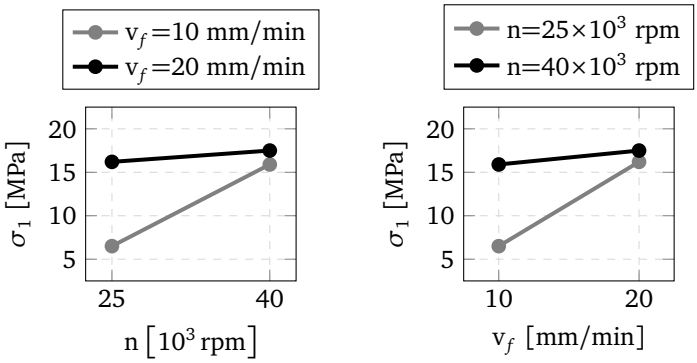

Figure 5.25 – Interaction plots for maximum residual stress σ_1 using a four-flute square end mill during AISI 1020 drilling.

Table 5.11 – ANOVA table for maximum residual stress σ_1 using a four-flute square end mill during AISI 1020 drilling.

Source of Variation	*SS*	*df*	*MS*	*F-ratio*	*P-value*	F_{crit}
Feed rate	95.15	1	95.15	1.20	0.3060	5.32
Rotational speed	88.22	1	88.22	1.11	0.3232	5.32
Interaction	49.14	1	49.14	0.62	0.4546	5.32
Within	636.72	8	79.59			
Total	869.23	11				

$\alpha = 0.05$; SS: sum of squares; df: degrees of freedom; MS: mean squares.

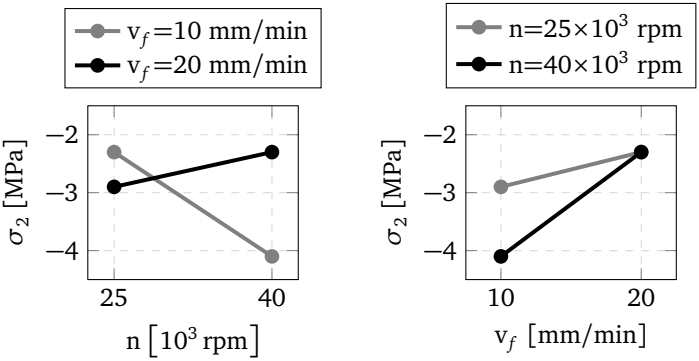

Figure 5.26 – Interaction plots for minimum residual stress σ_2 using a four-flute square end mill during AISI 1020 drilling.

Table 5.12 – ANOVA table for minimum residual stress σ_2 using a four-flute square end mill during AISI 1020 drilling.

Source of Variation	*SS*	*df*	*MS*	*F-ratio*	*P-value*	F_{crit}
Feed rate	1.11	1	1.11	0.06	0.8176	5.32
Rotational speed	1.25	1	1.25	0.06	0.8062	5.32
Interaction	4.15	1	4.15	0.21	0.6566	5.32
Within	155.97	8	19.50			
Total	162.48	11				

$\alpha = 0.05$; SS: sum of squares; df: degrees of freedom; MS: mean squares.

5.2.3 Microhardness

Figures 5.27 and 5.28 shows microhardness mean values plotted with a 95% confidence interval using a two-flute and a four-flute end mills respectively; again, Sample 0 correspond to the base material.

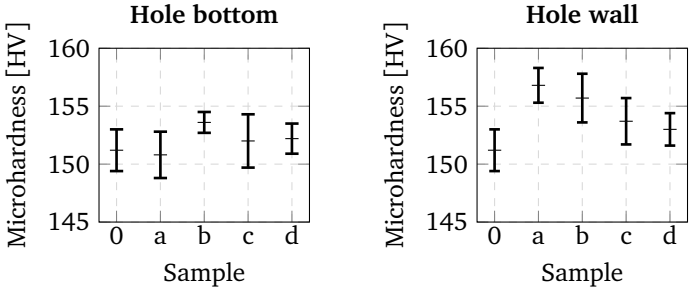

Figure 5.27 – Drilling effect on AISI 1020 hardness using a two-flute square end mill.

When employing a two-flute end mill, the hole bottom microhardness was only altered using the combination $v_f = 10$ mm/min and $n = 40,000$ rpm, while hole walls microhardness values increased significantly for all the cutting parameters combinations, according to Tables C.5 and C.6 respectively.

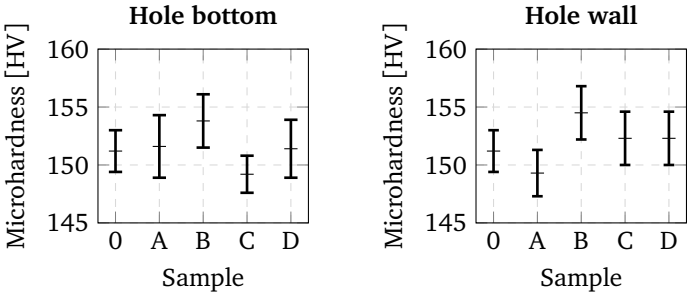

Figure 5.28 – Drilling effect on AISI 1020 hardness using a four-flute square end mill.

Using a four-flute end mill, the hole bottom microhardness suffered alteration solely using the combination $v_f = 20$ mm/min and $n = 25,000$ rpm; however, this is not a sure assertive since P-value was too close to the significance level and the null hypothesis were barely rejected, as seen in Table C.7. Only for the hole wall drilled with $v_f = 10$ mm/min and $n = 40,000$ rpm microhardness values increased, according to Table C.8.

Following the same trend seen in machining induced residual stress measurements in which little modification was introduced into the microstructure, microhardness values were barely changed when drilling AISI 1020 with a four-flute end mill. Particularly in the case in which the smaller feed per tooth is reached ($v_f = 10$ mm/min and $n = 40,000$ rpm), changes in microhardness were recurrent for both cutting tools. Blödorn [7] found decrease in microhardness on the hole surroundings for this material, suggesting that the thermal load in the present process is much lower than those achieved with MTRES due to much smaller rotational speeds, which results in lower interaction times with a rotating cutting tool and heat generation from frictional effects.

5.3 ALUMINIUM ALLOY AA 6061

5.3.1 Chip formation

Due to AA 6061 aluminium alloy composition, hard and brittle silicon inclusions facilitate chip breakage. Aluminium alloys often present more favourable chips the harder they are [23], for this reason AA 6061–T4 and AA 6061–T4 are known by their good machinability. However, workpiece material is AA 6061–O corresponding to annealed condition, too soft and for this reason chip formation may be problematic since this temper favours built-up edge formation [58].

(a) $v_f = 10$ mm/min and $n = 25,000$ rpm (b) $v_f = 20$ mm/min and $n = 25,000$ rpm

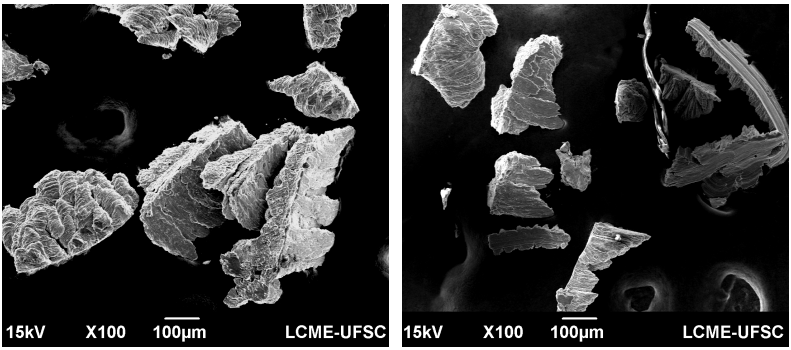

(c) $v_f = 10$ mm/min and $n = 40,000$ rpm (d) $v_f = 20$ mm/min and $n = 40,000$ rpm

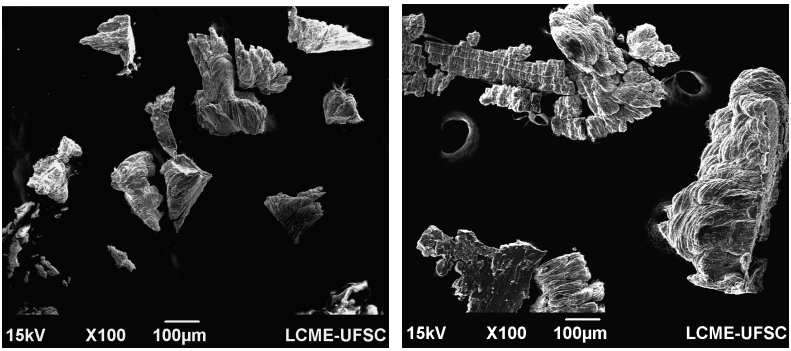

Figure 5.29 – Chip comparison using a two-flute square end mill during AA 6061 drilling.

Using a two-flute end mill, Figure 5.29 shows that AA 6061 chips that are significantly thicker (around 100 μm) than those formed during both steels machining. A viscous and irregular appearance was observed. The stick-slip mechanism is crucial in the chip formation process since it affects chip curl and the degree of plastic deformation [70]. This mechanism is particularly influenced by the strong adhesion tendency presented by this soft material, especially when in contact with a cutting edge with a grooved surface finish. Figure 5.30 shows that for $v_f = 10$ mm/min, chips present more intense plastic deformation effects than using $v_f = 20$ mm/min, in which more organized layers were formed as the chip slips. Using $v_f = 20$ mm/min and $n = 25,000$ rpm particularly, a lamellar pattern is observed.

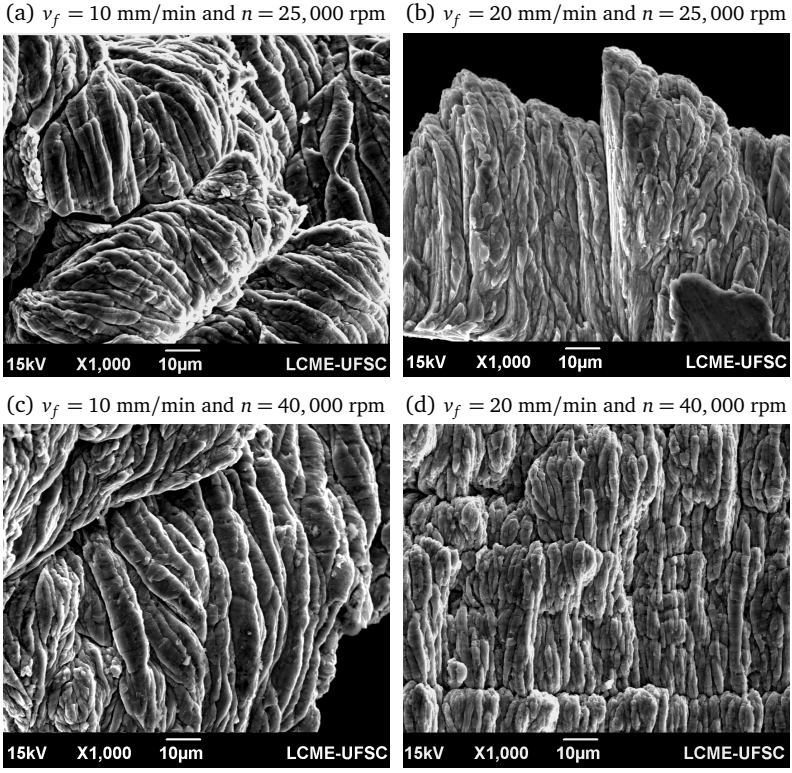

Figure 5.30 – Chip upper surface comparison using a two-flute square end mill during AA 6061 drilling.

Figure 5.31 shows chips formed using a four-flute end mill. Employing $v_f = 10$ mm/min and $n = 40,000$ rpm, thicker structures that barely resembles a chip were formed, while for $v_f = 20$ mm/min there are regions that present regular layers and others that seem to be melted material agglomerates. These images suggest that the cutting parameters combination tested are in a cutting regime transition range, microstructural changes and process oscillations seem to exert great influence in chip formation. Figure 5.32 suggests that $v_f = 10$ mm/min and $n = 40,000$ rpm produces a chip mostly by ploughing effects instead of proper metal cutting, since this cutting parameter combination results in smaller feed per tooth than the other cases, that seem to generate more regular shear fronts.

(a) $v_f = 10$ mm/min and $n = 25,000$ rpm (b) $v_f = 20$ mm/min and $n = 25,000$ rpm

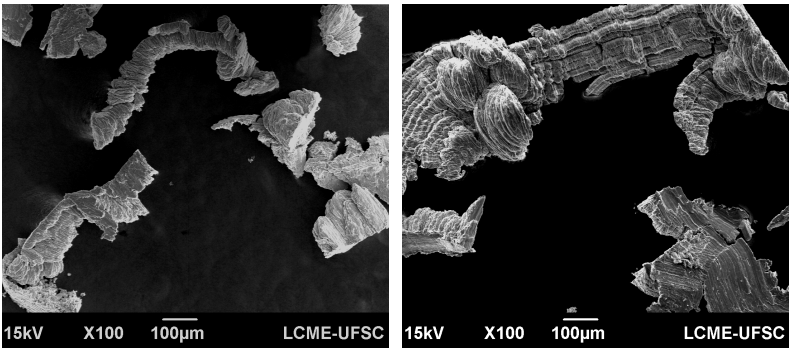

(c) $v_f = 10$ mm/min and $n = 40,000$ rpm (d) $v_f = 20$ mm/min and $n = 40,000$ rpm

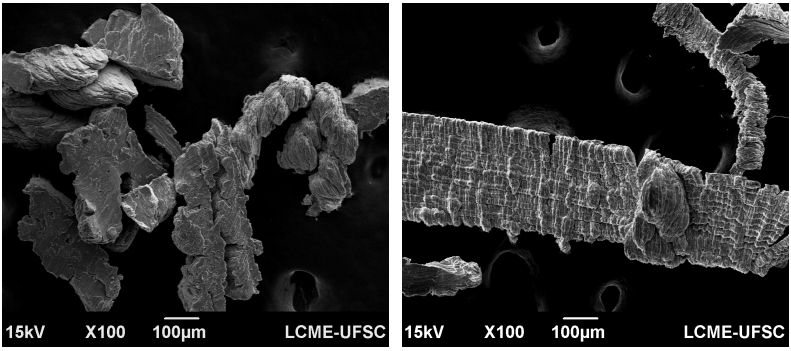

Figure 5.31 – Chip comparison using a four-flute square end mill during AA 6061 drilling.

(a) $v_f = 10$ mm/min and $n = 25,000$ rpm

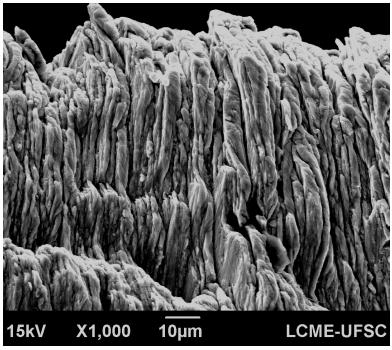

(b) $v_f = 20$ mm/min and $n = 25,000$ rpm

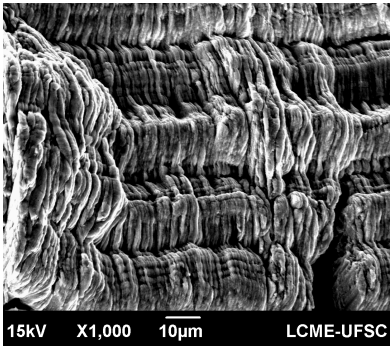

(c) $v_f = 10$ mm/min and $n = 40,000$ rpm

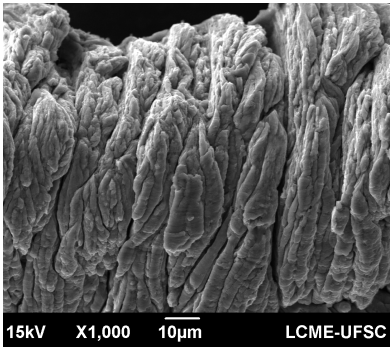

(d) $v_f = 20$ mm/min and $n = 40,000$ rpm

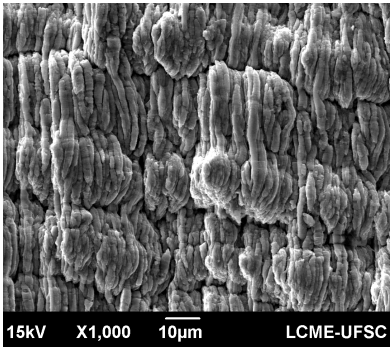

Figure 5.32 – Chip upper surface comparison using a four-flute square end mill during AA 6061 drilling.

5.3.2 Machining induced residual stress

Maximum and minimum machining induced residual stresses mean values with their sample standard deviation for both cutting tools during AA 6061 drilling are presented in Figure 5.33 and 5.34 respectively. Residual stress measurements can be found in Table B.3 – Appendix B. Four-flute end mill performed better than two-flute end mill for most cutting parameters combinations, reaching lower residual stress absolute values and sample standard deviations. Machining induced residual stresses mean values and sample standard deviations introduced during AA 6061 drilling are shown in Tables 5.13 and 5.14.

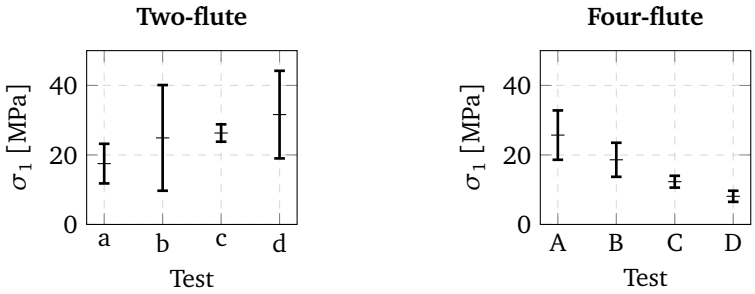

Figure 5.33 – Machining induced maximum residual stress σ_1 during AA 6061 drilling.

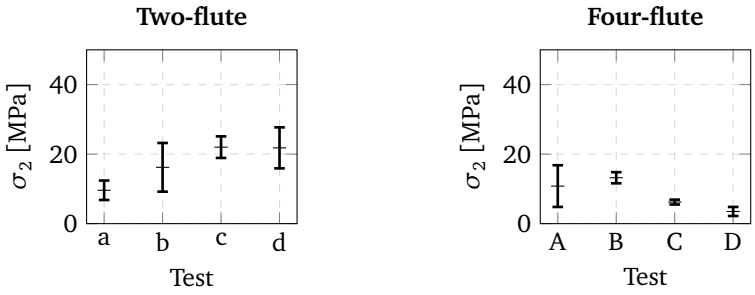

Figure 5.34 – Machining induced minimum residual stress σ_2 during AA 6061 drilling.

Table 5.13 – Machining induced residual stresses in AA 6061 drilling using a two-flute end mill.

Cutting parameters	σ_1 **[MPa]**	σ_2 **[MPa]**
25,000 rpm 10 mm/min	18 ±6	10±3
40,000 rpm 10 mm/min	25 ±15	16 ±7
25,000 rpm 20 mm/min	26 ±2	22 ±3
40,000 rpm 20 mm/min	32 ±13	22 ±6

Table 5.14 – Machining induced residual stresses in AA 6061 drilling using a four-flute end mill.

Cutting parameters	σ_1 **[MPa]**	σ_2 **[MPa]**
25,000 rpm 10 mm/min	26 ±7	11±6
40,000 rpm 10 mm/min	19 ±5	13±2
25,000 rpm 20 mm/min	12 ±2	6±1
40,000 rpm 20 mm/min	8 ±2	3 ±1

Lower maximum residual stresses σ_1 using a two-flute end mill were found using $v_f = 10$ mm/min or $n = 25,000$ mm/min, as seen in Figure 5.35. According to ANOVA analysis in Table 5.15, none of the cutting parameters or their interaction resulted in a significative source of variation in residuals stresses σ_1.

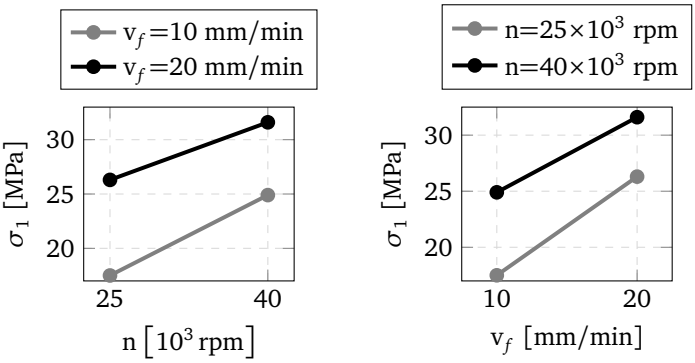

Figure 5.35 – Interaction plots for maximum residual stress σ_1 using a two-flute square end mill during AA 6061 drilling.

Table 5.15 – ANOVA table for maximum residual stress σ_1 using a two-flute square end mill during AA 6061 drilling.

Source of Variation	*SS*	*df*	*MS*	*F-ratio*	*P-value*	F_{crit}
Feed rate	181.04	1	181.04	1.13	0.3196	5.32
Rotational speed	118.64	1	118.64	0.74	0.4153	5.32
Interaction	3.36	1	3.36	0.02	0.8886	5.32
Within	1286.15	8	160.77			
Total	1589.18	11				

$\alpha = 0.05$; SS: sum of squares; df: degrees of freedom; MS: mean squares.

A similar tendency is observed in minimum residual stresses σ_2 using a two-flute end mill: $v_f = 10$ mm/min or $n = 25,000$ mm/min produced less residual stresses when confronted to the another corresponding cutting parameter (Figure 5.36). Table 5.16 shows that the feed rate is the main source of variation in minimum residual stresses σ_2.

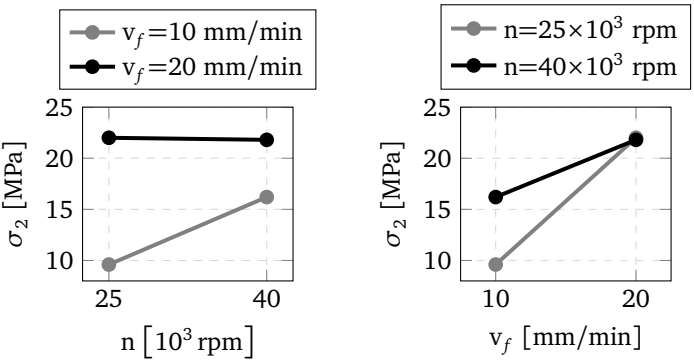

Figure 5.36 – Interaction plots for minimum residual stress σ_2 using a two-flute square end mill during AA 6061 drilling.

Table 5.16 – ANOVA table for minimum residual stress σ_2 using a two-flute square end mill during AA 6061 drilling.

Source of Variation	*SS*	*df*	*MS*	*F-ratio*	*P-value*	F_{crit}
Feed rate	243.39	1	243.39	6.41	0.0351	5.32
Rotational speed	30.24	1	30.24	0.80	0.3981	5.32
Interaction	35.75	1	35.75	0.94	0.3602	5.32
Within	303.68	8	37.96			
Total	613.06	11				

$\alpha = 0.05$; SS: sum of squares; df: degrees of freedom; MS: mean squares.

A contrary trend is perceived when hole drilling is performed with a four-flute end mill (Figure 5.37), as lower maximum residual stresses σ_1 can be achieved with $v_f = 20$ mm/min or $n = 40,000$ mm/min. For this case, feed rates also impact significantly on the residual stress σ_1 introduction, from ANOVA analysis in Table 5.17. The same behaviour was detected in Figure 5.38 and Table 5.18 for minimum residual stresses σ_2.

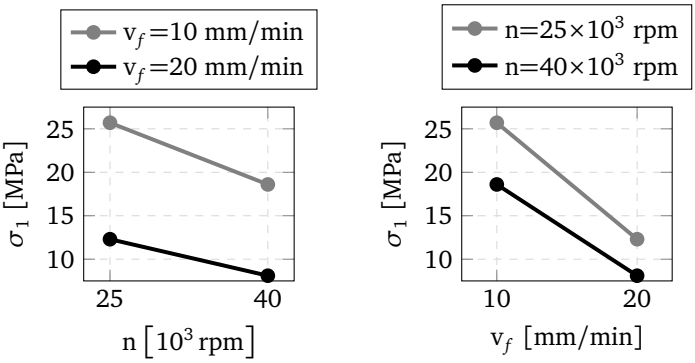

Figure 5.37 – Interaction plots for maximum residual stress σ_1 using a four-flute square end mill during AA 6061 drilling.

Table 5.17 – ANOVA table for maximum residual stress σ_1 using a four-flute square end mill during AA 6061 drilling.

Source of Variation	*SS*	*df*	*MS*	*F-ratio*	*P-value*	F_{crit}
Feed rate	431.33	1	431.33	14.49	0.0052	5.32
Rotational speed	96.98	1	96.98	3.26	0.1087	5.32
Interaction	6.23	1	6.23	0.21	0.6596	5.32
Within	238.15	8	29.77			
Total	772.69	11				

$\alpha = 0.05$; SS: sum of squares; df: degrees of freedom; MS: mean squares.

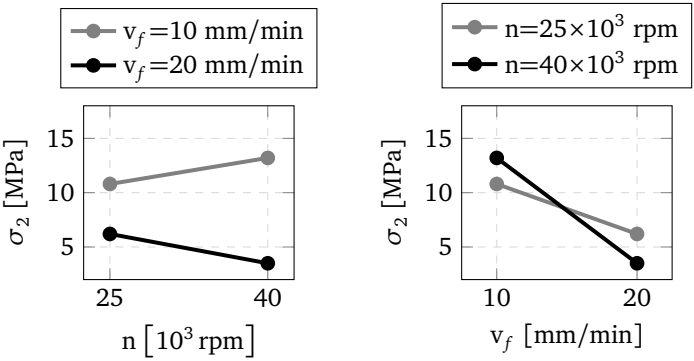

Figure 5.38 – Interaction plots for minimum residual stress σ_2 using a four-flute square end mill during AA 6061 drilling.

Table 5.18 – ANOVA table for minimum residual stress σ_2 using a four-flute square end mill during AA 6061 drilling.

Source of Variation	*SS*	*df*	*MS*	*F-ratio*	*P-value*	F_{crit}
Feed rate	154.44	1	154.44	10.21	0.0127	5.32
Rotational speed	0.09	1	0.09	0.01	0.9411	5.32
Interaction	19.84	1	19.84	1.31	0.2852	5.32
Within	121.04	8	15.13			
Total	295.41	11				

$\alpha = 0.05$; SS: sum of squares; df: degrees of freedom; MS: mean squares.

Tensile machining induced residual stresses were found for both cutting tools, indicating the thermal load predominance over the mechanical effects, since low energies are required to shear soft metals. This behaviour is in good agreement with literature, since tensile residual stresses in 7075 aluminium alloy high-speed milling was already reported by Tang *et al.* [75] using a worn cutting tool. Even if a new cutting tool was used during this experiment, the end mill can be considered dull since the first drilling given the ratio between f_z and ρ as aforementioned.

5.3.3 Microhardness

During the microhardness measurements in aluminium alloy AA 6061 samples, the bulk material microhardness differed from workpiece to workpiece. To keep a fair comparison, each hole microhardness value was compared to bulk material microhardness value for the same workpiece. Microhardness mean values were plotted with a 95% confidence interval in Figure 5.39 and 5.40.

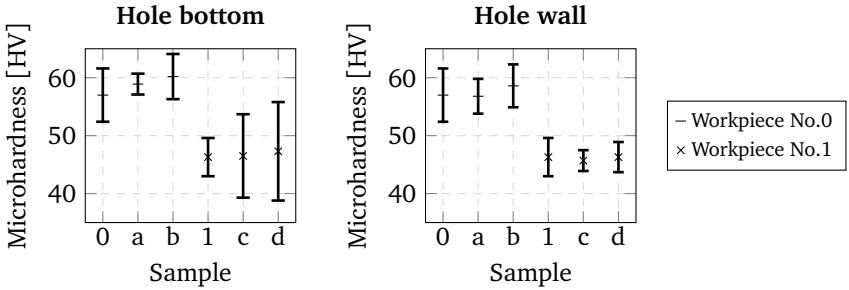

Figure 5.39 – Drilling effect on AA 6061 hardness using a two-flute square end mill.

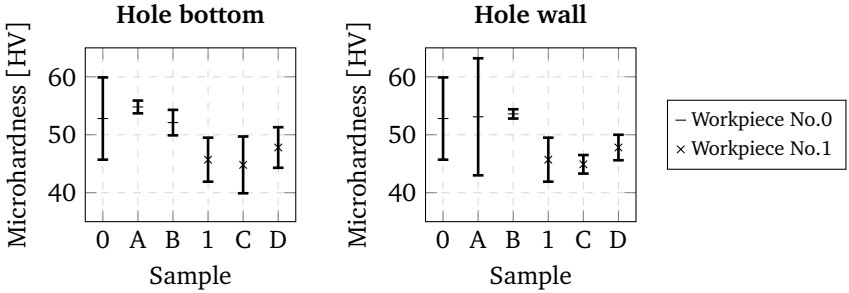

Figure 5.40 – Drilling effect on AA 6061 hardness using a four-flute square end mill.

In Table C.9 the effect of the drilling using a two-flute end mill on the hole bottom microhardness is analysed. Drilling using the lowest feed rates ($v_f = 10$ mm/min) provoked an increase in the hole bottom microhardness; H_0 was not tightly rejected for both cases at $\alpha = 0.05$ level. On the other hand, drilling performed with higher feed rates ($v_f = 20$ mm/min) barely affected the hole bottom microhardness; strong evidences of this fact are provided by the high P-values found.

Hole wall microhardness values were not significantly changed by the drilling using a two-flute end mill in all the tested combination of parameters, as shown in Table C.10. High P-values obtained for this set of tests indicate weak evidence that the metal cutting introduced severe non-homogeneities into the hole wall. Heat generation was not intense

since microhardness values did not suffer a noticeable decrease, which is a reasonable outcome since the energy consumed to machine aluminium alloys are relatively low when compared to other metals. Even though ASTM E837 – 13a [3] expresses a concern about the rubbing between the hole wall and a square end mill peripheral cutting edges, low friction between cutting tool and workpiece can also be deduced from this result, indicating a favourable combination of cutting tool coating and workpiece material; thus, the utilisation of an inverted-cone end mill to avoid unnecessary rubbing as recommended by the standard may not bring much benefit over a properly selected square end mill.

As seen in Table C.11, the hole bottom microhardness values were not strongly affected by drilling for almost all cases ($v_f = 10$ mm/min and $n = 25,000$ rpm; $v_f = 20$ mm/min and $n = 25,000$ rpm; $v_f = 20$ mm/min and $n = 40,000$ rpm). It is worth mentioning that H_0 could be barely rejected in $v_f = 10$ mm/min and $n = 40,000$ rpm at $\alpha = 0.05$, since the P-value was 0.047; i.e. there is not strong evidence to assert that the drilling is producing a significant change in the hole bottom microhardness for this condition.

In Table C.12, a similar trend is observed in the hole wall microhardness for the following cutting conditions: $v_f = 10$ mm/min and $n = 25,000$ rpm; $v_f = 10$ mm/min and $n = 40,000$ rpm; $v_f = 20$ mm/min and $n = 25,000$ rpm, in which the drilling seems to exert little influence in the surrounding microstructure. However, for the case $v_f = 20$ mm/min and $n = 40,000$ rpm, the hole wall microhardness value increased significantly, indicating a work hardening. A possible explanation is the chip adhesion on the cutting tool surface that may have happened during this drilling operation, in a way that the material was smeared against the hole wall since chip disposal becomes more problematic with increasing flute number.

Summarising briefly, aluminium alloy AA 6061 drilling produced minor changes in the hole surroundings microhardness for both two-flute and four-flute end mills, indicating that the microstructure was not strongly disturbed by the metal cutting process; this outcome corroborates the small

machining induced residual stresses measured, as explored in the previous section, and denotes a good choice of cutting tool and cutting parameters for HDM residual stress measurement purposes in this type of material. During AA 6061 drilling, Blödorn [7] reported a decrease in the hole surroundings microhardness, i.e. the temperature rise was excessive despite the material high thermal diffusivity that dissipates heat quickly. For this reason, the process seems to be less aggressive than the used by MTRES also for this material.

5.4 HOLE GEOMETRY

Figure 5.41 presents a comparison on the same scale between the hole cross-sectional profile obtained when drilling all tested materials with the 1.6 mm inverted-cone dental end mill currently employed by MTRES and the selected square end mills. All holes are 1 mm deep, as advised by the standard [3].

(a) Dental end mill, AISI 304L [7]

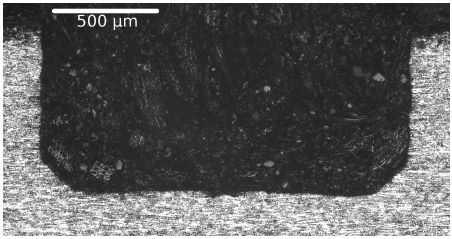

(b) Square end mill, AISI 304L

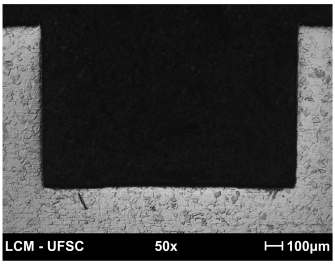

(c) Dental end mill, AISI 1020 [7]

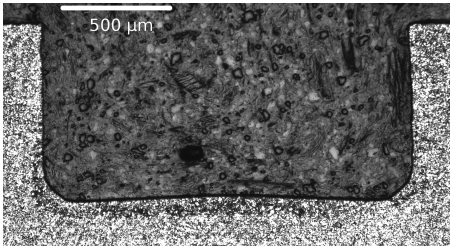

(d) Square end mill, AISI 1020

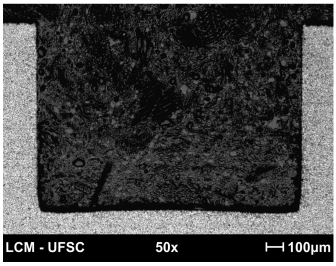

(e) Dental end mill, AA 6061 [7]

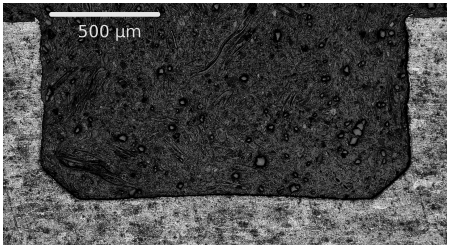

(f) Square end mill, AA 6061

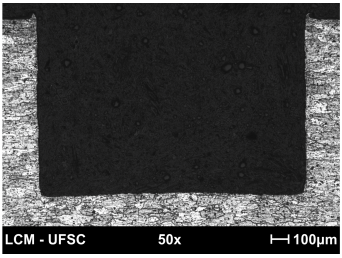

Figure 5.41 – Hole profiles comparison.

Clearly, square end mills generate a geometry closer to the ideal cylindrical profile suggested by ASTM E837 since they do not present the

chamfer. This element was introduced in the inverted-cone dental end mill design to increase tool tip robustness. Even with the chamfer, tool tip breakage was often reported using the inverted-cone dental end mill [7, 42].

When using this inverted-cone end mill, residual stress calculations may present significant errors if correction coefficients in the computational model are not properly adjusted to this complex geometry, since the chamfer size is comparable to a drilling step and changes significantly the stress relief distribution. Sharper corners were obtained using the square end mills, which have a radius much smaller than the drilling steps and therefore standardized correction coefficients could be used without introducing significant errors.

Another important influence that contributed to the obtained hole geometries is the machine tool. Even though the employed end mills differ only 0.1 mm in diameter, the hole diameters obtained with MTRES clearly are at least 0.2 mm wider. The pneumatic turbine use associated with low rigidity bearings may have provoked significant run-outs. Certainly, these features must be improved in the new MTRES drilling module design and will also help to avoid constant tool breakages.

6 CONCLUSIONS

In this chapter, the main conclusions drawn from this work are summarized and ideas for further works are pointed out.

6.1 CONCLUSIONS

In this work, cutting tools and cutting parameters combinations were selected and tested concerning the Hole-Drilling Method application with ESPI to measure displacements both from machining and metrological perspectives. Feed rate and rotational speed effects on machining induced residual stresses and microhardness were investigated in three types of material.

During preliminary tests, snarled chips were formed in AISI 304L drilling using $n = 10{,}000$ rpm at all feed rates, and for this reason this rotational speed was not used further. This continuous chip proved to be extremely prejudicial to the interferogram data reliability, since the reference surface was scratched during the end mill rotation. Hence, cutting parameters that favour continuous chip formation should be avoided whenever ESPI is being used to measure strains. Powdery or too thin chips associated with poor metal cutting process were observed when using v_f =1 mm/min, being also eliminated from the final tests. Burr formation do not pose a problem to the optical measuring process, since the burr is very small and the useful measuring area is far from it.

The combination of workpiece material, cutting tool geometry, cutting tool coating and cutting parameters during stainless steel AISI 304L dry drilling provoked an intense compressive stress state, inadequate to residual stress measurement purposes for most tested parameters, except for v_f =10 mm/min and $n = 25{,}000$ rpm, which resulted in a machining induced maximum residual stress $\sigma_1 = 4 \pm 10$ MPa. Microhardness values increased in almost all the cases when this property experienced significant change,

which means that the plastic deformation is the predominant effect over heating from frictional effects; this is in good agreement with compressive residual stresses found in most conditions, which may be explained by the AISI 304L tendency to work hardening.

Favourable chips were formed during AISI 1020 drilling, presenting small sizes and being properly cut as the chip upper surface presented regularly formed shear fronts, however the v_f =20 mm/min and $n = 25{,}000$ rpm using a two-flute end mill seemed to favour the undesired continuous chip formation. Using a four-flute cutting tool, smaller and narrower chips were obtained, being possibly the preferred option since chip removal by suction would be easier; besides, low machining induced residual stresses were observed for all cutting parameters combinations, in particular using v_f =10 mm/min and $n = 25{,}000$ rpm that resulted in a machining induced maximum residual stress $\sigma_1 = 6 \pm 14$ MPa. Another good combination was v_f =10 mm/min and $n = 40{,}000$ rpm using a two-flute end mill, that yielded $\sigma_1 = 4 \pm 14$ MPa. As in AISI 304L steel, microhardness values increased with drilling in almost all the conditions this property was significantly altered.

When drilling AA 6061, minimum chip thickness is likely within the tested feed per tooth range, as two chip upper surface patterns were clearly distinguished. Even though AA 6061 chips seemed to be intensely deformed, it may be a consequence of how material softness, low melting temperature and its tendency to adhere on the cutting tool surface affects the stick-slip mechanism, as the chip is removed from the cutting area at lower rates than it is produced. In general, four-flute square end mills overall performance was better than those of two-flute square end mills; while the former presented lower machining induced residual stresses absolute values and low data dispersion, the latter presented greater data scattering and introduced higher stress levels. A machining induced maximum residual stress $\sigma_1 = 8 \pm 2$ MPa obtained with v_f =20 mm/min and $n = 40{,}000$ rpm seemed to be the best solution for AA 6061. Microhardness values were mostly unaffected by drilling and increased in all instances a significant modification was spotted.

The main outputs of this work are shown in Table 6.1, in which the recommended solutions and their characteristics are summarised.

Table 6.1 – Recommended cutting parameters combinations and their features.

	AISI 304L	**AISI 1020**	**AA 6061**
Maximum residual stress	4 ±10	6 ±14	8 ±2
Minimum residual stress	-7 ±6	-2 ±5	3 ±1
Cutting parameters	25,000 rpm 10 mm/min	25,000 rpm 10 mm/min	40,000 rpm 20 mm/min
Cutting tool	Four-flute	Four-flute	Four-flute
Chip form	Favourable	Favourable	Favourable

Another important remark is that residual stress measurements presented low sample standard deviation, despite having only few available samples. This result may be attributed to the machine tool high rigidity, and also indicates that the end mill used in this work can properly drill several holes without suffering aggressive tool wear that would justify the frequent replacement by a new cutting tool.

The microhardness increases in almost all samples suggest that the thermal effect on the microstructure due to high rotational speeds was lesser than the plastic deformation influence likely related to the chip burnishing against the hole surfaces.

Hole geometries obtained with the selected square end mills were compared to the inverted-cone end mills currently employed by MTRES. The new cutting tool produces a hole geometry closer to the ideal geometry suggested by ASTM E837 – 13a. Evidence shows that MTRES drilling module rigidity is an attribute to be improved.

No general trend or rule of thumb can be given for the tested materials regarding both machining induced residual stresses and microhardness change, since the author believes that the cutting parameters combinations were in the transition from micromachining to macromachining; in this gray zone range, phenomena are not well-delineated. Nonetheless, feed rate was highlighted in many ANOVA analyses as the most important factor concerning machining induced residual stress within the tested cutting parameters range.

Among the cutting tool and cutting parameters combinations, some conditions introduced low machining induced residual stresses into the workpieces material and can be incorporated in a future MTRES version. With this improvement, errors associated to the drilling process can be minimized during a real residual stress evaluation.

6.2 SUGGESTIONS FOR FUTURE WORK

Further work is yet to be done in the following aspects, regarding the Hole-Drilling Method context:

- decrease even more the allowed rotational speed, to reach values recommended by machining literature and verify whether a less retroactive residual stress measurement is possible;
- include recommendations also about the feed rates, instead of only informing the cutting tool types and the rotational speed;
- use a proper tool to perform a drilling operation and change the standardised coefficients accordingly.

Concerning MTRES design, the proposed improvements are:

- design and validate an electrical drill using a brushless motor for better rotational speed control in a closed-loop;
- implement the cutting parameters and cutting tool used in the present work;
- study the cutting tool effect using the dental inverted-cone end mill currently used in MTRES, under the same cutting conditions

explored by this work;

- investigate tool wear evolution using a single end mill to drill using only one cutting parameter combination with the purpose of establishing the tool life that can be achieved with the proposed drilling process;
- provide a more stable, smoother and continuous feed replacing the stepper motor with a sliding linear motor, such as ball screws actuators;
- replace the dental turbine assembly in which only dental burrs fit with a chuck compatible with drills for metal cutting to make the drilling module more versatile;
- improve the drilling module rigidity;
- test API grade steels that are actually used in the oil and gas industry as workpiece material.

BIBLIOGRAPHY

[1] MACHERAUCH, E. Residual stresses. In: SIH, G.; SOMMER, E.; DAHL, W. (Ed.). *Application of Fracture Mechanics to Materials and Structures*. : Springer Netherlands, 1984. p. 157–192.

[2] JAMES, M. R. Introduction. In: *Handbook of Measurement of Residual Stresses*. : Fairmont Press, 1996. Chap. 1, p. 1–4.

[3] ASTM INTERNATIONAL. *ASTM E837 – 13a – Standard Test Method for Determining Residual Stresses by the Hole-Drilling Strain-Gage Method*. 2013.

[4] ALBERTAZZI, A.; VIOTTI, M. R.; BUSCHINELLI, P.; HOFFMANN, A.; KAPP, W. Residual stresses measurement and inner geometry inspection of pipelines by optical methods. In: PROULX, T. (Ed.). *Engineering Applications of Residual Stress, Volume 8*. : Springer New York, 2011. p. 1–12.

[5] NELSON, D. V. Optical methods. In: *Practical Residual Stress Measurement Method*. : Wiley, 2013. Chap. 11, p. 279–302.

[6] VIOTTI, M. R.; ALBERTAZZI, A. *Robust Speckle Metrology Techniques for Stress Analysis and NDT*. : SPIE, 2014.

[7] BLÖDORN, R. *Estudo do Furo e do Processo de Furação Empregado no Méodo do Furo Cego para Medição de Tensões Residuais*. Thesis (Master's) — Universidade Federal de Santa Catarina, 2014.

[8] SCHAJER, G. S.; RUUD, C. O. Overview of residual stresses and their measurement. In: *Practical Residual Stress Measurement Method*. : Wiley, 2013. Chap. 1, p. 1–27.

[9] MAKINO, A.; NELSON, D.; HILL, M. Hole-within-a-hole method for determining residual stresses. *Journal of Engineering Materials and Technology*, v. 133, n. 2, p. 0210201–0210208, 2011.

[10] ROSSINI, N.; DASSISTI, M.; BENYOUNIS, K.; OLABI, A. Methods of measuring residual stresses in components. *Materials & Design*, v. 35, p. 572–588, 2012.

[11] TEBEDGE, N.; ALPSTEN, G.; TALL, L. Residual-stress measurement by the sectioning method. *Experimental Mechanics*, v. 13, n. 2, p. 88–96, 1973.

[12] SCHAJER, G. S.; FLAMAN, M. T.; ROY, G.; LU, J. Hole-drilling and ring core methods. In: *Handbook of Measurement of Residual Stresses*. : Fairmont Press, 1996. Chap. 2, p. 5–34.

[13] MATHAR, J. Determination of initial stresses by measuring the deformation around drilled holes. *Trans. ASME*, v. 56, n. 4, p. 249–254, 1934.

[14] GRANT, P. V.; LORD, J.; WHITEHEAD, P. *Measurement Good Practice Guide No. 53 - Issue 2: The Measurement of Residual Stresses by the Incremental Hole Drilling Technique*. 2006.

[15] NIKU-LARI, a.; LU, J.; FLAVENOT, J. F. Measurement of residual-stress distribution by the incremental hole-drilling method. *Experimental Mechanics*, v. 25, p. 175–185, 1985.

[16] BEGHINI, M.; BERTINI, L.; SANTUS, C. A procedure for evaluating high residual stresses using the blind hole drilling method, including the effect of plasticity. *Journal of Strain Analysis for Engineering Design*, v. 45, n. 4, p. 301–318, 2010. Cited By 12.

[17] ALBERTAZZI, A. *Fundamentals of Interferometry - Speckle*. 2014. PowerPoint Presentation. 83 slides.

[18] MAKINO, a.; NELSON, D. Residual-stress determination by single-axis holographic interferometry and hole drilling-Part I: Theory. *Experimental Mechanics*, v. 34, p. 66–78, 1994.

[19] SUTERIO, R. *Medição de tensões residuais por indentação associada a holografia eletrônica*. Dissertation (PhD) — Universidade Federal de Santa Catarina, 2005.

[20] VISHAY MEASUREMENTS GROUP. *Measurement of Residual Stresses by the Hole Drilling Strain Gage Method*. Tech note 503-6. Raleigh, 2010.

[21] RODACOSKI, M. R. *Medição de tensões residuais com holografia eletrônica*. Dissertation (PhD) — Universidade Federal de Santa Catarina, 1997.

[22] DAVIM, J. P. *Modern Machining Technology: A Practical Guide*. : Woodhead Publishing, 2011. 412 p.

[23] KLOCKE, F. *Manufacturing processes 1: turning, milling, drilling*. : Springer-Verlag Berlin Heidelberg, 2011.

[24] ASTAKHOV, V. P. *Drills: Science and Technology of Advanced Operations*. : CRC Press, 2014. 888 p.

[25] ASTAKHOV, V. P. *Tribology of Metal Cutting*. : Elsevier, 2006. 888 p.

[26] GROTE, K.-H.; ANTONSSON, E. K. *Springer Handbook of Mechanical Engineering*. : Springer Science & Business Media, 2009. 1580 p.

[27] EL-HOFY, H. A.-G. *Fundamentals of Machining Processes: Conventional and Nonconventional Processes*. : CRC Press, 2013. 562 p.

[28] EDWARDS, R. *Cutting Tools*. : Institute of Materials, 1993. 200 p.

[29] SANDVIK. *Metal Cutting Technical Guide: Milling*. 2006.

[30] GARANT TOOLSCOUT. *Machining Handbook*. 2013. 1096 p.

[31] MITSUBISHI CARBIDE. *End Mill Features and Specification*. 2014. Available from Internet: <http://www.mitsubishicarbide.net/contents/mhg/enuk/html/product/technical_information/information/endmill_terminology.html>.

[32] WORMAN, T. *The Skinny on End Mills*. 2015. Available from Internet: <http://makezine.com/magazine/make-40/endmills/>.

[33] ASTAKHOV, V. P.; DAVIM, J. P. Tools (geometry and material) and tool wear. In: DAVIM, J. P. (Ed.). *Machining: Fundamentals and Recent Advances*. : Springer, 2008. Chap. 2, p. 29–57.

[34] WYEN, C.-F. *Rounded cutting edges and their influence in machining titanium*. Dissertation (PhD) — Eidgenössische Technische Hochschule ETH Zürich, 2011.

[35] TOENSHOFF, H. K.; DENKENA, B. *Basics of Cutting and Abrasive Processes*. : Springer-Verlag Berlin Heidelberg, 2013. 21–37 p.

[36] BISSACCO, G.; HANSEN, H. N.; De Chiffre, L. Micromilling of hardened tool steel for mould making applications. *Journal of Materials Processing Technology*, v. 167, n. 2-3, p. 201–207, 2005.

[37] DORNFELD, D.; MIN, S.; TAKEUCHI, Y. Recent Advances in Mechanical Micromachining. *CIRP Annals - Manufacturing Technology*, v. 55, n. 2, p. 745–768, 2006.

[38] CHAE, J.; PARK, S. S.; FREIHEIT, T. Investigation of micro-cutting operations. *International Journal of Machine Tools and Manufacture*, v. 46, n. 3-4, p. 313–332, 2006.

[39] ARAMCHAROEN, a.; MATIVENGA, P. T. Size effect and tool geometry in micromilling of tool steel. *Precision Engineering*, v. 33, n. 4, p. 402–407, 2009.

[40] LAI, X.; LI, H.; LI, C.; LIN, Z.; NI, J. Modelling and analysis of micro scale milling considering size effect, micro cutter edge radius and minimum chip thickness. *International Journal of Machine Tools and Manufacture*, v. 48, n. 1, p. 1–14, 2008.

[41] OLIVEIRA, F. B. de; RODRIGUES, A. R.; COELHO, R. T.; SOUZA, A. F. de. Size effect and minimum chip thickness in micromilling. *International Journal of Machine Tools and Manufacture*, v. 89, p. 39–54, 2015.

[42] BLÖDORN, R.; TAMURA, M. T.; HENKE, R. A.; VIOTTI, M. R.; JR, A. A.; SCHROETER, R. B. Study of the drilling process used in the hole-drilling method through thrust force measurement and tool wear analysis. In: *23rd ABCM International Congress of Mechanical Engineering*. Rio de Janeiro: , 2015. p. 1–8.

[43] KIM, C.-J.; BONO, M.; NI, J. Experimental analysis of chip formation in micro-milling. In: ENGINEERS, S. of M. (Ed.). *NAMRI XXX*. 2002. p. 1–8.

[44] SCHOLTES, B. Residual Stress Introduced by Machining. In: NIKU-LARI, A. (Ed.). *Advances in surface treatments: technology - applications - effects*. : Pergamon Books, 1987. p. 59–71.

[45] TRENT, E. M.; WRIGHT, P. K. *Metal Cutting*. 4. ed. : Butterworth-Heinemann, 2000.

[46] WANG, S.; TO, S.; CHAN, C.; CHEUNG, C.; LEE, W. A study of the cutting-induced heating effect on the machined surface in ultra-precision raster milling of 6061 al alloy. *The International Journal of Advanced Manufacturing Technology*, Springer-Verlag, v. 51, n. 1-4, p. 69–78, 2010.

[47] SADAT, A. B. Surface region damage of machined inconel-718 nickel-base superalloy using natural and controlled contact length tools. *Wear*, v. 119, n. 2, p. 225 – 235, 1987.

[48] BRINKSMEIER, E.; CAMMETT, J.; KONIG, W.; LESKOVAR, P.; PETERS, J.; TONSHOFF, H. Residual stresses: Measurement and causes in machining processes. *CIRP Annals*, v. 31, n. 2, p. 491 – 510, 1982.

[49] JANG, D.; WATKINS, T.; KOZACZEK, K.; HUBBARD, C.; CAVIN, O. Surface residual stresses in machined austenitic stainless steel. *Wear*, v. 194, n. 1–2, p. 168 – 173, 1996.

[50] EL-KHABEERY, M.; FATTOUH, M. Residual stress distribution caused by milling. *International Journal of Machine Tools and Manufacture*, v. 29, n. 3, p. 391 – 401, 1989.

[51] FLAMAN, M. Brief investigation of induced drilling stresses in the center-hole method of residual-stress measurement. *Experimental Mechanics*, Kluwer Academic Publishers, v. 22, n. 1, p. 26–30, 1982.

[52] FLAMAN, M. T.; HERRING, J. A. Comparison of four hole-producing techniques for the center-hole residual-stress measurement method. *Experimental Techniques*, v. 9, n. 8, p. 30–32, 1985.

[53] STEINZIG, M.; UPSHAW, D.; RASTY, J. Influence of drilling parameters on the accuracy of hole-drilling residual stress measurements. *Experimental Mechanics*, v. 54, p. 1537–1543, 2014.

[54] MITSUBISHI CARBIDE. *Tools News – B052G – Micro Solid Carbide Drills*. 2015. Available from Internet: <https://www.mitsubishicarbide.com/mmc/en/product/pdf/b/b052g.pdf>.

[55] KYOCERA PRECISION TOOLS. *Drillling Speeds & Feeds – Micro Drills*. 2015. Available from Internet: <http://www.kyoceraprecisiontools.com/micro/pdf/257_MIT_Catalog.pdf>.

[56] CALLISTER, W. D.; RETHWISCH, D. G. *Materials Science and Engineering: An Introduction*. : John Wiley & Sons, 2010. 992 p.

[57] GROOVER, M. *Fundamentals of Modern Manufacturing: Materials, Processes, and Systems*. : John Wiley & Sons, 2010.

[58] DAVIS, J. R. *ASM Handbook Volume 16: Machining*. 9th. ed. : ASM International, 1989. 944 p.

[59] SANDVIK. *Machining Stainless Steels*. 2015. Available from Internet: <http://smt.sandvik.com/en/products/bar-and-hollow-bar/bar-steel/machining-stainless-steels/>.

[60] ASM INTERNATIONAL. *ASM Handbook Volume 01 – Properties and Selection: Irons, Steels, and High-Performance Alloys*. 1991. v. 1. 2521 p.

[61] KÖNIG, W.; KLOCKE, F. *Tecnologia da Usinagem com Ferramenta de Corte de Geometria Definida - Parte 1*. : Springer, 2002.

[62] DAVIM, J. P. *Machining: Fundamentals and Recent Advances*. : Springer-Verlag London, 2008.

[63] KLOCKE, F.; EISENBLÄTTER, G. Dry cutting. *CIRP Annals - Manufacturing Technology*, v. 46, n. 2, p. 519 – 526, 1997.

[64] SMITH, I.; MUNZ, W.; DONOHUE, L.; PETROV, I.; GREENE, J. Improved ti1-xalxn pvd coatings for dry high speed cutting operations. *Surface Engineering*, v. 14, n. 1, p. 37–41, 1998. Cited By 27.

[65] VIOTTI, M. R.; ALBERTAZZI, A. Robust speckle metrology for stress measurements outside the lab. In: LEHMANN, P. (Ed.). *Optical Measurement Systems for Industrial Inspection IX – Proceedings of SPIE*. 2015. v. 9525.

[66] GEELS, K.; KOPP, W.; RüCKERT, M. *Metallographic and materialographic specimen preparation, light microscopy, image analysis, and hardness testing*. West Conshohocken, PA: ASTM International, 2007.

[67] ASM INTERNATIONAL. *ASM Handbook Volume 9 – Metallography and Microstructures* . 2004. v. 9. 1184 p.

[68] INTERNATIONAL ORGANIZATION FOR STANDARDIZATION. *ISO 6507-1:2005 – Metallic materials – Vickers hardness test – Part 1: Test method*. Geneva, Switzerland: , 2005.

[69] JEOL Ltd. *Scanning Electron Microscope A To Z*. Tokyo, Japan., 2009.

[70] SIMONEAU, a.; NG, E.; ELBESTAWI, M. a. Chip formation during microscale cutting of a medium carbon steel. *International Journal of Machine Tools and Manufacture*, v. 46, n. 5, p. 467–481, 2006.

[71] LANTRIP, J.; NEE, J. G.; SMITH, D. A. *Fundamentals of Tool Design*. 5th. ed. : Society of Manufacturing Engineers, 2003. 404 p.

[72] ENDRES, W. J.; KOUNTANYA, R. K. The Effects of Corner Radius and Edge Radius on Tool Flank Wear. *Journal of Manufacturing Processes*, v. 4, n. 2, p. 89–96, 2002.

[73] CAPELLO, E. Residual stresses in turning: Part I: Influence of process parameters. *Journal of Materials Processing Technology*, v. 160, p. 221–228, 2005.

[74] CAPELLO, E. Residual stresses in turning: Part II. Influence of the machined material. *Journal of Materials Processing Technology*, v. 172, p. 319–326, 2006.

[75] TANG, Z. T.; LIU, Z. Q.; PAN, Y. Z.; WAN, Y.; AI, X. The influence of tool flank wear on residual stresses induced by milling aluminum alloy. *Journal of Materials Processing Technology*, v. 209, p. 4502–4508, 2009.

[76] MINITOR CO. *Sfida 01 Series – Motor Spindle MZ01: Operation Manual*. Japan.

APPENDIX A – CUTTING TOOL MEASUREMENT

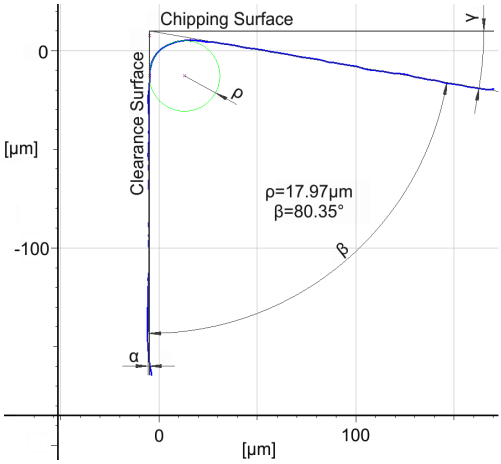

(a) Minor cutting edge.

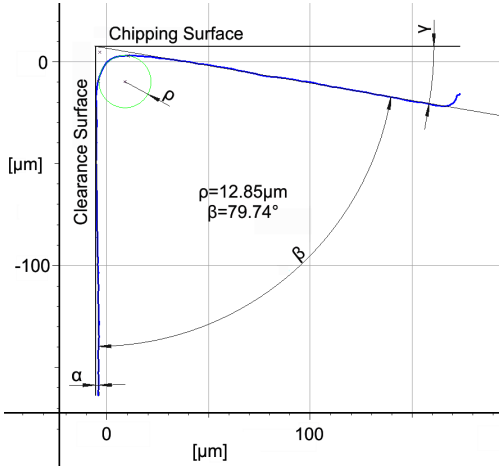

(b) Major cutting edge.

Two-flute square end mill microgeometry measurement samples.

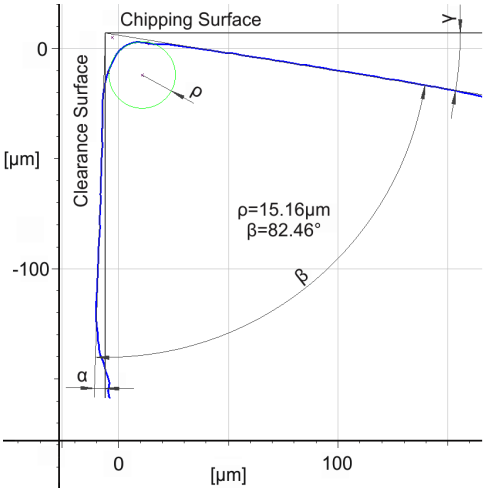

(a) Minor cutting edge.

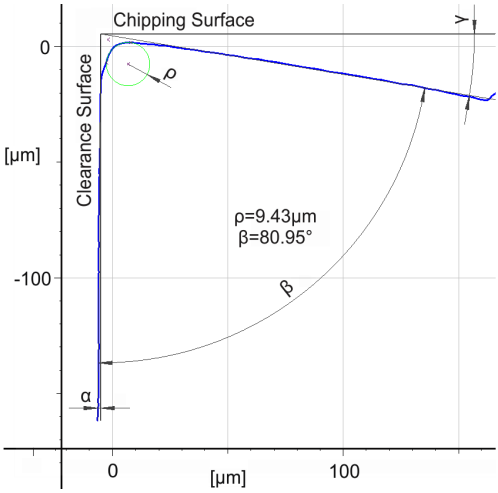

(b) Major cutting edge.

Four-flute square end mill microgeometry measurement samples.

APPENDIX B – RESIDUAL STRESSES MEASUREMENTS RAW DATA

Table B.1 – Residual stress raw data for stainless steel AISI 304L.

Test [-]	$\mathbf{n_f}$ [-]	$\mathbf{v_f}$ [mm/min]	**n** [$\times 10^3$ rpm]	$\mathbf{f_z}$ [μm]	σ_1 [MPa]	σ_2 [MPa]
a11	2	10	25	0.20	-66	-81
a12	2	10	25	0.20	-57	-66
b11	2	10	40	0.13	-88	-97
c11	2	20	25	0.40	-38	-44
c12	2	20	25	0.40	-43	-63
d11	2	20	40	0.25	-51	-95
d12	2	20	40	0.25	-39	-57
A22	4	10	25	0.10	-7	-13
A23	4	10	25	0.10	14	-1
B21	4	10	40	0.06	-15	-29
C81	4	20	25	0.20	-94	-125
C82	4	20	25	0.20	-84	-113
D81	4	20	40	0.13	-111	-118
D82	4	20	40	0.13	-87	-100

Table B.2 – Residual stress raw data for carbon steel AISI 1020.

Test [-]	$\mathbf{n_f}$ [-]	$\mathbf{v_f}$ [mm/min]	**n** [$\times 10^3$ rpm]	$\mathbf{f_z}$ [μm]	σ_1 [MPa]	σ_2 [MPa]
a31	2	10	25	0.20	-17	-20
a32	2	10	25	0.20	-16	-20
a33	2	10	25	0.20	-12	-15
b31	2	10	40	0.13	10	6
b32	2	10	40	0.13	-15	-17
b33	2	10	40	0.13	16	-5
c31	2	20	25	0.40	50	30
c32	2	20	25	0.40	48	27
c33	2	20	25	0.40	58	32
d31	2	20	40	0.25	-16	-20
d32	2	20	40	0.25	-16	-17
d33	2	20	40	0.25	-39	-59
A31	4	10	25	0.10	-5	-6
A32	4	10	25	0.10	-2	-7
A33	4	10	25	0.10	26	5
B31	4	10	40	0.06	19	1
B32	4	10	40	0.06	13	-10
B33	4	10	40	0.06	15	-3
C31	4	20	25	0.20	16	-3
C32	4	20	25	0.20	18	-3
C33	4	20	25	0.20	15	-2
D31	4	20	40	0.13	20	-3
D32	4	20	40	0.13	16	-2
D33	4	20	40	0.13	16	-2

Table B.3 – Residual stress raw data for aluminium alloy AA 6061.

Test [-]	$\mathbf{n_f}$ [-]	$\mathbf{v_f}$ [mm/min]	**n** [$\times 10^3$ rpm]	$\mathbf{f_z}$ [μm]	σ_1 [MPa]	σ_2 [MPa]
a51	2	10	25	0.20	11	6
a52	2	10	25	0.20	17	12
a53	2	10	25	0.20	25	12
b51	2	10	40	0.13	46	26
b52	2	10	40	0.13	14	11
b53	2	10	40	0.13	14	11
c51	2	20	25	0.40	25	20
c52	2	20	25	0.40	24	20
c53	2	20	25	0.40	30	26
d51	2	20	40	0.25	23	18
d52	2	20	40	0.25	49	30
d53	2	20	40	0.25	23	17
A51	4	10	25	0.10	17	3
A52	4	10	25	0.10	25	13
A53	4	10	25	0.10	35	17
B51	4	10	40	0.06	25	15
B52	4	10	40	0.06	17	13
B53	4	10	40	0.06	14	12
C51	4	20	25	0.20	10	7
C52	4	20	25	0.20	12	5
C53	4	20	25	0.20	14	7
D52	4	20	40	0.13	10	5
D53	4	20	40	0.13	8	2
D54	4	20	40	0.13	6	3

APPENDIX C – ANALYSES OF VARIANCE – MICROHARDNESS

Table C.1 – Analysis of the drilling effect on the AISI 304L samples hole bottom microhardness using a two-flute square end mill.

(a) Groups statistics

Sample	Sample size		Sample mean		Sample variance	
Base material	$\mathbf{n_0}$	24	μ_0	175.3	$\mathbf{S_0}$	3.7
$v_f = 10$ mm/min $n = 25,000$ rpm	$\mathbf{n_a}$	5	μ_a	180.0	$\mathbf{S_a}$	4.7
$v_f = 10$ mm/min $n = 40,000$ rpm	$\mathbf{n_b}$	5	μ_b	184.8	$\mathbf{S_b}$	2.3
$v_f = 20$ mm/min $n = 25,000$ rpm	$\mathbf{n_c}$	5	μ_c	182.4	$\mathbf{S_c}$	4.7
$v_f = 20$ mm/min $n = 40,000$ rpm	$\mathbf{n_d}$	5	μ_d	178.0	$\mathbf{S_d}$	4.7

(b) Unequal variance t-test

Hypotheses	df	t_0	t_{crit}	P-value	MD	Test result
$\mathbf{H_0 : \mu_0 - \mu_a = 0}$ $\mathbf{H_1 : \mu_0 - \mu_a \neq 0}$	5.1	-2.13	2.56	0.085	-4.8	H_0 cannot be rejected
$\mathbf{H_0 : \mu_0 - \mu_b = 0}$ $\mathbf{H_1 : \mu_0 - \mu_b \neq 0}$	9.1	-7.53	2.26	<0.001	-9.6	H_0 can be rejected
$\mathbf{H_0 : \mu_0 - \mu_c = 0}$ $\mathbf{H_1 : \mu_0 - \mu_c \neq 0}$	5.1	-3.19	2.56	0.024	-7.2	H_0 can be rejected
$\mathbf{H_0 : \mu_0 - \mu_d = 0}$ $\mathbf{H_1 : \mu_0 - \mu_d \neq 0}$	5.1	-1.23	2.56	0.271	-2.8	H_0 cannot be rejected

$\alpha = 0.05$; MD: mean difference; df: degrees of freedom.

Table C.2 – Analysis of the drilling effect on the AISI 304L samples hole wall microhardness using a two-flute square end mill.

(a) Groups statistics

Sample	Sample size		Sample mean		Sample variance	
Base material	$\mathbf{n_0}$	24	μ_0	175.3	$\mathbf{S_0}$	3.7
$v_f = 10$ mm/min $n = 25,000$ rpm	$\mathbf{n_a}$	6	μ_a	180.5	$\mathbf{S_a}$	4.2
$v_f = 10$ mm/min $n = 40,000$ rpm	$\mathbf{n_b}$	6	μ_b	178.7	$\mathbf{S_b}$	3.1
$v_f = 20$ mm/min $n = 25,000$ rpm	$\mathbf{n_c}$	6	μ_c	182.5	$\mathbf{S_c}$	5.4
$v_f = 20$ mm/min $n = 40,000$ rpm	$\mathbf{n_d}$	6	μ_d	181.0	$\mathbf{S_d}$	4.3

(b) Unequal variance t-test

Hypotheses	df	t_0	t_{crit}	P-value	MD	Test result
$\mathbf{H_0 : \mu_0 - \mu_a = 0}$ $\mathbf{H_1 : \mu_0 - \mu_a \neq 0}$	7.0	-2.79	2.36	0.027	-5.3	H_0 can be rejected
$\mathbf{H_0 : \mu_0 - \mu_b = 0}$ $\mathbf{H_1 : \mu_0 - \mu_b \neq 0}$	9.0	-2.33	2.26	0.045	-3.4	H_0 can be rejected
$\mathbf{H_0 : \mu_0 - \mu_c = 0}$ $\mathbf{H_1 : \mu_0 - \mu_c \neq 0}$	6.2	-3.11	2.43	0.020	-7.3	H_0 can be rejected
$\mathbf{H_0 : \mu_0 - \mu_d = 0}$ $\mathbf{H_1 : \mu_0 - \mu_d \neq 0}$	6.9	-2.99	2.37	0.021	-5.8	H_0 can be rejected

$\alpha = 0.05$; MD: mean difference; df: degrees of freedom.

Table C.3 – Analysis of the drilling effect on the AISI 304L samples hole bottom microhardness using a four-flute square end mill.

(a) Groups statistics

Sample	**Sample size**		**Sample mean**		**Sample variance**	
Base material	$\mathbf{n_0}$	24	μ_0	175.3	$\mathbf{S_0}$	3.7
$v_f = 10$ mm/min $n = 25,000$ rpm	$\mathbf{n_A}$	5	μ_A	172.4	$\mathbf{S_A}$	2.6
$v_f = 10$ mm/min$n =$ 40,000 rpm	$\mathbf{n_B}$	5	μ_B	186.4	$\mathbf{S_B}$	6.1
$v_f = 20$ mm/min $n = 25,000$ rpm	$\mathbf{n_C}$	5	μ_C	168.2	$\mathbf{S_C}$	4.0
$v_f = 20$ mm/min $n = 40,000$ rpm	$\mathbf{n_D}$	5	μ_D	182.0	$\mathbf{S_D}$	3.5

(b) Unequal variance t-test

Hypotheses	**df**	$\mathbf{t_0}$	$\mathbf{t_{crit}}$	**P-value**	**MD**	**Test result**
$\mathbf{H_0 : \mu_0 - \mu_A = 0}$ $\mathbf{H_1 : \mu_0 - \mu_A \neq 0}$	7.8	2.05	2.32	0.075	2.8	H_0 cannot be rejected
$\mathbf{H_0 : \mu_0 - \mu_B = 0}$ $\mathbf{H_1 : \mu_0 - \mu_B \neq 0}$	4.6	-3.96	2.63	0.012	-11	H_0 can be rejected
$\mathbf{H_0 : \mu_0 - \mu_C = 0}$ $\mathbf{H_1 : \mu_0 - \mu_C \neq 0}$	5.5	3.61	2.50	0.013	7.1	H_0 can be rejected
$\mathbf{H_0 : \mu_0 - \mu_D = 0}$ $\mathbf{H_1 : \mu_0 - \mu_D \neq 0}$	6.0	-3.85	2.45	0.008	-6.8	H_0 can be rejected

$\alpha = 0.05$; MD: mean difference; df: degrees of freedom.

Table C.4 – Analysis of the drilling effect on the AISI 304L samples hole wall microhardness using a four-flute square end mill.

(a) Groups statistics

Sample	Sample size		Sample mean		Sample variance	
Base material	$\mathbf{n_0}$	24	μ_0	175.3	$\mathbf{S_0}$	3.7
$v_f = 10$ mm/min $n = 25,000$ rpm	$\mathbf{n_A}$	6	μ_A	176.5	$\mathbf{S_A}$	4.6
$v_f = 10$ mm/min $n = 40,000$ rpm	$\mathbf{n_B}$	6	μ_B	179.2	$\mathbf{S_B}$	3.5
$v_f = 20$ mm/min $n = 25,000$ rpm	$\mathbf{n_C}$	6	μ_C	173.2	$\mathbf{S_C}$	5.6
$v_f = 20$ mm/min $n = 40,000$ rpm	$\mathbf{n_D}$	6	μ_D	180.3	$\mathbf{S_D}$	2.9

(b) Unequal variance t-test

Hypotheses	df	t_0	t_{crit}	P-value	MD	Test result
$\mathbf{H_0 : \mu_0 - \mu_A = 0}$ $\mathbf{H_1 : \mu_0 - \mu_A \neq 0}$	6.7	-0.62	2.39	0.557	-1.3	H_0 cannot be rejected
$\mathbf{H_0 : \mu_0 - \mu_B = 0}$ $\mathbf{H_1 : \mu_0 - \mu_B \neq 0}$	8.1	-2.43	2.30	0.041	-3.9	H_0 can be rejected
$\mathbf{H_0 : \mu_0 - \mu_C = 0}$ $\mathbf{H_1 : \mu_0 - \mu_C \neq 0}$	6.1	0.86	2.44	0.422	2.1	H_0 cannot be rejected
$\mathbf{H_0 : \mu_0 - \mu_D = 0}$ $\mathbf{H_1 : \mu_0 - \mu_D \neq 0}$	9.4	-3.58	2.25	0.006	-5.1	H_0 can be rejected

$\alpha = 0.05$; MD: mean difference; df: degrees of freedom.

Table C.5 – Analysis of the drilling effect on the AISI 1020 samples hole bottom microhardness using a two-flute square end mill.

(a) Groups statistics

Sample	**Sample size**		**Sample mean**		**Sample variance**	
Base material	$\mathbf{n_0}$	24	μ_0	151.2	$\mathbf{S_0}$	1.8
$v_f = 10$ mm/min $n = 25{,}000$ rpm	$\mathbf{n_a}$	5	μ_a	150.8	$\mathbf{S_a}$	2.0
$v_f = 10$ mm/min $n = 40{,}000$ rpm	$\mathbf{n_b}$	5	μ_b	153.6	$\mathbf{S_b}$	0.9
$v_f = 20$ mm/min $n = 25{,}000$ rpm	$\mathbf{n_c}$	5	μ_c	152.0	$\mathbf{S_c}$	2.3
$v_f = 20$ mm/min $n = 40{,}000$ rpm	$\mathbf{n_d}$	5	μ_d	152.2	$\mathbf{S_d}$	1.3

(b) Unequal variance t-test

Hypotheses	**df**	$\mathbf{t_0}$	$\mathbf{t_{crit}}$	**P-value**	**MD**	**Test result**
$\mathbf{H_0 : \mu_0 - \mu_a = 0}$ $\mathbf{H_1 : \mu_0 - \mu_a \neq 0}$	5.3	0.41	2.53	0.695	0.4	H_0 cannot be rejected
$\mathbf{H_0 : \mu_0 - \mu_b = 0}$ $\mathbf{H_1 : \mu_0 - \mu_b \neq 0}$	11.8	-4.44	2.18	0.001	-2.4	H_0 can be rejected
$\mathbf{H_0 : \mu_0 - \mu_c = 0}$ $\mathbf{H_1 : \mu_0 - \mu_c \neq 0}$	5.0	-0.71	2.57	0.507	-0.8	H_0 cannot be rejected
$\mathbf{H_0 : \mu_0 - \mu_d = 0}$ $\mathbf{H_1 : \mu_0 - \mu_d \neq 0}$	7.5	-1.45	2.34	0.189	-1.0	H_0 cannot be rejected

$\alpha = 0.05$; MD: mean difference; df: degrees of freedom.

Table C.6 – Analysis of the drilling effect on the AISI 1020 samples hole wall microhardness using a two-flute square end mill.

(a) Groups statistics

Sample	Sample size		Sample mean		Sample variance	
Base material	$\mathbf{n_0}$	24	μ_0	151.2	$\mathbf{S_0}$	1.8
$v_f = 10$ mm/min $n = 25,000$ rpm	$\mathbf{n_a}$	6	μ_a	156.8	$\mathbf{S_a}$	1.5
$v_f = 10$ mm/min $n = 40,000$ rpm	$\mathbf{n_b}$	6	μ_b	155.7	$\mathbf{S_b}$	2.1
$v_f = 20$ mm/min $n = 25,000$ rpm	$\mathbf{n_c}$	6	μ_c	153.7	$\mathbf{S_c}$	2.0
$v_f = 20$ mm/min $n = 40,000$ rpm	$\mathbf{n_d}$	6	μ_d	153.0	$\mathbf{S_d}$	1.4

(b) Unequal variance t-test

Hypotheses	df	t_0	t_{crit}	P-value	MD	Test result
$\mathbf{H_0 : \mu_0 - \mu_a = 0}$ $\mathbf{H_1 : \mu_0 - \mu_a \neq 0}$	9.0	-8.02	2.26	<0.001	-5.6	H_0 can be rejected
$\mathbf{H_0 : \mu_0 - \mu_b = 0}$ $\mathbf{H_1 : \mu_0 - \mu_b \neq 0}$	7.0	-4.86	2.37	0.002	-4.5	H_0 can be rejected
$\mathbf{H_0 : \mu_0 - \mu_c = 0}$ $\mathbf{H_1 : \mu_0 - \mu_c \neq 0}$	7.2	-2.79	2.35	0.026	-2.5	H_0 can be rejected
$\mathbf{H_0 : \mu_0 - \mu_d = 0}$ $\mathbf{H_1 : \mu_0 - \mu_d \neq 0}$	9.4	-2.63	2.25	0.026	-1.8	H_0 can be rejected

$\alpha = 0.05$; MD: mean difference; df: degrees of freedom.

Table C.7 – Analysis of the drilling effect on the AISI 1020 samples hole bottom microhardness using a four-flute square end mill.

(a) Groups statistics

Sample	**Sample size**		**Sample mean**		**Sample variance**	
Base material	$\mathbf{n_0}$	24	μ_0	151.2	$\mathbf{S_0}$	1.8
$v_f = 10$ mm/min $n = 25{,}000$ rpm	$\mathbf{n_A}$	5	μ_A	151.6	$\mathbf{S_A}$	2.7
$v_f = 10$ mm/min $n = 40{,}000$ rpm	$\mathbf{n_B}$	5	μ_B	153.8	$\mathbf{S_B}$	2.3
$v_f = 20$ mm/min $n = 25{,}000$ rpm	$\mathbf{n_C}$	5	μ_C	149.2	$\mathbf{S_C}$	1.6
$v_f = 20$ mm/min $n = 40{,}000$ rpm	$\mathbf{n_D}$	5	μ_D	151.4	$\mathbf{S_D}$	2.5

(b) Unequal variance t-test

Hypotheses	**df**	$\mathbf{t_0}$	$\mathbf{t_{crit}}$	**P-value**	**MD**	**Test result**
$\mathbf{H_0}: \mu_0 - \mu_A = 0$ $\mathbf{H_1}: \mu_0 - \mu_A \neq 0$	4.7	-0.31	2.61	0.769	-0.4	H_0 cannot be rejected
$\mathbf{H_0}: \mu_0 - \mu_B = 0$ $\mathbf{H_1}: \mu_0 - \mu_B \neq 0$	5.1	-2.40	2.56	0.061	-2.6	H_0 cannot be rejected
$\mathbf{H_0}: \mu_0 - \mu_C = 0$ $\mathbf{H_1}: \mu_0 - \mu_C \neq 0$	6.1	2.45	2.44	0.049	2.0	H_0 can be rejected
$\mathbf{H_0}: \mu_0 - \mu_D = 0$ $\mathbf{H_1}: \mu_0 - \mu_D \neq 0$	4.9	-0.16	2.59	0.877	-0.2	H_0 cannot be rejected

$\alpha = 0.05$; MD: mean difference; df: degrees of freedom.

Table C.8 – Analysis of the drilling effect on the AISI 1020 samples hole wall microhardness using a four-flute square end mill.

(a) Groups statistics

Sample	Sample size		Sample mean		Sample variance	
Base material	$\mathbf{n_0}$	24	μ_0	151.2	$\mathbf{S_0}$	1.8
$v_f = 10$ mm/min $n = 25,000$ rpm	$\mathbf{n_A}$	6	μ_A	149.3	$\mathbf{S_A}$	2.0
$v_f = 10$ mm/min $n = 40,000$ rpm	$\mathbf{n_B}$	6	μ_B	154.5	$\mathbf{S_B}$	2.3
$v_f = 20$ mm/min $n = 25,000$ rpm	$\mathbf{n_C}$	6	μ_C	152.3	$\mathbf{S_C}$	2.3
$v_f = 20$ mm/min $n = 40,000$ rpm	$\mathbf{n_D}$	6	μ_D	152.3	$\mathbf{S_D}$	2.3

(b) Unequal variance t-test

Hypotheses	df	t_0	t_{crit}	P-value	MD	Test result
$\mathbf{H_0 : \mu_0 - \mu_A = 0}$ $\mathbf{H_1 : \mu_0 - \mu_A \neq 0}$	7.2	2.13	2.35	0.070	1.9	H_0 cannot be rejected
$\mathbf{H_0 : \mu_0 - \mu_B = 0}$ $\mathbf{H_1 : \mu_0 - \mu_B \neq 0}$	6.6	-3.32	2.39	0.014	-3.3	H_0 can be rejected
$\mathbf{H_0 : \mu_0 - \mu_C = 0}$ $\mathbf{H_1 : \mu_0 - \mu_C \neq 0}$	6.6	-1.14	2.39	0.294	-1.1	H_0 cannot be rejected
$\mathbf{H_0 : \mu_0 - \mu_D = 0}$ $\mathbf{H_1 : \mu_0 - \mu_D \neq 0}$	6.5	-1.10	2.40	0.309	-1.1	H_0 cannot be rejected

$\alpha = 0.05$; MD: mean difference; df: degrees of freedom.

Table C.9 – Analysis of the drilling effect on the AA 6061 samples hole bottom microhardness using a two-flute square end mill.

(a) Groups statistics

Sample	Sample size		Sample mean		Sample variance	
Base material Workpiece No. 0	$\mathbf{n_0}$	12	μ_0	57.0	$\mathbf{S_0}$	2.1
$v_f = 10$ mm/min $n = 25,000$ rpm	$\mathbf{n_a}$	3	μ_a	58.9	$\mathbf{S_a}$	0.6
$v_f = 10$ mm/min $n = 40,000$ rpm	$\mathbf{n_b}$	3	μ_b	60.2	$\mathbf{S_b}$	0.9
Base material Workpiece No. 1	$\mathbf{n_1}$	12	μ_1	46.3	$\mathbf{S_1}$	1.5
$v_f = 20$ mm/min $n = 25,000$ rpm	$\mathbf{n_c}$	3	μ_c	46.5	$\mathbf{S_c}$	2.3
$v_f = 20$ mm/min $n = 40,000$ rpm	$\mathbf{n_d}$	3	μ_d	47.3	$\mathbf{S_d}$	2.7

(b) Unequal variance t-test

Hypotheses	df	t_0	t_{crit}	P-value	MD	Test result
$\mathbf{H_0 : \mu_0 - \mu_a = 0}$ $\mathbf{H_1 : \mu_0 - \mu_a \neq 0}$	12	-2.70	2.17	0.018	-1.9	H_0 can be rejected
$\mathbf{H_0 : \mu_0 - \mu_b = 0}$ $\mathbf{H_1 : \mu_0 - \mu_b \neq 0}$	5.7	-3.41	2.48	0.016	-3.2	H_0 can be rejected
$\mathbf{H_0 : \mu_0 - \mu_c = 0}$ $\mathbf{H_1 : \mu_0 - \mu_c \neq 0}$	2.5	-0.15	3.61	0.895	-0.2	H_0 cannot be rejected
$\mathbf{H_0 : \mu_0 - \mu_d = 0}$ $\mathbf{H_1 : \mu_0 - \mu_d \neq 0}$	2.3	-0.62	3.78	0.590	-1.0	H_0 cannot be rejected

$\alpha = 0.05$; MD: mean difference; df: degrees of freedom.

Table C.10 – Analysis of the drilling effect on the AA 6061 samples hole wall microhardness using a two-flute square end mill.

(a) Groups statistics

Sample	Sample size		Sample mean		Sample variance	
Base material Workpiece No. 0	$\mathbf{n_0}$	12	μ_0	57.0	$\mathbf{S_0}$	2.1
$v_f = 10$ mm/min $n = 25,000$ rpm	$\mathbf{n_a}$	4	μ_a	56.8	$\mathbf{S_a}$	1.1
$v_f = 10$ mm/min $n = 40,000$ rpm	$\mathbf{n_b}$	4	μ_b	58.6	$\mathbf{S_b}$	1.3
Base material Workpiece No. 1	$\mathbf{n_1}$	12	μ_1	46.3	$\mathbf{S_1}$	1.5
$v_f = 20$ mm/min $n = 25,000$ rpm	$\mathbf{n_c}$	4	μ_c	45.7	$\mathbf{S_c}$	0.7
$v_f = 20$ mm/min $n = 40,000$ rpm	$\mathbf{n_d}$	4	μ_d	46.3	$\mathbf{S_d}$	0.9

(b) Unequal variance t-test

Hypotheses	df	t_0	t_{crit}	P-value	MD	Test result
$\mathbf{H_0 : \mu_0 - \mu_a = 0}$ $\mathbf{H_1 : \mu_0 - \mu_a \neq 0}$	11	0.31	2.20	0.764	0.25	H_0 cannot be rejected
$\mathbf{H_0 : \mu_0 - \mu_b = 0}$ $\mathbf{H_1 : \mu_0 - \mu_b \neq 0}$	8.6	-1.68	2.28	0.128	-1.5	H_0 cannot be rejected
$\mathbf{H_0 : \mu_1 - \mu_c = 0}$ $\mathbf{H_1 : \mu_1 - \mu_c \neq 0}$	12	1.19	2.17	0.256	0.65	H_0 cannot be rejected
$\mathbf{H_0 : \mu_1 - \mu_d = 0}$ $\mathbf{H_1 : \mu_1 - \mu_d \neq 0}$	8.7	-0.04	2.27	0.970	-0.025	H_0 cannot be rejected

$\alpha = 0.05$; MD: mean difference; df: degrees of freedom.

Table C.11 – Analysis of the drilling effect on the AA 6061 samples hole bottom microhardness using a four-flute square end mill.

(a) Groups statistics

Sample	Sample size		Sample mean		Sample variance	
Base material Workpiece #0	$\mathbf{n_0}$	12	μ_0	52.8	$\mathbf{S_0}$	2.9
$v_f = 10$ mm/min $n = 25{,}000$ rpm	$\mathbf{n_A}$	3	μ_A	54.8	$\mathbf{S_A}$	0.4
$v_f = 10$ mm/min $n = 40{,}000$ rpm	$\mathbf{n_B}$	3	μ_B	52.1	$\mathbf{S_B}$	0.7
Base material Workpiece #1	$\mathbf{n_1}$	12	μ_1	45.7	$\mathbf{S_1}$	1.7
$v_f = 20$ mm/min $n = 25{,}000$ rpm	$\mathbf{n_C}$	3	μ_C	44.8	$\mathbf{S_C}$	1.6
$v_f = 20$ mm/min $n = 40{,}000$ rpm	$\mathbf{n_D}$	3	μ_D	47.8	$\mathbf{S_D}$	1.1

(b) Unequal variance t-test

Hypotheses	df	t_0	t_{crit}	P-value	MD	Test result
$\mathbf{H_0 : \mu_0 - \mu_A = 0}$ $\mathbf{H_1 : \mu_0 - \mu_A \neq 0}$	11	-1.97	2.21	0.074	-2.0	H_0 cannot be rejected
$\mathbf{H_0 : \mu_0 - \mu_B = 0}$ $\mathbf{H_1 : \mu_0 - \mu_B \neq 0}$	12	0.74	2.18	0.472	0.7	H_0 cannot be rejected
$\mathbf{H_0 : \mu_1 - \mu_C = 0}$ $\mathbf{H_1 : \mu_1 - \mu_C \neq 0}$	3.4	0.89	2.98	0.431	0.9	H_0 cannot be rejected
$\mathbf{H_0 : \mu_1 - \mu_D = 0}$ $\mathbf{H_1 : \mu_1 - \mu_D \neq 0}$	4.9	-2.64	2.58	0.047	-2.2	H_0 can be rejected

$\alpha = 0.05$; MD: mean difference; df: degrees of freedom.

Table C.12 – Analysis of the drilling effect on the AA 6061 samples hole wall microhardness using a four-flute square end mill.

(a) Groups statistics

Sample	Sample size		Sample mean		Sample variance	
Base material Workpiece No. 0	$\mathbf{n_0}$	12	μ_0	52.8	$\mathbf{S_0}$	2.9
$v_f = 10$ mm/min $n = 25,000$ rpm	$\mathbf{n_A}$	4	μ_A	53.1	$\mathbf{S_A}$	3.6
$v_f = 10$ mm/min $n = 40,000$ rpm	$\mathbf{n_B}$	4	μ_B	53.6	$\mathbf{S_B}$	0.3
Base material Workpiece No. 1	$\mathbf{n_1}$	12	μ_1	45.7	$\mathbf{S_1}$	1.7
$v_f = 20$ mm/min $n = 25,000$ rpm	$\mathbf{n_C}$	4	μ_C	44.9	$\mathbf{S_C}$	0.6
$v_f = 20$ mm/min $n = 40,000$ rpm	$\mathbf{n_D}$	4	μ_D	47.4	$\mathbf{S_D}$	0.8

(b) Unequal variance t-test

Hypotheses	df	t_0	t_{crit}	P-value	MD	Test result
$\mathbf{H_0 : \mu_0 - \mu_A = 0}$ $\mathbf{H_1 : \mu_0 - \mu_A \neq 0}$	4.9	-0.12	2.59	0.910	-0.3	H_0 cannot be rejected
$\mathbf{H_0 : \mu_0 - \mu_B = 0}$ $\mathbf{H_1 : \mu_0 - \mu_B \neq 0}$	10.4	-0.75	2.22	0.469	-0.8	H_0 cannot be rejected
$\mathbf{H_0 : \mu_1 - \mu_C = 0}$ $\mathbf{H_1 : \mu_1 - \mu_C \neq 0}$	13.9	1.42	2.15	0.177	0.8	H_0 cannot be rejected
$\mathbf{H_0 : \mu_1 - \mu_D = 0}$ $\mathbf{H_1 : \mu_1 - \mu_D \neq 0}$	12.0	-2.71	2.18	0.019	-1.7	H_0 can be rejected

$\alpha = 0.05$; MD: mean difference; df: degrees of freedom.

ANNEX A – HEAT TREATMENT CERTIFICATES

TECNOTÊMPERA
Tecnotêmpera Tratamentos Térmicos Ltda.
Rodovia BR 280 - KM 45 - Corticeira - Guaramirim - SC
89270 000 - Fone 47 3373 3353 - Fax 47 3373 4230
www.tecnotempera.com.br

Página: 1 Hora: 02:17:32 Data: 26-08-13

CERTIFICADO DE TRATAMENTO TÉRMICO

EMPRESA CERTIFICADA ISO 9001/2008

BUREAU VERITAS Certification

Nro. 262367

Cliente: 105 TORNEARIA GUINTHER LTDA

Nota do Cliente 4812 Pedido do Cliente

Material ASI 304L Peça INOXIDAVEL

Quantidade 24,0000 Peso 4,1000

Especificações
Inspeção Inicial

Tratamento: ALIVIO DE TENSOES

Propriedades Solicitadas	Propriedades Obtidas	Nr. Peças Testadas	Observações
Camada (mm):	Camada (mm):	24,0000	
Dureza:	Dureza: 6/8HRC		

Durômetro:
Cód.: 01 DUROMETRO WOLPERT HT 1A
Empresa Certificadora: DUROCONTROL
Nº Certificado Calibração: CAL-0714.1212.01
Data de Calib.: 12-12-12
Próxima Calib.: 12-12-13

Controle:
Controlador: NILTON
Data: 26-08-13 Hora: 02:17

TECNOTÊMPERA
Tecnotêmpera Tratamentos Térmicos Ltda.
Rodovia BR 280 - KM 45 - Corticeira - Guaramirim - SC
89270 000 - Fone 47 3373 3353 - Fax 47 3373 4230
www.tecnotempera.com.br

Página: 1 Hora: 02:25:00 Data: 26-08-13

CERTIFICADO DE TRATAMENTO TÉRMICO

EMPRESA CERTIFICADA ISO 9001/2008

Nro. 262368

BUREAU VERITAS Certification

Cliente: 105 TORNEARIA GUINTHER LTDA

Nota do Cliente 4812 Pedido do Cliente
Material 1020 Peça SAE 1020

Quantidade 21,0000 Peso 3,5500

Especificações
Inspeção Inicial

Tratamento: ALIVIO DE TENSOES

Propriedades Solicitadas	Propriedades Obtidas	Nr. Peças Testadas	Observações
Camada (mm):	Camada (mm):	21,0000	
Dureza:	Dureza: 6/8HRC		

Durômetro:
Cód.: 01 DUROMETRO WOLPERT HT 1A
Empresa Certificadora: DUROCONTROL
Nº Certificado Calibração: CAL-0714.1212.01
Data de Calib.: 12-12-12
Próxima Calib.: 12-12-13

Controle:
Controlador: NILTON
Data: 26-08-13 Hora: 02:24

TECNOTÊMPERA
Tecnotêmpera Tratamentos Térmicos Ltda.
Rodovia BR 280 - KM 45 - Corticeira - Guaramirim - SC
89270.000 - Fone 47 3373 3353 - Fax 47 3373 4230
www.tecnotempera.com.br

Página: 1 Hora: 03:19:40 Data: 23-08-13

CERTIFICADO DE TRATAMENTO TÉRMICO

EMPRESA CERTIFICADA ISO 9001/2008

BUREAU VERITAS Certification

Nro. 262365

Cliente: 105 TORNEARIA GUINTHER LTDA

Nota do Cliente 4812 Pedido do Cliente

Material ALUMINIO Peça ALUMINIO

Quantidade 20,0000 Peso 2,2500

Especificações

Inspeção Inicial

Tratamento: ALIVIO DE TENSÕES

Propriedades Solicitadas	Propriedades Obtidas	Nr. Peças Testadas	Observações
Camada (mm):	Camada (mm):	3,0000	
Dureza:	Dureza: ALIVIO DE TENSÕES		

Durômetro:

Cód.: 01 DUROMETRO WOLPERT HT 1A

Empresa Certificadora: DUROCONTROL

Nº Certificado Calibração: CAL-0714.1212.01

Data de Calib.: 12-12-12

Próxima Calib.: 12-12-13

Controle:

Controlador: JENACIR FREITAS

Data: 23-08-13 Hora: 03:19

ANNEX B – MOTOR SPINDLE SPECIFICATION

3 Specifications and Dimensions

3-1 Specifications

Model	MZ01	
Allowable Rotation Speed	60,000min^{-1}	Effective working range is not less than 5,000min^{-1}. Continuous duty not more than 50,000min^{-1} is recommended.
Spindle Accuracy	Within 1 μm	

Accessories List (Confirm after unsealing)

- Motor spindle main body (MZ01) 1piece
- Chuck nut (MCN1) 1piece
- Wrench (MSP1) 2pieces
- Air hose Φ4x4m (AH4-40) 1piece
- Operation Manual 1piece

Optional

- Motor cord 3m(MKD-30), 4m(MKD-40), 6m(MKD-60), 8m(MKD-80)
- Collets chuck : every 0.5mm from 1.0mmφ to 6.0mmφ (0.2Φ – 1.0Φ can prepare)

※ Motor cord and collets chuck are not included in this device.
Please order upon selecting appropriate sizes for use.

3-2 Dimension of External Appearance

- BT shank

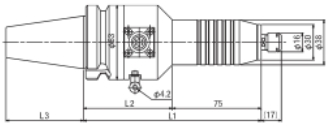

Product Code	Dimension (mm)			Weight (kg)
	L1	L2	L3	
MZ01-BT30	165	90	48	2.1
MZ01-BT40	150	75	65.4	2.2
MZ01-BT50	160	85	101.8	4.8

- SK shank

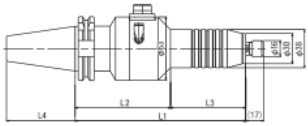

Product Code	Dimension (mm)				Weight (kg)
	L1	L2	L3	L4	
MZ01-SK40	170	95	75	68.4	2.3
MZ01-SK50	160	85	75	101.8	4.9

Source: MINITOR CO. [76]

ANNEX C – SOCKET TECHNICAL DRAWING